Charles University in Prague
Faculty of Mathematics and Physics

DOCTORAL THESIS

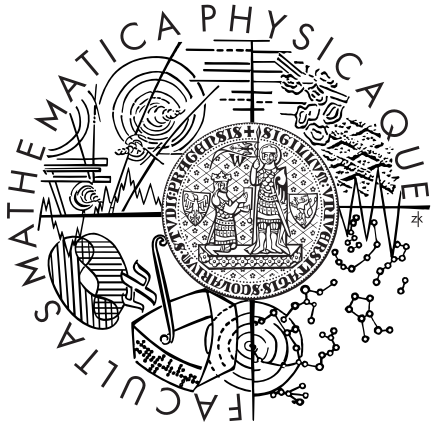

Karel Kouřil

Local structure of hexagonal ferrites studied by NMR

Department of Low Temperature Physics

Supervisor of the doctoral thesis:

prof. RNDr. Helena Štěpánková, CSc.

Study programme:
Physics

Specialisation:
4F3, Condensed Matter Physics and Material Research

Prague 2013

Acknowledgments

I am most grateful to my supervisor prof. RNDr. Helena Štěpánková, CSc. for introducing me to fields of hexagonal ferrites and nuclear magnetic resonance, and for patient and inspiring guidance she provided me with.

Mgr. Vojtěch Chlan, PhD and Ing. Pavel Novák, CSc. taught me about electronic structure calculations and provided me with abundance of help on this matter. The calculations were performed at subcluster Dorje of the computing center Golias at Institute of Physics AS CR and at computing cluster of Department of Low Temperature Physics.

Following people provided their samples: Ing. J. Buršík, CSc. from Institute of Inorganic Chemistry AS CR, prof. P. Görnert, dr. C. Dubs and dr. R. Müller from Innovent e.V. Jena, prof. T. Kimura and Y. Hiraoka from Osaka University and prof. J. Töpfer from University of Applied Sciences Jena.

I would also like to thank prof. Kimura and his team for their hospitality during my stays in Japan and for letting me use their facilities for the magnetoelectric experiments presented in this work.

I declare that I carried out this doctoral thesis independently, and only with the cited sources, literature and other professional sources.

I understand that my work relates to the rights and obligations under the Act No. 121/2000 Coll., the Copyright Act, as amended, in particular the fact that the Charles University in Prague has the right to conclude a license agreement on the use of this work as a school work pursuant to Section 60 paragraph 1 of the Copyright Act.

In . . . . . date . . . . . signature

Název Práce: Studium lokální struktury hexagonálních feritů metodami NMR
Autor: Karel Kouřil
Katedra/Ústav: Katedra fyziky nízkých teplot
Vedoucí doktorské práce: prof. RNDr. Helena Štěpánková, CSc.

Abstrakt: Práce je věnována hexagonálním feritům strukturních typů M, W, X a Y. Tyto materiály byly studovány pomocí NMR, výpočtů elektronové struktury a magnetoelektrických experimentů. Byly získány výsledky týkající se distribuce kationtů, lokalizace železnatých iontů, interpretace NMR spekter studovaných materiálů a důsledků redukce velikosti částic. V tenkých vrstvách strontnatého M feritu a v submikronových částicích barnatého M feritu byla ^{57}Fe NMR spektra ovlivněna efekty snížené velikosti částic. V magnetoelektrických barnatostrontnatých Y hexaferitech s dvojmocnými ionty zinku mělo žíhání pozitivní vliv na jejich magnetoelektrické vlastnosti, zatímco distribuce zinku nebyla výrazně ovlivněna. Ve skandiem substituovaném barnatém M feritu bylo pozorováno rovnoměrné rozložení substituce v krystalu připraveném TSSG technikou. V lantnatostrontnatém M feritu byla zjištěna lokalizace elektronů v podmříži $2a$, dvojná substituce La+Zn, La+Co, a La+Cu vedla k částečné kompenzaci náboje. V strontnatých feritech typu W a X byla pozorována lokalizace železnatých iontů v oktaedrických pozicích v SS blocích.

Klíčová slova: NMR, hexagonální ferity, struktura, multiferoika, defekty

Title: Local structure of hexagonal ferrites studied by NMR
Author: Karel Kouřil
Department/Institute: Department of Low Temperature Physics
Supervisor of the doctoral thesis: prof. RNDr. Helena Štěpánková, CSc.

Abstract: Hexagonal ferrites of M, W, X and Y structure types were studied by means of NMR, electronic structure calculations and magnetoelectric experiments. Presented results deal with cation distribution, localization of ferrous ions, interpretation of NMR spectra of studied materials and effects of size reduction. In oriented layers M type strontium ferrite and submicron particles of M type barium ferrite pronounced effects of reduced size were observed on ^{57}Fe NMR spectra. Performance of magnetoelectric barium-strontium Y type hexaferrites with divalent zinc cations improved upon thermal treatment of samples while distribution of zinc was not significantly altered. In Sc substituted BaM, Sc content was found to be uniform throughout TSSG grown crystal. In LaSrM systems electron localization in $2a$ sublattice was observed, co-substitution with La+Zn, La+Co and La+Cu was found to lead to partial charge compensation. In strontium ferrites of type W and X localization of ferrous ions in octahedral sites in SS block pair was observed.

Keywords: NMR, hexagonal ferrites, structure, multiferroics, defects

Contents

Chapter 1

Introduction

At present hexagonal ferrites are well established magnetic materials with many uses, they can be found in cost-effective hard magnets as well as in components for high-frequency applications. Interest in hexaferrites has been rekindled by discovery of intrinsic magnetoelectrics amongst Y type materials with strong coupling of magnetic and electric order as well as by emergence of various low-dimensional hexaferrite systems (e.g. nanoparticles and thin layers). Of course there is still effort devoted to "classical" hexaferrite systems aimed on improving their performance in applications and unveiling related physics.

This work deals with hexagonal ferrites of different types. We were interested in their microstructure, namely preference sites for substitution atoms, changes of substitution distribution upon thermal treatment, localization of ferrous ions and effects of lowering particle size. To answer these questions we employed nuclear magnetic resonance (NMR), a local technique providing information on close surroundings of probe nuclei, and electronic structure calculations, which have been utilized in order to obtain more insight into the NMR data. In case of Y type hexaferrite samples magnetoelectric experiments have been performed as well.

First there are introductory chapters dealing with studied systems (chapter 2), employed techniques (chapters 3 and 4) and describing the actual approaches applied in the pursuit of information on the studied systems (chapter 5).

These chapters are followed by the ones devoted to actual results, each of these chapters has its own summary.

In chapter 6 we start with study of oriented SrM layers on $SrTiO_3$ substrate and submicron size BaM particles, in these systems we observed effects of particle size on NMR spectra.

Then there is chapter 7 on magnetoelectric Y type hexaferrites where we

aimed on effect of thermal treatment on microstructure and magnetoelectric properties of these materials.

This is followed by chapter 8 containing theoretical considerations useful for analysis of ^{57}Fe NMR spectra of substituted M type hexaferrites.

In chapter 9 we deal with Sc doped BaM spheres, where we investigated spatial homogeneity of Sc content (and content of possible contaminants) throughout parent single crystal out of which the spheres were fabricated.

Next comes chapter 10 dealing with LaSrM hexaferrites and LaSrM co-substituted by Zn, Cu and Co. Here we studied effect of extra charge brought in by trivalent La and its compensation by co-substitution by the divalent small ions. In co-substituted systems we also investigated site preference of small cations.

Finally there is chapter 11 on interpretation of ^{57}Fe spectra of $SrFe_2W$ and $SrFe_2X$ hexaferrites, and localization of ferrous ions in these structures.

Main results presented in the thesis are summarized in chapter 12.

Chapter 2

Hexagonal ferrites

Out of iron oxides, hexagonal ferrites are a broad subset which is of great practical importance as well as scientific interest. These systems are ferimagnets as dominant interaction between magnetic ions is oxygen-mediated antiferomagnetic superexchange. They offer a variety of magnetic structures and properties – these qualities are determined by structure and particular composition. In following we will briefly deal with materials studied in this work. More detailed information may be found elsewhere [1–6].

2.1 Crystal structure

Hexaferrite structure is based on layers of tightly packed large ions, which are either solely oxygen anions or oxygen anions and large cations (Ba^{2+}, Sr^{2+}, Pb^{2+}, La^{3+} ...). Interstitial cavities between large ions are occupied by small cations, most typically Fe^{3+} or Fe^{2+}, other elements can be introduced as well (Zn^{2+}, Co^{2+}, Al^{3+}, Ti^{4+}, ...).

All hexaferrite unit cells may be viewed as composed of of so-called structural blocks – smaller structural motifs repeating within a hexaferrite unit cell. There are three basic structural blocks: S, R and T. The blocks can be stacked along hexagonal axis in many different sequences, thus giving rise to abundance of various hexaferrite types [1–3].

2.1.1 Structural blocks

The three different structural blocks denoted as S, R and T, contain 2, 3 and 4 oxygen layers respectively (along with small cations in the interstitial cavities). In R and T blocks there are also large cations present in the inner layers. Further there are small cation sites on block boundary, which are shared

by two adjacent blocks. The blocks are depicted in figure 2.1.

S block may also be viewed as a slice of cubic spinel structure. It contains two oxygen layers, small cations occupy tetrahedral cavities and two types of octahedral ones (in spinel structure all octahedral sites are equivalent, however we further distinguish sites on block boundary, which are shared by adjacent blocks, from these located inside the block).

R block consists of three large ion layers, the outer ones contain exclusively oxygen anions while in the central one there are large cations. Small cations occupy two types of octahedral cavities and one type of 5-coordinated bipyramidal cavity, which may also be viewed as two face sharing tetrahedral cavities.

T block is the largest with 4 large ion layers, the outer layers again consist solely of oxygen while both inner layers contain oxygen anions as well as large cations. Small cations are in two types of octahedral and one type of tetrahedral cavities.

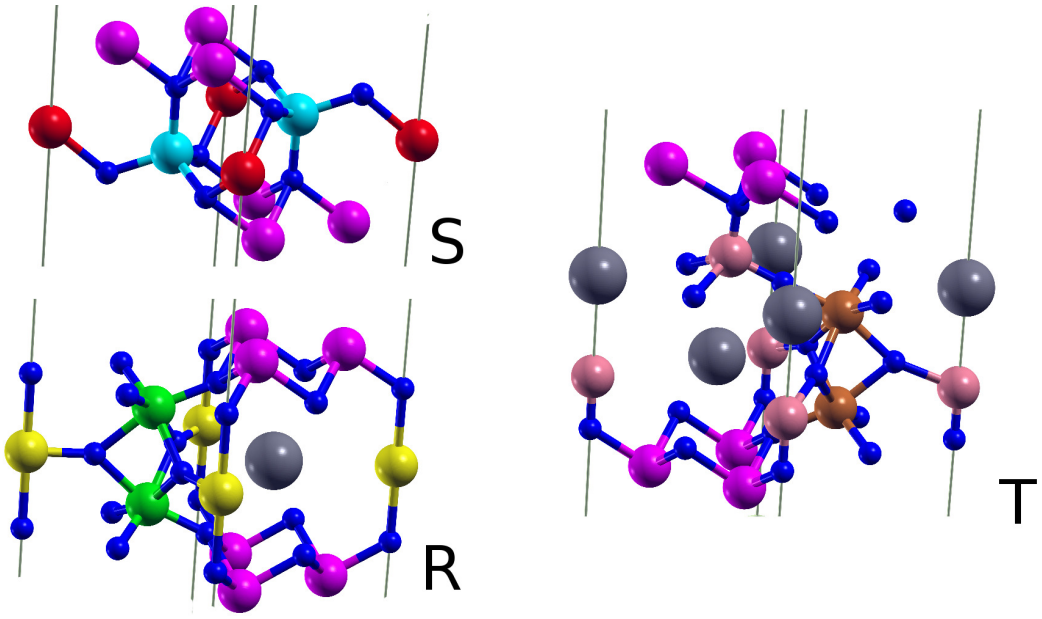

Figure 2.1: Structural blocks of hexagonal ferrites. Small blue balls represent oxygen atoms, large grey balls represent large cations, coloured balls represent small cations. Size of the balls is in no relation to ionic radii. The small ions depicted in magenta color are shared by two adjacent blocks. Created with XCrySDen [7].

2.1.2 M type

The M type hexagonal ferrite consists of regularly altering R and S blocks, the sequence corresponding to one unit cell being RSR*S* where the * denotes rotation of the block by 180° about hexagonal c axis. One unit cell contains two formula units (f.u.) $LFe_{12}O_{19}$. Depending on large cation type (L = Ba, Sr ...) the systems are labeled as BaM, SrM...

Spacegroup of M type structure is $P6_3/mmc$, large cations are in $2d$ sites, small cation occupy five different crystallographic sites: 3 octahedral: $2a$, $4f_{\mathrm{VI}}$, $12k$, one tetrahedral $4f_{\mathrm{IV}}$ and one bipyramidal $2b$. The $4f_{\mathrm{IV}}$ and $4f_{\mathrm{VI}}$ sites are also labeled as $4f_1$ and $4f_2$ respectively.

Lattice constants are $c \approx 23.1$ Å and $a \approx 5.9$ Å, they vary by up to 1% amongst BaM, SrM and PbM systems. Planes of large cations perpendicular to hexagonal axis are mirror planes of the structure. The bipyramidal $2b$ polyhedra can be pictured as composed of two face-sharing oxygen tetrahedra, it has been suggested that the $2b$ iron is actually split by about 0.16 Å into two half-atoms above and bellow the mirror plane [3, 8].

In LaM system cooled below 110 K the lattice symmetry changes from hexagonal to orthorhombic $Cmcm$ [9], comparison of corresponding unit cells is in figure 2.3. The most important consequence of the structural change is, that hexagonal ($P6_3/mmc$) $12k$ sites are split 1:2 into orthorhombic ($Cmcm$) $16h$ and $8f_3$ sites.

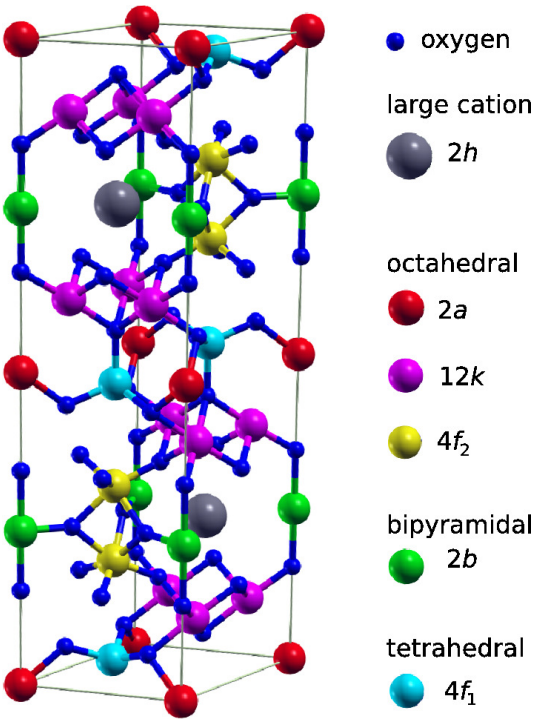

Figure 2.2: Unit cell of M–type hexagonal ferrite. Oxygen anions occupy five nonequivalent sites, which are not distinguished. Size of the balls is in no relation to ionic radii. Created with XCrySDen [7].

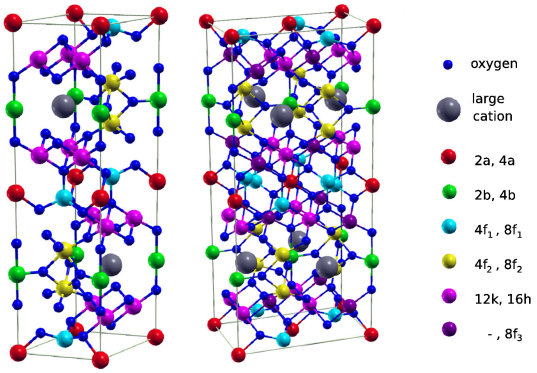

Figure 2.3: Comparison of small cation positions in orthorhombic and hexagonal unit cell of LaM. Hexagonal $12k$ position breaks up into orthorhombic $16h$ and $8f_3$. While hexagonal unit cell contains two formula units, the orthorhombic contains four. Created with XCrySDen [7].

2.1.3 W and X types

The W and X type hexaferrites contain one additional S block per formula unit, which leads to formation of two sites for divalent ions per f.u. (assuming divalent large cations and trivalent small ions). The W or X systems are usually denoted as LM_2W or L_2M_2X where L stands for large ion and M for divalent ion. One formula unit of W ferrite is $LM_2Fe_{16}O_{29}$ and one f.u. of X type is $L_2M_2Fe_{28}O_{46}$, one unit cell of W type hexaferrite contains 2 f.u., unit cell of X type contains 3 f.u. Stacking sequence of W type is $RSSR^*S^*S^*$ and that of X type is $RSRSSR^*S^*R^*S^*S^*$. Spacegroup of W type structure is $P6_3/mmc$, spacegroup of X structure is $R\bar{3}m$.

Crystallographic positions of iron ions in M type, LFe_2W and L_2Fe_2X hexaferrites are listed in table 2.1 together with orientations of magnetic moments of the sites. There are seven inequivalent small cation sites in W type and eleven in X type. Unit cells of W and X type hexaferrites are shown in figure 2.4, that of M type can be found in figure 2.2.

One can see that W type resembles M type with pair of S blocks in place of single S block in M. The X structure than can be viewed as formed by stacking of two types of block sequences: half M cell (RS block pair) and half W cell (RSS block triplet). While in M and W structures the planes of large cations perpendicular to hexagonal axis were mirror planes, in X structure is this symmetry lost and the two octahedral sites inside R blocks are no longer equivalent.

Block	Coordination	Hexaferrite type		
		M	W	X
S	octahedral	$\uparrow 2a$		$\uparrow 3b_{\mathrm{VI}}$
S	tetrahedral	$\downarrow 4f_{\mathrm{IV}}$		$\downarrow 6c_{\mathrm{IV}}$
R	octahedral	$\downarrow 4f_{\mathrm{VI}}$	$\downarrow 4f_{\mathrm{VI}}$	$\downarrow 6c_{\mathrm{VI}}$, $\downarrow 6c^{*}_{\mathrm{VI}}$
R	bipyramidal	$\uparrow 2b$	$\uparrow 2d$	$\uparrow 6c_{\mathrm{V}}$
SS	octahedral		$\uparrow 4f_{\mathrm{VI}}$	$\uparrow 6c_{\mathrm{VI}}$
SS	tetrahedral		$\downarrow 4e$, $\downarrow 4f_{\mathrm{IV}}$	$\downarrow 6c_{\mathrm{IV}}$, $\downarrow 6c^{*}_{\mathrm{IV}}$
R–S	octahedral	$\uparrow 12k$		$\uparrow 18h_{\mathrm{VI}}$
R–SS	octahedral		$\uparrow 12k$	$\uparrow 18h^{*}_{\mathrm{VI}}$
S–S	octahedral		$\uparrow 6g$	$\uparrow 9c_{\mathrm{VI}}$

Table 2.1: Comparison of crystallographic positions occupied by iron in M, W and X hexaferrites and their spin orientations.

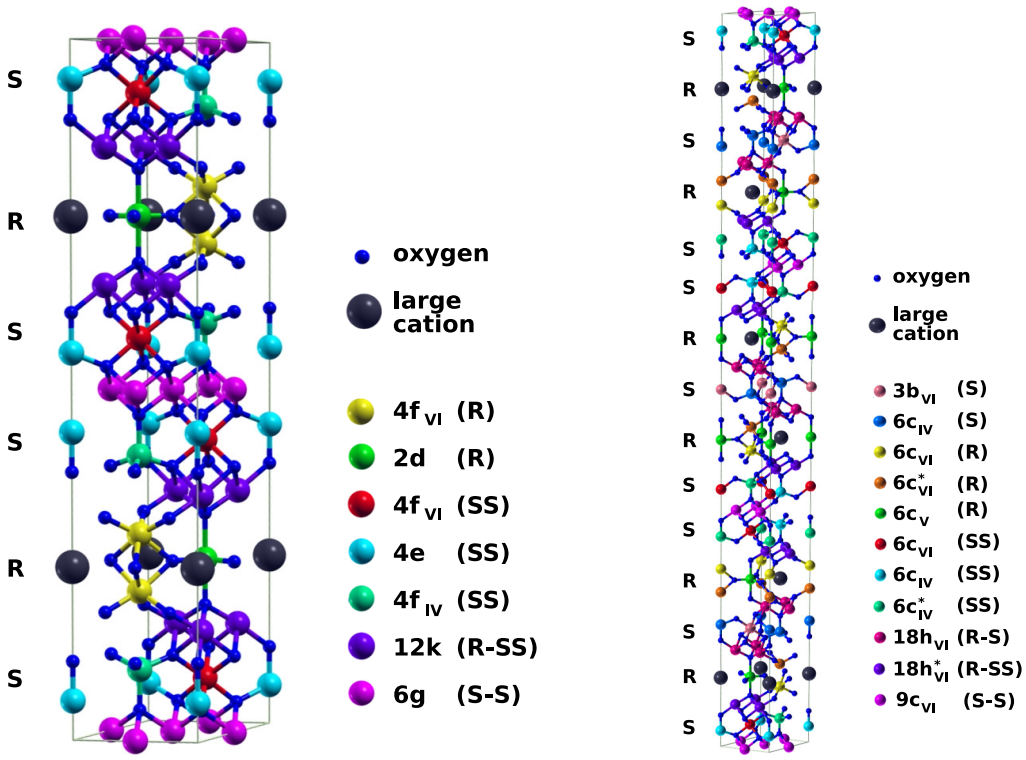

Figure 2.4: Unit cells of W type hexaferrite (left) and of X type hexaferrite (right). Created with XCrySDen [7].

2.1.4 Y type

One unit cell contains three formula units $L_2M_2Fe_{12}O_{22}$ and consists of STS'T'S"T" sequence of blocks, where ' denotes rotation by 120° about hexagonal axis. Spacegroup of Y type structure is $R\bar{3}m$. As in W and X type hexaferrites, in Y type there are two divalent M ions per f.u. as well. There are six inequivalent positions for small ions in the structure – see figure 2.5.

We studied $Ba_{1-x}Sr_xZn_2Y$ systems, in these materials the divalent Zn cations occupy tetrahedral sites, however as there are twice as much tetrahedral sites as there are Zn cations in the structure, hence on top of (Ba–Sr) disorder in occupation of large cation sublattice there is (Fe–Zn) disorder in occupation of tetrahedral sublattices.

Main effect of Ba–Sr substitution is change of $6c^*_{\mathrm{IV}} - \mathrm{O} - 6c_{\mathrm{VI}}$ bond angle as relatively large Ba^{2+} cations are replaced by smaller Sr^{2+} cations. This allows to tune magnetic properties of the system.

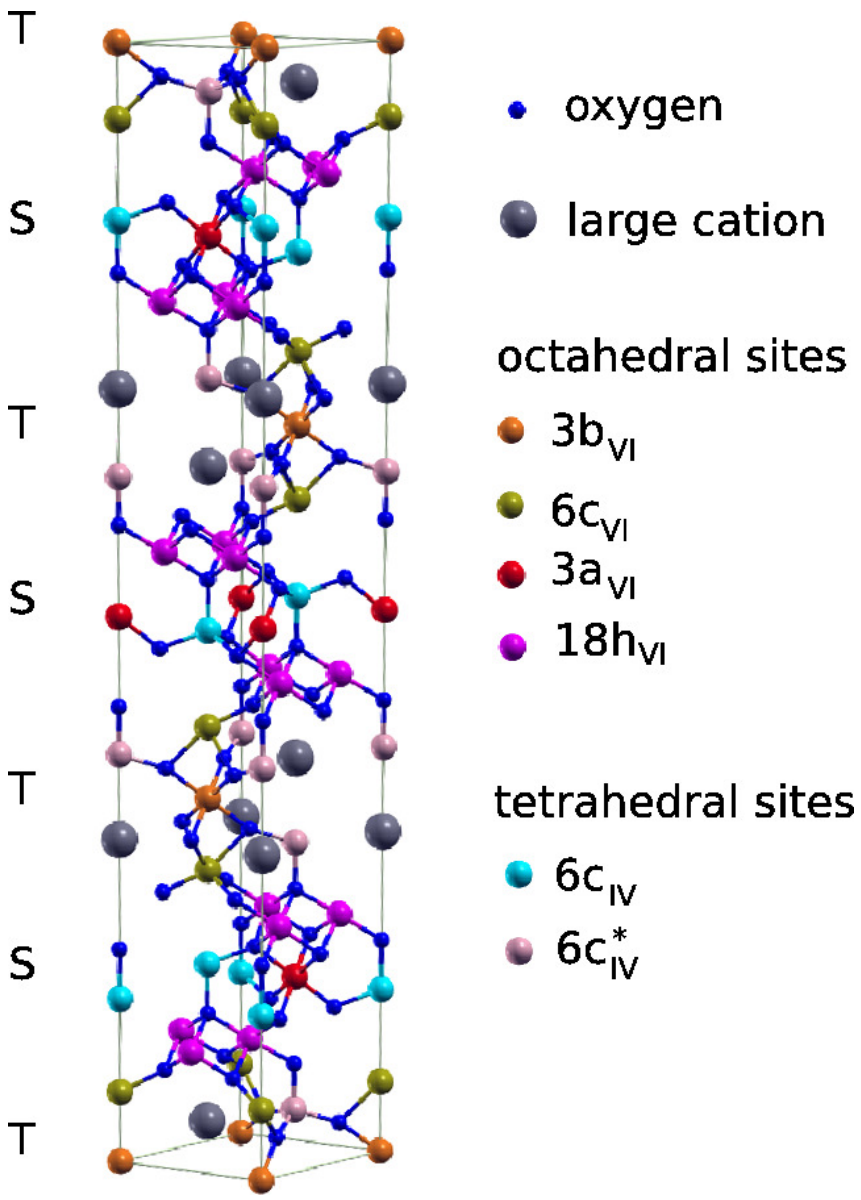

Figure 2.5: Unit cell of Y–type hexagonal ferrite. Created with XCrySDen [7].

2.2 Magnetism

Dominant interaction shaping magnetic structure of the hexaferrites is superexchange mediated by oxygen anions. Raw estimates of exchange interaction strengths can be based on Goodenough–Kanamori rules. Interactions between neighbor ferric ions are antiferromagnetic their magnitude increases as bond angle (ion1 — oxygen — ion2) deviates from 90°.

The antiferromagnetic interactions lead to ferrimagnetic order, which depending on particular system can be collinear or of more complex character. Ordering temperatures are typically well above room temperature.

Magnetocrystalline anisotropy of hexagonal ferrites can be described in term of corresponding energy density [4]:

$$f_K = K_1 \sin^2\theta + K_2 \sin^4\theta + \cdots \tag{2.1}$$

where $K_{1,2}$ are first two anisotropy constants and θ is angle between hexagonal axis and total magnetization. Easy directions of magnetization are such, that minimize the f_K. If $K_1 + K_2 > 0$ one gets uniaxial anisotropy (easy direction of magnetization is parallel with hexagonal axis), if $K_1 + K_2 < 0$ one gets easy-plane type of anisotropy (magnetization lies in plane perpendicular to hexagonal axis). When the anisotropy constants are of similar magnitude and opposite signs one may get easy-cone type of anisotropy (if $0 < -K_1/2K_2 < 1$).

2.2.1 M, W and X types

The M ($LFe_{12}O_{19}$), W ($LM_2Fe_{16}O_{29}$) and X ($L_2M_2Fe_{28}O_{46}$) systems are hard uniaxial collinear ferrimagnets with easy direction of magnetization along hexagonal c–axis. Orientations of magnetic moments were summarized in table 2.1.

Currie temperatures are about 740 K for BaM and SrM systems, 700 K for LaM, 730 K for Fe_2W and 700 K for Zn_2X [1, 2]. Exchange interactions in M type hexaferrite were estimated from results of electronic structure calculations [10] as well as from experimental temperature dependences of sublattice magnetizations [11] and four strong antiferromagnetic exchanges were identified: $a - f_{\mathrm{IV}}$, $b - f_{\mathrm{VI}}$, $k - f_{\mathrm{IV}}$ and $k - f_{\mathrm{VI}}$.

2.2.2 Y type

$BaZn_2Y$ has collinear magnetic order and its magnetocrystalline anisotropy is of easy plane type with preferred orientation of magnetization in hexagonal plane. Currie temperatures of Zn_2Y ferrites are about 400 K [2]. Upon substitution of Ba by Sr noncollinear order appears [12, 13], magnetization remains confined to hexagonal plane.

The magnetic order can be conveniently seen in terms of alternating stacking of large ($\mathcal{L}$) and small ($\mathcal{S}$) magnetic blocks along hexagonal axis. Small magnetic block contains inner part of structural T block ($3a_{\mathrm{VI}}$ and $6c^*_{\mathrm{IV}}$ sites), large magnetic block contains spinel block and outer parts of its neighbor T blocks ($6c_{\mathrm{VI}}$, $18h_{\mathrm{VI}}$, $6c_{\mathrm{IV}}$ and $3a_{\mathrm{VI}}$ sites). Within blocks there is collinear ferrimagnetic order, exchange between blocks is tuned by replacing Ba ions with Sr [14, 15].

In external magnetic field $Ba_{0.5}Sr_{1.5}Zn_2Y$ develops rich magnetic phase diagram [14]. At 4.2 K and in fields about $0.3 - 2.2$ T there is cycloidal component in the magnetic order. The spin cycloid breaks inversion symmetry of the system and gives rise to electrical polarization via spin-current mechanism [5, 16–19] which can be seen as inverse effect of Dzyaloshinskii–Moria interaction [20, 21]. Vector of resulting electrical polarization is perpendicular to magnetization and lies in hexagonal plane as well. This improper electric order is dependent on underlying magnetic order and thus can be easily controlled by external magnetic field [14].

Chapter 3

Nuclear magnetic resonance

Phenomenon of nuclear magnetic resonance (NMR) allows one to study hyperfine structure of nuclear levels which arises from lifting $2I + 1$ nuclear groundstate degeneracy (I being spin of the nucleus) by electromagnetic interactions. NMR utilizes radiofrequency (rf) magnetic field $\boldsymbol{B}_1$ to bring nuclear spin system out of equilibrium and observes response in form of time dependent nuclear magnetization. After processing the recorded response a NMR spectrum is obtained. The spectrum contains information on the underlying interactions responsible for the hyperfine structure, the interactions in turn are determined by the studied system.

NMR is local, i.e. contribution of any individual nucleus is to large extent determined by its close surroundings (within few Å). This makes it very suitable for study of various types of defects or disorders within system in question.

In this chapter we will briefly deal with principles of pulsed NMR with emphasis on its applications is magnetically ordered materials, more detailed information on the technique can be found in textbooks [22–26].

3.1 Hyperfine interactions

Hyperfine interactions may be defined as such interactions of nucleus with its surroundings, that lift the $2I + 1$ groundstate degeneracy.

In general these interactions are of electromagnetic nature. The first nonzero terms of magnetic and electric multipole expansions, which allow for coupling of external fields to nuclear spin, are magnetic dipolar and electric quadrupolar interaction. Since higher order terms are negligible, hyperfine spin hamiltonian consists of two contributions:

$$H_{\mathrm{hf}} = H_{\mathrm{m}} + H_{\mathrm{Q}} \tag{3.1}$$

Only terms explicitly dependent on nuclear spins are considered in the hamiltonian, this huge simplification stems from the spin hamiltonian approach which assumes, that effect of nuclear spins on electronic wavefunction is very weak. The action of nuclei on electrons is considered only in description of electron-mediated internuclear interactions and of enhancement effect in magnetics, apart from this, it may be neglected if ones object of interest are the nuclei. The electrons are considered to be an environment which acts strongly upon the nuclear spins while being only weakly disturbed by them.

In following we will go even further and neglect the internuclear interactions. In strongly correlated systems with non-compensated electron spins, which are subject of this work, any direct (dipole–dipole) internuclear interactions are negligible compared to electron–nuclear or electron mediated internuclear interactions, because nuclear magnetic moments are at least two orders of magnitude smaller than the electronic ones. If the electron mediated internuclear interactions are negligible as well (e.g. due to low natural abundance of $I > 0$ nuclei) one view the nuclei as passive local probes delivering information on the electronic system.

3.1.1 Magnetic dipolar interaction

Nuclear magnetic moment is given by $\boldsymbol{\mu} = \gamma \boldsymbol{I}$, where γ is gyromagnetic ratio, a constant characteristic for given isotope and state. Magnetic part of the hyperfine hamiltonian then is:

$$H_{\mathrm{m}} = -\gamma \boldsymbol{B} \cdot \boldsymbol{I} \tag{3.2}$$

where $\boldsymbol{B}$ is local magnetic field on nuclear site.

3.1.2 Electric quadrupolar interaction

Hamiltonian of nuclear quadrupolar interaction is:

$$H_{\mathrm{Q}} = \frac{eQ}{\hbar 2I(2I-1)} \boldsymbol{I} \cdot \nabla \boldsymbol{E} \cdot \boldsymbol{I} \tag{3.3}$$

where Q is magnitude of nuclear quadrupole moment, e elementary charge, $\hbar$ reduced Planck constant and $\nabla \boldsymbol{E}$ is electric field gradient tensor: $(\nabla \boldsymbol{E})_{ij} = \partial^2 \phi / \partial x_i \partial x_j$, ϕ being electrostatic potential. Only nuclei with $I > 1/2$ are subject to quadrupolar interaction.

$\nabla \boldsymbol{E}$ is usually substituted by $\boldsymbol{V} = \nabla \boldsymbol{E} - \frac{1}{3}\boldsymbol{1}\mathrm{Tr}(\nabla \boldsymbol{E})$ since only this component of $\nabla \boldsymbol{E}$ can induce changes of hyperfine structure other than uniform shift of all nuclear levels. $\boldsymbol{V}$ is traceless by definition, hence in its eigensystem only

two numbers are needed for its full description, those usually are V_{zz} – eigenvalue of largest absolute value and $\eta = (V_{xx} - V_{yy})/V_{zz}$ – asymmetry of the $\boldsymbol{V}$. V_{xx} and V_{yy} are the remaining two eigenvalues of $\boldsymbol{V}$ and $|V_{xx}| \leq |V_{yy}| \leq |V_{zz}|$ by convention, hence $0 \leq \eta \leq 1$. Apart from V_{zz} and η one needs to know orientation of $\boldsymbol{V}$'s eigenvectors in order to be able to write down the hyperfine hamiltonian.

3.2 NMR patterns

Resonating nuclei are usually found in various environments (e.g. inequivalent crystallographic positions). Since we neglected the internuclear interactions, we can consider the resulting spectrum simply to be sum of subspectra corresponding to individual sets of electromagnetic fields and isotopes. It is most useful for interpretation of experimental spectra to know what patterns are to be expected as subspectra for known isotope and fields.

The simplest and in this work prevailing case is spin 1/2 nucleus in magnetic field. In such case the expected resonance consists of single line at frequency $\omega = \gamma B_0$ and experimental spectrum can be viewed as proportional to distribution of B_0 magnitudes in the positions of resonating nuclei.

Second case occurring in the following text is the most complicated one – both magnetic and quadrupolar interaction are present and neither is largely dominant to justify treatment of the second one as a perturbation. There are $2I+1$ levels to be expected yielding $I(2I+1)$ resonance lines of varying relative intensity. Positions of lines $\omega_{i,j}$ are given by energy difference of corresponding levels (i and j):

$$\hbar\omega_{ij} = |E_i - E_j| \tag{3.4}$$

Relative intensities can be estimated using matrix element of S_x operator (z axis parallel to static magnetic field) between the eigenfunctions involved:

$$I_{ij} \sim |\langle i|S_x|j\rangle|^2 \tag{3.5}$$

In general it is not always possible to determine hyperfine fields from observed NMR pattern, however one still can compare experiment to results obtained from a model.

3.3 NMR experiment

In order to obtain NMR spectrum, the studied system needs to be excited from thermal equilibrium state by rf pulses, its response recorded and properly processed. Basis of the procedure can be understood in terms nuclear

magnetization $\boldsymbol{M}^{\mathrm{n}}$ being arbitrarily rotated by properly set rf pulses, evolving under action of static magnetic field and returning to thermal equilibrium due to relaxations.

3.3.1 Nuclear magnetization

Typical NMR setup is ensemble of nuclei at temperature T placed in static magnetic field $\boldsymbol{B}_0$ and acted upon by pulses of harmonic rf magnetic field $\boldsymbol{B}_1$ perpendicular to and much weaker than $\boldsymbol{B}_0$. Nuclear magnetic moment is approximately two orders of magnitude smaller than electron one, hence in most practical cases $kT >> \hbar\gamma B_0$ and nuclei in static magnetic field constitute a textbook example of paramagnetism in high temperature limit. Equilibrium nuclear magnetization $\boldsymbol{M}_0^{\mathrm{n}}$ is then given by Curie law:

$$\boldsymbol{M}_0^{\mathrm{n}} = \frac{N\gamma^2\hbar^2 I(I+1)\boldsymbol{B}_0}{3kT} \tag{3.6}$$

where T is temperature, k Boltzmann constant and N number of nuclei in unit volume.

3.3.2 Bloch equations

When the magnetization is deviated out of its equilibrium direction and then left to evolve, it starts to precess around $\boldsymbol{B}_0$ at Larmor frequency:

$$\omega_{\mathrm{L}} = \gamma B_0$$

Due to fluctuating component of hyperfine interactions, relaxation processes occur: rotating transversal component $\boldsymbol{M}_{\perp}^{\mathrm{n}}$ diminishes, while longitudinal component $\boldsymbol{M}_{\parallel}^{\mathrm{n}}$ returns to $\boldsymbol{M}_0^{\mathrm{n}}$. This behavior (precession and relaxation) is described by phenomenological Bloch equations:

$$\frac{\mathrm{d}}{\mathrm{d}t}\boldsymbol{M}_{\parallel}^{\mathrm{n}} = \gamma(\boldsymbol{M}^{\mathrm{n}} \times \boldsymbol{B})_{\parallel} - (\boldsymbol{M}_{\parallel}^{\mathrm{n}} - \boldsymbol{M}_0^{\mathrm{n}})/T_1 \tag{3.7}$$

$$\frac{\mathrm{d}}{\mathrm{d}t}\boldsymbol{M}_{\perp}^{\mathrm{n}} = \gamma(\boldsymbol{M}^{\mathrm{n}} \times \boldsymbol{B})_{\perp} - \boldsymbol{M}_{\perp}^{\mathrm{n}}/T_2 \tag{3.8}$$

In general, relaxation times T_1 and T_2 differ, the only constraint is $T_2 \leq 2T_1$ (apart from statistical fluctuation, the relaxation processes should not generate transient nuclear magnetization larger than is its equilibrium value). Relaxation times can range from days to less than microseconds depending on studied system and temperature. Extreme relaxation times (i.e. hours and more or 10 μs and less) severely limit set of feasible NMR experiments.

Longitudinal relaxation time T_1 corresponds to nuclear spin system returning to thermal equilibrium, the underlying processes involve energy being transferred between the nuclear system and its surroundings ("lattice").

The transversal relaxation time T_2 corresponds, apart from return to thermal equilibrium, to loss of coherence of individual precessions. In most cases, there is a (inhomogeneous) dispersion of resonance frequencies, which results in faster decay of $M_\perp^n$ than this relaxation would have induced, corresponding apparent relaxation time is usually denoted T_2^*. Fast decay of the transversal component due to the resonance frequency dispersion can be reversed by spin echo technique (see below) as this is not true relaxation process but mere reflection of static distribution of resonance frequencies.

Bloch equations provide a comprehensive framework to understanding effect of rf pulse action. If linearly polarized field $2\boldsymbol{B}_1$ perpendicular to $\boldsymbol{B}_0$ oscillating with frequency ω is present, it is convenient to work in rotating reference frame (axis of rotation is along B_0, sense of rotation is the same as it would have been for Larmor precession). The linearly polarized oscillating field can be decomposed into two rotating fields (rotation axis parallel with $\boldsymbol{B}_0$), each with amplitude B_1 and with opposite senses of rotation. In rotating reference frame one of the components is static, while the other rotates at frequency 2ω and effectively averages to zero. Magnetic field in the rotating frame then becomes e.g. $\boldsymbol{B}_{\mathrm{rot}} = (B_1, 0, B_0 - \omega/\gamma)$ (orientation of component perpendicular to rotation axis is given by phase of $2\boldsymbol{B}_1$ oscillations). If resonance condition $\omega = \omega_L$ is met, the resulting field is perpendicular to $\boldsymbol{B}_0$ and magnetization, which was initially parallel with $\boldsymbol{B}_0$, can precess around it. By choosing appropriate intensity and duration of B_1 pulse, one can manipulate nuclear magnetization at will. Under action of pulse of intensity B_1 and duration $\tau \ll T_1, T_2$, magnetization is rotated by $\varphi = \gamma B_1 \tau$, typical values of φ used are $\pi/2$ and π.

Case of $I > 1/2$ nuclei subject to both magnetic and quadrupole interaction is generally due to fact that several different transitions can be excited at the same time. If one can assume selective excitation of only one transition of given nucleus, the situation becomes formally equivalent to that of $I = 1/2$ nucleus in magnetic field. The corresponding effective magnetic field and gyromagnetic ratio are given by the nuclear species and the local fields it interacts with [23].

3.3.3 Spin echo

In spontaneously magnetized systems, distributions of resonance frequencies are rather broad. This results in very short T_2^* thus often prohibiting detection of precession excited by single pulse (free induction decay, FID), because weak NMR signal is obscured by pulse ringdown. This complication is remedied

by spin echo pulse sequence consisting of two pulses. First pulse generates transversal magnetization, signal of which rapidly decays, then after τ_{echo} second pulse is applied which refocuses the individual precessions so that in time $2\tau_{\text{echo}}$ precessing transversal component of nuclear magnetization reappears. Typically (when inhomogeneous broadening is dominant cause of line broadening) the first pulse is set to act as $\pi/2$ and the second as π, but this is not essential for echo to appear. Since τ_{echo} can be set at any value (as long as T_2 relaxation allows) one can avoid ringdown after rf pulses and observe the NMR signal. If T_2 is not too short, this procedure (refocusing by π pulse) can be repeated many times. The corresponding pulse sequence, named CPMG (after Carr, Purcell, Meiboom and Gill who invented it) allows observation of multiple spin echoes in one scan thus significantly improving signal-to-noise ratio (S/N) and reducing required experimental time.

3.3.4 Signal aquisition and processing

Signal observed within single pulse sequence is usually noisy, so the sequence is repeated many times, while signals of individual scans are coherently summed in order to average out the noise. The repetition time is dictated by T_1 relaxation – nuclear system should be in thermal equilibrium when the pulse sequence starts, hence one has to wait several T_1-s between consecutive scans.

Spin echoes are observed as oscillating voltage induced in a pick-up coil (in most setups the same coil is used for generation of rf pulses and detection), this signal is then amplified and digitized for computer processing. Echoes observed in given pulse sequence are summed up and than Fourier transformed (FT), thus revealing finer details of resonance frequencies distribution.

Broad NMR spectra cannot be observed by excitation at a single frequency, thus in order to obtain full spectrum one has to sweep the excitation frequency and construct the spectrum either as an envelope of spectra observed at individual frequencies (in case of rather narrow line profiles with finer details) or simply as a plot of FT amplitudes observed at individual excitation frequencies.

In either case, resulting intensity of NMR signal in a given sample is proportional to number of resonating nuclei, provided that spectrum is not too broad. In case of broad spectra more careful approach to experiment is needed and appropriate frequency corrections of spectral intensities have to be applied.

3.3.5 Frequency corrections of spectral intensities

Reasons for need to apply the frequency corrections are of two types: they are either fundamental physics arguments, or they are based on actual imperfections of the experimental setup.

First fundamental argument is the Faraday law of induction – the voltage induced in the rf coil is proportional not only to magnitude of oscillating magnetic flux but to frequency of the oscillations as well. Resulting signal intensity is then proportional to $\omega n(\omega)$ where $n(\omega)$ is number of nuclei resonating on frequency ω. Second is,that higher frequency means proportionally increased separation of corresponding energy levels, and, due to Boltzman factor, larger difference of their populations in thermal equilibrium. Again, this effect adds ω proportionality to the signal intensity. The two effects combined than lead to signal being proportional to $\omega^2 n(\omega)$, rather than just to $n(\omega)$. This argument is valid to any NMR experiment, however is special cases, there may be further phenomena adding more terms to frequency dependent prefactor in signal intensity. Example of such phenomenon may be the enhancement effect in magnetically ordered materials.

Typical experimental problem altering signal intensity is the impedance mismatch. If the rf circuit in the NMR probe or any component along the signal line is not matched to spectrometer impedance (typically 50Ω), standing waves emerge in the rf lines resulting in oscillatory modulation of the spectrum. Due to such artefacts experiments on higher frequencies are increasingly difficult. Good impedance matching is the most straightforward way to remedy this problem, which from our experience seems to be sufficient for low frequencies (bellow 100MHz).

3.4 Fields on nuclear sites

To lift groundstate degeneracy of nuclei and to perform a NMR experiment one needs static (on timescale of the experiment) magnetic field or (if the nuclei have spin greater than 1/2) electric field gradient, or both. The fluctuating components of the fields will in general be responsible for relaxation phenomena. In following we will deal with the static fields. Subsection on magnetic fields is written with emphasis on magnetically ordered materials, albeit we tried to stay as general as possible, some effects important in diamagnetic materials but comparatively weak in magnetics are not discussed in much detail or not at all.

3.4.1 Electric field gradient

The electric field gradient (EFG) comes from uneven charge distribution in close vicinity of the nucleus and can be viewed as intrinsic property of material the nucleus is embedded in – practically accessible external electric field gradients (e.g. generated by a set of electrodes surrounding the sample) are

typically too small to yield observable changes of nuclear levels.

The EFG tensor symmetry is given by point group of site occupied by resonant nucleus – if symmetry is high enough the EFG cannot be asymmetric (it must have $\eta = 0$), e.g. in case of three or more fold rotational axis, or the tensor must be zero, e.g. if there are three perpendicular mirror planes.

3.4.2 Magnetic field

Nuclear magnetic moment interacts with electrons in the sample and with external magnetic field, the interaction can be written in terms of local magnetic field, operator of which is:

$$\boldsymbol{B}_{\mathrm{loc}} = -\frac{\mu_0 \mu_{\mathrm{B}}}{2\pi} \sum_{i=1}^{N} \left[\frac{8\pi}{3} \boldsymbol{s}_i \delta(\boldsymbol{r}) - \frac{\boldsymbol{s}_i}{r_i^3} + 3\frac{\boldsymbol{r}_i(\boldsymbol{r}_i \cdot \boldsymbol{s}_i)}{r_i^5} + \frac{\boldsymbol{l}_i}{r_i^3} \right] + \boldsymbol{B}_{\mathrm{ext}} \tag{3.9}$$

where $\boldsymbol{s}$ is operator of electron spin, $\boldsymbol{r}$ electron position (nucleus is at $\boldsymbol{r} = 0$), $r = |\boldsymbol{r}|$, $\boldsymbol{l}$ is operator of electron angular momentum ($\boldsymbol{l} = \boldsymbol{r} \times \boldsymbol{p}$, $\boldsymbol{p}$ is operator of electron momentum), μ_0 permeability of vacuum, μ_{B} Bohr magneton, N number of electrons in considered system and $\boldsymbol{B}_{\mathrm{ext}}$ is external magnetic field. The first term is contact interaction arising when electronic and nuclear wavefunctions overlap, the second and third correspond to dipole field of electron magnetic moments and the last term to field generated by motion of electrons.

Magnetic field on nuclear site is sum of effective field generated by electrons in studied sample and external field. Unlike electric field gradient, magnetic fields on nuclear sites are not determined solely by close surroundings of the nuclei, but more distant parts of sample as well as external sources may generate important contributions. It is beneficial to break up the local magnetic field into intrinsic and extrinsic component, the former being characteristic for studied material and the latter for experimental setup (sample shape, NMR magnet ...). Practically it means limiting sum in equation 3.9 to contributions coming from regions in different distances from nucleus. Intrinsic fields can be found experimentally as local fields on nuclei in magnetic domains of well demagnetized sample.

Following Lorentz approach to calculation of local fields in solids we can define the intrinsic magnetic field as that coming from within Lorentz spere (including the Lorentz sphere surface) and the extrinsic as that from outside the sphere. The intrinsic field may be further decomposed into hyperfine and lattice component, the hyperfine coming from interaction of nucleus with "close" electrons (the corresponding limit in sum 3.9 is rather arbitrary, and dependent on particular system, 2 Å may be considered a typical value) and

the lattice component being (in case of localized magnetism) sum of fields generated by magnetic ions (point dipoles) contained within the Lorentz sphere. Typical contributions to extrinsic component are external magnetic field and demagnetizing field of the sample. The above can be summarized in formula:

$$\boldsymbol{B}_{\mathrm{loc}} = \underbrace{\boldsymbol{B}_{\mathrm{hf}} + \boldsymbol{B}_{\mathrm{latt}} + \boldsymbol{B}_{\mathrm{Lorentz}}}_{\text{intrinsic}} + \underbrace{\boldsymbol{B}_{\mathrm{dem}} + \boldsymbol{B}_{\mathrm{ext}}}_{\text{extrinsic}} \tag{3.10}$$

Here $\boldsymbol{B}_{\mathrm{hf}}$ is hyperfine field, $\boldsymbol{B}_{\mathrm{latt}}$ is sum of dipolar fields of magnetic ions in Lorentz sphere, $\boldsymbol{B}_{\mathrm{Lorentz}}$ is contribution of Lorentz sphere surface, $\boldsymbol{B}_{\mathrm{dem}}$ is demagnetization field and $\boldsymbol{B}_{\mathrm{ext}}$ is external field.

The hyperfine field $\boldsymbol{B}_{\mathrm{hf}}$ is determined mainly by parent ion of studied nucleus (on-site hyperfine field $\boldsymbol{B}_{\mathrm{hf}}^{\mathrm{on-site}}$) and to smaller extent also by its neighbors (transfered hyperfine field $\boldsymbol{B}_{\mathrm{hf}}^{\mathrm{trans}}$):

$$\boldsymbol{B}_{\mathrm{hf}} = \boldsymbol{B}_{\mathrm{hf}}^{\mathrm{on-site}} + \boldsymbol{B}_{\mathrm{hf}}^{\mathrm{trans}} \tag{3.11}$$

In $3d$ elements there is proportionality of hyperfine field to magnetic moment of ion with ratio roughly -10 T per μ_{B}.

Demagnetization field is in homogeneously magnetized sample determined solely by its shape (it is homogeneous in ellipsoidal sample and inhomogeneous otherwise), in case inhomogeneous magnetization integration over sample volume exterior to the Lorentz sphere is needed.

Extrinsic magnetic field ($\boldsymbol{B}_{\mathrm{dem}} + \boldsymbol{B}_{\mathrm{ext}}$) adds to intrinsic field thus changing magnitude of local field and shifting the resonance frequency. Additionally the extrinsic field can also modify the intrinsic field by rotating electron magnetization or changing magnetic structure of material. In case of magnetization rotation the effect can be described in terms of local field tensor:

$$\boldsymbol{B}_{\mathrm{in}}(\boldsymbol{n}) = (B_{\mathrm{iso}}\boldsymbol{E} + \boldsymbol{A}) \cdot \boldsymbol{n} \tag{3.12}$$

where $\boldsymbol{n}$ is unit vector parallel with magnetic moment of the ion, $\boldsymbol{B}_{\mathrm{in}}$ intrinsic part of local magnetic field, B_{iso} magnitude of isotropic part of local field tensor, $\boldsymbol{E}$ identity tensor, $\boldsymbol{A}$ anisotropic part of local field tensor (traceless).

In case of ferric ions the isotropic contribution is usually dominant part of local field on nuclei. It comes from contact interaction of s–electrons polarized by d–electrons, the corresponding field is antiparallel with magnetic moment of the particular ion. The anisotropic part is due to dipole field of other magnetic ions as well as anisotropic contributions to hyperfine field. The anisotropic contributions to hyperfine field stem from orbital and dipole fields generated by close electrons, these contributions are small compared to contact field as the d–shell of free ferric ion is half-filled ($3d^5$) with practically no orbital momentum and nearly spherical symmetry.

Symmetry of $\boldsymbol{A}$ tensor is the same as point symmetry of corresponding site. Crystallographic equivalence of sites does not imply magnetic equivalence – due to several possible orientations of $\boldsymbol{A}$ tensors of (crystallographically) equivalent sites one obtains several values of $\boldsymbol{B}_{\mathrm{in}}$ for general orientation of magnetization. Number of magnetically inequivalent sites is reduced when magnetization is oriented in particular high-symmetry directions. For ideal ferrimagnetic crystal one should get as many distinct values of $\boldsymbol{B}_{\mathrm{in}}$ as there are magnetically inequivalent sites occupied by studied ions. In case of none or negligible quadrupole interaction this means, that there is one-to-one correspondence of observed resonance lines and magnetically inequivalent sites (however the lines still may overlap).

3.5 NMR in magnetically ordered materials

NMR in magnetics has at least two features with no counterpart in more common solid-state NMR in diamagnetic materials. Namely large static intrinsic field, which allows for resonance to be observed in zero external field, and effect of enhancement, which amplifies applied rf field as well as nuclear signal. Next, due to distribution of intrinsic fields the spectra can be (relative to resonance frequency) very broad. The local field anisotropy is somewhat analogous to chemical shift anisotropy observed in diamagnetic materials [24–26], but its effect is typically much stronger. The technique does not require single phase samples – non-magnetic second phases are not seen in zero field experiments and even if magnetic second phases are present, there is good chance of separating their signals on basis of different resonance frequency or excitation conditions. Finally, due to large values of magnetization the magnetic samples can produce substantial demagnetizing fields (e.g. in single-domain particles) which can be observed as shifts or (in case of distribution of the fields) broadenings of NMR lines.

3.5.1 Enhancement factor

The electron magnetization can significantly amplify rf pulses applied on sample as well as nuclear response to the pulses [22, 27, 28]. The mechanism is following: applied rf field $\boldsymbol{B}_1$ induces weak oscillations of electron magnetization vector as it tries to be parallel with $\boldsymbol{B}_{\mathrm{A}}^{\mathrm{eff}} + \boldsymbol{B}_1$, where $\boldsymbol{B}_{\mathrm{A}}^{\mathrm{eff}}$ is effective anisotropy field. The oscillating magnetization leads to oscillations of local magnetic field on nuclear sites by approximately the same angle. The oscillating component of local field is η-times larger than the original rf field, which

induced it, the enhancement factor η can be estimated as:

$$\eta = \frac{B_{\mathrm{in}}}{B_{\mathrm{A}}^{\mathrm{eff}}} \sin\alpha \tag{3.13}$$

where B_{in} and $B_{\mathrm{A}}^{\mathrm{eff}}$ are magnitudes of intrinsic magnetic field on nuclear site and of effective anisotropy field, α is angle between direction of rf field and $\boldsymbol{B}_{\mathrm{A}}^{\mathrm{eff}}$. The $\boldsymbol{B}_{\mathrm{A}}^{\mathrm{eff}}$ is given by sum of all interactions keeping magnetization in its direction and expressed as effective field – it includes magnetocrystalline anisotropy, demagnetizing field (shape anisotropy) and external field. In demagnetized sample in zero external field the $\boldsymbol{B}_{\mathrm{A}}^{\mathrm{eff}}$ is given only by magnetocrystalline anisotropy.

Obviously, the effect of enhancement is strongest, when rf field is perpendicular to magnetization – typically (in demagnetized collinear uniaxial magnet) perpendicular to easy axis of sample material. There may be further orientation dependence of η due to $\boldsymbol{B}_{\mathrm{A}}^{\mathrm{eff}}$ – magnitude of this effective field can vary depending on direction into which one tries to rotate magnetization from its equilibrium position (e.g. in case of easy-plane type of magnetocrystalline anisotropy).

As $\boldsymbol{B}_{\mathrm{A}}^{\mathrm{eff}}$ arises from combined effects of magnetocrystalline anisotropy, shape anisotropy and external field, strong external fields can become dominant part of $\boldsymbol{B}_{\mathrm{A}}^{\mathrm{eff}}$, hence significantly reducing η compared to its zero-field value.

The effect of enhancement is also present in case of nuclear response – one can define effective field acting from nuclear spins on electronic magnetic moments and proceed in similar manner as in case of rf field. The resulting enhancement factor can be again estimated by formula 3.13, only α is now angle between magnetization and axis of pick-up coil.

So far we only discussed enhancement of signal from magnetic domains. In case of domain walls the enhancement is present as well, however since oscillations of magnetic moments in domain walls are of different nature (they are induced by domain wall motion) the values of η in walls differ from that in domains and further they are dependent on position of nucleus within the wall, on details of wall magnetic structure, its mobility etc. The enhancement in domain walls may be much stronger than in domains, thus allowing for separation of the signals by excitation conditions.

3.5.2 Local field anisotropy

Anisotropic term in equation 3.12 is responsible for dependence of NMR spectra on orientation of magnetization. Its effect can be seen in zero-field experiments as well as in experiments conducted in external magnetic fields. In

zero field experiments it can be responsible for line splitting (two or more resonance lines correspond to one crystallographic position e.g. ^{57}Fe NMR a lines in YIG [29]) or broadening (e.g. domain wall spectra – within the wall many orientations of magnetization are realized [30]). External magnetic field can apart from adding to local fields also change orientation of magnetization and thus alter the anisotropic contribution to local fields.

For single crystal in external field, one can expect observed resonance lines to shift and split as magnetization orientation changes. Components of $\boldsymbol{A}$ tensor can be extracted from angular dependences of spectra. In case of powder or polycrystalline sample in external magnetic field various orientations of crystals are present which leads to line shifting and broadening (in comparison to zero-field domain spectra).

3.5.3 Defects

If ideal structure of material is perturbed by a defect, intrinsic fields (both magnetic and electric) on nuclei in its vicinity are altered in specific manner. One can view effect of a defect in terms of additional component of intrinsic field effectively generated by the defect on close nuclei $\Delta\boldsymbol{B}_{\mathrm{in}}$. Resonance frequencies of the nuclei are changed accordingly and corresponding so-called satellite lines appear in spectrum. In case of low concentration of defects this leads to formation of satellite line pattern in NMR spectrum which is characteristic for particular type of defect. Intensity of satellite lines is determined by concentration of the defect (for low concentrations there is linear relation between concentration and satellite intensity).

In general, magnitude of $\Delta\boldsymbol{B}_{\mathrm{in}}$ drops fast with distance between the defect and resonating nucleus. In case of point defects constituted by cationic substitution one can typically observe satellite lines corresponding to defect being nearest (cationic) neighbor (nn) or next nearest neighbor (nnn) of resonant nucleus, further defects usually cannot change the local fields sufficiently to induce well separated resonance line and manifest themselves as broadening of main resonance line (corresponding to unperturbed ideal structure).

In higher concentrations the defects lead to broad NMR profiles, which may be viewed as a sum of many different satellite lines, each corresponding to particular configuration of defects in vicinity of resonant nucleus.

Chapter 4

Electronic structure calculations

While NMR technique can provide data containing detailed information on studied sample, especially in case of complicated systems (like hexaferrites) it is not straightforward to interpret its results and extract relevant information. We used calculations of electronic structure as a tool complementary to NMR as these can furnish theoretical estimates of hyperfine parameters thus allowing for direct comparison with experiment. Apart from the hyperfine parameters the calculations do of course supply abundance of further physically relevant output amongst which valences and magnetic moments of individual ions were of interest for us.

In following we will briefly deal with density functional based method of calculations, more detailed description can be found in literature [31–34].

4.1 Density functional

When looking for ground-state solution of manybody quantum mechanical problem such as that of electrons and nuclei in solids, one usually utilises Born–Oppenheimer approximation (i.e. considers nuclei as fixed reducing them to a source of external potential for electrons). Within its framework then one can look either for the ground-state wavefunction of the N electrons $\Psi(\boldsymbol{r}_1, \boldsymbol{r}_2, \ldots, \boldsymbol{r}_N)$ or for corresponding electron density $\rho(\boldsymbol{r})$. The former approach is used in Hartree–Fock (HF) family of methods, while the latter in the density functional theory (DFT). In calculations concerning condensed matter systems the DFT is usually the method of choice, as it is better suited for larger systems.

The DFT expresses ground-state energy as functional of electron density:

$$E[\rho] = T_0[\rho] + V_{\mathrm{N-N}} + V_{\mathrm{N-e}}[\rho] + V_{\mathrm{e-e}}[\rho] + V_{\mathrm{xc}}[\rho] \tag{4.1}$$

$T_0[\rho]$ is kinetic energy of non-interacting electrons, $V_{\mathrm{N-N}}$ potential energy of electrostatic repulsion of nuclei, $V_{\mathrm{N-e}}[\rho]$ contribution from electron–nuclear interaction, $V_{\mathrm{e-e}}[\rho]$ mean field electron–electron interaction (Hartree term) and finally the $V_{\mathrm{xc}}[\rho]$ is exchange–correlation contribution which is defined as difference between exact $E[\rho]$ and that computed using only first four terms of 4.1. In contrast to previous terms its exact form is not known.

As it follows from theorems of Kohn and Hohenberg [35], the true ground-state density minimizes functional 4.1, furthermore once the density is found, all relevant information can be extracted from it (i.e. appropriate density functional can be written for any observable).

The problematic exchange-correlation term $V_{\mathrm{xc}}[\rho]$ has to be estimated, however, once a workable approximation is found, it can be used for large variety of systems. One approximation to $V_{\mathrm{xc}}[\rho]$ is based on comparison with homogeneous electron gas, for which "exact" numerical solution is available from quantum Monte Carlo calculations hence one can get the $V_{\mathrm{xc}}(\rho)$ from definition (in homogeneous electron gas the V_{xc} is mere function of its density). Neglecting non-locality of true $V_{\mathrm{xc}}[\rho]$ one can arrive at Local Density Approximation (LDA) or Local Spin Density approximation (LSDA) in spin-polarized calculation. LDA or LSDA estimate contribution (to exchange-correlation energy) from each infinitesimal volume of studied system as contribution of the same volume of homogeneous electron gas with the same overall density. Going one step further and taking into account also changes of electron density yields Generalized Gradient Approximation (GGA) which gives slightly better results than LDA, however it is no more uniquely defined – there is a family of GGA approximations.

4.2 Kohn–Sham scheme

Kohn and Sham [36] used approach, in which, instead of trying to find ground-state density directly, they interpreted the functional 4.1 as describing non-interacting electrons which are subject to external potentials. They arrived at Schrödinger equation for non-interacting electrons:

$$\left(-\frac{\hbar^2}{2m_{\mathrm{e}}}\nabla^2 + \frac{e^2}{4\pi\varepsilon_0}\int\frac{\rho(\boldsymbol{r}')}{|\boldsymbol{r}-\boldsymbol{r}'|}\mathrm{d}\boldsymbol{r}' + V_{\mathrm{xc}} + V_{\mathrm{ext}}\right)\phi_i = \epsilon_i\phi_i \tag{4.2}$$

In this equation exchange-correlation are described by potential V_{xc} which is defined as functional derivative of exchange-correlation functional:

$$V_{\mathrm{xc}} = \frac{\delta V_{\mathrm{xc}}[\rho]}{\delta\rho} \tag{4.3}$$

Other terms in hamiltonian in equation 4.2 are same as usual: the first corresponds to kinetic energy (m_e is electron mass), the second is Hartree part of electron-electron interaction (e is electron charge, ε_0 permittivity of vacuum) and V_ext is external potential (generated by nuclei), ϕ_i are wavefunctions and ϵ_i corresponding energies.

The wavefunctions ϕ_i do not correspond to true one-electron wavefunctions in the system (in contrast to HF methods), however (as Kohn an Sham have proven) they do yield correct electron density:

$$\rho(\boldsymbol{r}) = \sum_{i=0}^{N} |\phi_i(\boldsymbol{r})|^2 \tag{4.4}$$

where the sum runs over N (number of electrons in the system) lowest energy wavefunctions.

The problem of finding ground-state density is solved iteratively: First, a starting density is generated (typically as a sum electron densities confined inside individual atomic spheres). Second, potentials in equation 4.2 are determined from the density. Third, new density is constructed from solutions of 4.2, mixed with the previous density (or densities) and again used to generate potentials. This process runs until self-consistency is reached, i.e. the newly found density is the same as the one used to generate the potentials in 4.2.

4.3 Basis

In order to solve equation 4.2 effectively one needs to approximate the wavefunctions ϕ_i as linear combinations of finite number of basis functions. This transforms the differential equation into problem of diagonalizing the hamiltonian matrix (expressed in the chosen basis). One needs basis, which is as small as possible (in order to minimize computation time) and universal (i.e. well suited for large variety of systems) at the same time.

In solid state computations, muffin-tin approach is often used – studied crystal is broken up into two parts: non-overlapping atomic spheres S_α (α labels inequivalent atoms) and interstitial region I in between.

To describe so-called core states, in which the wavefunction is completely confined within atomic sphere, atomic-like functions (single particle solutions of Schrödinger equation for particular element) are used. Basis functions for valence electrons which take part in chemical bonding are then constructed as plane waves in the interstitial and as atomic-like functions in the spheres, the atomic and interstitial parts are matched so that resulting function is continuous at sphere boundary. The resulting basis set is called Augmented

Plane Waves (APW):

$$\phi_{\boldsymbol{K}}^{\boldsymbol{k}}(\boldsymbol{r}) = \begin{cases} \frac{1}{V} e^{i(\boldsymbol{K}+\boldsymbol{k})\cdot\boldsymbol{r}} & \boldsymbol{r} \in I \\ \sum_{l,m} A_{l,m}^{\alpha,\boldsymbol{k}+\boldsymbol{K}} u_l^\alpha(r', E) Y_m^l(\boldsymbol{r}'_0) & \boldsymbol{r} \in S_\alpha \end{cases} \tag{4.5}$$

$\boldsymbol{K} + \boldsymbol{k}$ is wavevector of the plane wave ($\boldsymbol{k}$ is the part confined within the first Brillouin zone, $\boldsymbol{K}$ is reciprocal lattice vector), V is unit cell volume, $A_{l,m}^{\alpha,\boldsymbol{k}+\boldsymbol{K}}$ are coefficients that ensure matching of plane wave part and atomic part of wavefunction on atomic sphere boundary, $u_\alpha^l(r', E)$ is radial part of solution of Schrödinger equation of atom α for energy E, the r' is distance from the centre of the particular atomic sphere, $Y_l^m(\boldsymbol{r}'_0)$ are spherical harmonics as a function of direction with respect to centre of atomic sphere ($\boldsymbol{r}'_0 = \boldsymbol{r}'/|\boldsymbol{r}'|$).

Reasonable measure of APW basis size is product of smallest atomic sphere radius $R_{\min}$ and largest wavevector $K_{\max}$, the larger the $R_{\min}K_{\max}$ the better results can be expected (as the basis is larger). This measure can be used also for the other bases discussed below although the optimal values of $R_{\min}K_{\max}$ for given system depend on particular basis.

Main drawback of APW basis is its dependence on energy E at which the atomic wavefunctions are constructed. This energy has to be matched to band energies $\epsilon_{\boldsymbol{k}}^n$ for the basis to perform well, however the energies $\epsilon_{\boldsymbol{k}}^n$ need to be determined from equation 4.2 during the iterative process hence the basis changes during the calculation thus slowing it down significantly.

To remedy the energy dependence of APW basis, Taylor expansion of $u_l^\alpha(r', E)$ to first order in energy can be used – energy dependence of the basis functions is linearized and one only needs to estimate energy at which the expansion is performed. The corresponding basis set is called Linearized Augmented Plane Waves (LAPW). The LAPW requires more basis functions (higher $R_{\min}K_{\max}$) than APW, however energies in definition of its functions are now fixed and only need to be set somewhere in corresponding band, hence they can be estimated in the beginning and kept constant during the calculation.

Estimating the energies for LAPW functions is not always straightforward due to so-called semi-core states. These states are still quite localized inside the atomic sphere but are not too far in energy from the valence states. Setting the energy to neither that of the valence band nor of the semi-core state (nor in between the two) yields good results. To improve description of the semi-core states and remove ambiguity in energy estimates, so-called local orbitals (LO) are added, yielding LAPW+LO basis. The LO is set to be non-zero only inside particular atomic sphere.

Another possibility is to use APW basis with fixed energies (thus again removing its energy dependence) and add another type of local orbitals (lo)

to treat semi-core states (APW+lo basis). It is advantageous to combine LAPW with APW+lo especially when one needs to work with valence d and f states – these are more effectively described using APW+lo while the rest can be treated by LAPW.

4.4 Strongly correlated systems

LSDA by itself cannot well describe strongly correlated systems; in order to improve its performance, approaches like self-interaction correction (SIC) [37] and various versions of LDA+U [38–40], or more recently hybrid functionals [41–43] and combination of DFT with dynamic mean field theory (DMFT) [44–46] were introduced in literature.

One of methods used for transitional metal oxides is self-interaction corrected GGA combined with Hubbard model (GGA+U(SIC)) [39]. The model uses effective $U_{\text{eff}} = U - J$ where U and J are on-site repulsion and exchange [47, 48]. Typical values for U_{eff} in d elements are 1–10 eV.

Since in principle GGA+U(SIC) is a mean field approximation it is inevitably quite crude, furthermore magnitude of correlation effects is set "externally" by U. In the end one cannot expect it to describe the correlation in much detail, but rather to mimic its effects and give results qualitatively more resembling experimentally observed features of strongly correlated systems while on finer level its predictions can still be misleading. In spite of its drawbacks GGA+U(SIC) can provide correct insulating states where LSDA fails to do so (and where SIC gives too small gaps) and significantly improve theoretical description of materials with strongly correlated electrons.

Chapter 5

Procedures adopted in applied techniques

In this chapter we present practical notes on techniques actually used in experiments and related calculations.

5.1 NMR

The NMR spectra have been measured using modified CPMG pulse sequence where all excited echoes are recorded (see figure 5.1). Fast T_1 relaxations were measured using modified inversion recovery pulse sequence – instead of FID it used spin echo for signal detection (see figure 5.2).

Because of substantial width of spectra, they were recorded in frequency-sweep regime. We studied resonances of ^{57}Fe ,^{59}Co , ^{63}Cu , ^{65}Cu , ^{67}Zn , ^{139}La and ^{139}La (see table 5.1). Gyromagnetic ratios of this nuclei are rather low, which combined with low natural abundances of ^{67}Zn and ^{57}Fe (none of studied samples were enriched) meant that high detection sensitivity needed to be achieved in order to observe their resonances.

Vast majority of NMR experiments has been performed at temperature of 4.2K.

Isotope	Abundance (%)	Spin	$\gamma/2\pi$ (MHz/T)	Q (10^{-31}m^2)
^{57}Fe	2.2	1/2	1.382	– –
^{59}Co	100.0	7/2	10.08	420
^{63}Cu	69.2	3/2	11.32	−220
^{65}Cu	30.8	3/2	12.10	−204
^{67}Zn	4.1	5/2	2.669	150
^{139}La	99.9	7/2	6.061	200

Table 5.1: NMR–relevant properties of selected isotopes.

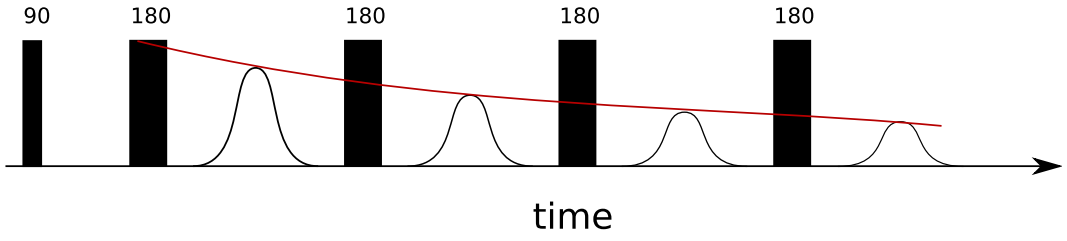

Figure 5.1: CPMG pulse sequence. The first 90° pulse brings the nuclear magnetization into transversal plane, each of following 180° pulses then refocuses it thus forming a spin echo. Amplitude of signal gradually decreases due to transversal relaxation.

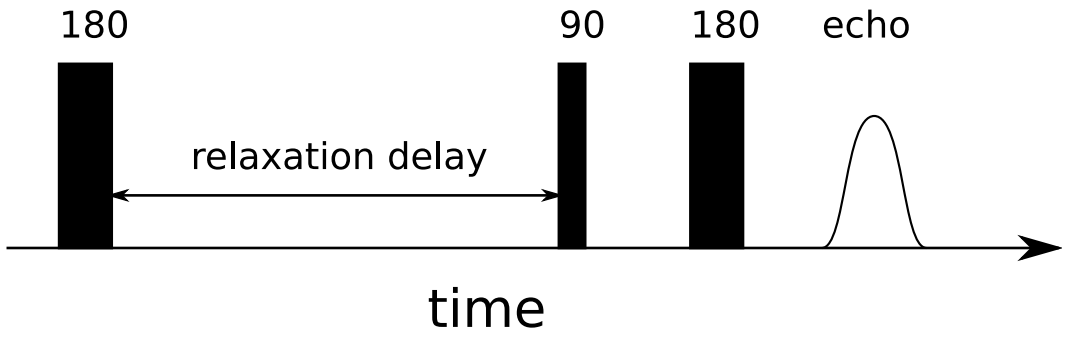

Figure 5.2: Modified inversion recovery pulse sequence. First pulse inverts the nuclear magnetization which then during the relaxation delay returns to its equilibrium value until it is "observed" by standard spin echo pulse sequence. The whole sequence recurs with sufficiently long repetition time, which allows the nuclear system to reach equilibrium.

5.1.1 Equipment

The NMR experiments have been performed using two commercial Bruker Avance NMR consoles, which have been adapted to experiments on magnetically ordered materials. NMR spectrometer consist of two basic sections – one responsible for generation of high power rf pulses used for excitation of nuclei, and the second, which detects the weak nuclear response and digitizes it for further processing (typically coherent summation and fast fourier transform). The most important of the mentioned adaptations were use of high power broadband rf. amplifiers in the excitation section (300W to 1kW, frequency range $6 - 900$MHz) and of fast analog-to-digital converter in the detection section.

NMR probehead is a dedicated insert which fits into a Dewar vessel or cryostat and provides electrical as well as mechanical connection between its room temperature end and cold end (where the sample is placed), further the probehead serves as Faraday cage for reducing parasitic signals from various outside rf sources. The probeheads used in the experiments were custom-made, designed with emphasis on low temperature operation. The main two types of probeheads used in NMR experiments were broadband and tuned ones.

In broadband probehead, sample is placed in coil of damped rf circuit (typical physical realization was coil connected on one end to rf line, coil was wrapped in grounded copper sheet which acted as capacitance). Such probehead allows experiments in broad frequency range to be run without physical presence of experimentalist thus using experimental time more effectively, however, due to its usually large mismatch its sensitivity is low, frequency dependent and it cannot produce strong rf pulses.

Problems of broadband probehead can be avoided by using tuned probehead, which has higher sensitivity and allows stronger rf pulses to be applied on sample. On the other hand, in frequency-swept experiments this probehead needs to be tuned manually at each frequency step.

Tuned probehead utilises parallel resonant RLC circuit with tunable capacitor. Sample is again placed in the coil of the circuit. The available frequency range is determined by coil inductance and extremal capacitances of the capacitor – while varying the inductance “shifts” the available frequency range, the capacitor determines ratio of maximal and minimal accessible frequency which is typically about one octave (depending on capacitor and magnitude of parasitic capacitances).

The resonant circuit is either inductively or galvanicaly coupled to rf line. In case of galvanic coupling, rf line is connected directly to sample coil, typically to one of first few turns from its ground terminal. Inductive coupling is realised via separate few turn coil, wound next to or on top of “resonant” coil. The

coupling coil is connected between the rf line and ground. The coupling has to be set in such way, that it ensures impedance matching of the RLC circuit to rf line. In practice this means changing position of rf line connection for galvanic coupling and number of matching coil turns (as well as overall circuit geometry) in case of inductive coupling. The matching has to be tested with sample inside the coil and at same temperature as the NMR experiment is to be performed.

Good matching is vital when one needs accurate intensities of NMR signal (mismatch leads to frequency dependent modulation of resulting signal intensity) and when samples with weak signals are studied (e.g. thin layers). In most experiments we used tuned probeheads, either galvanicaly or inductively matched.

In the resonant circuit a resistor parallel with coil may be used, if needed, to lower quality factor of resulting circuit – too high quality factor of the circuit means experimental complications, namely narrow resonance curve that apart from being too frequency-selective makes the experiment sensitive to minute instabilities of tuning capacitance which, to our experience, are inevitable.

Especially in low frequency experiments (below 25MHz) with inductively coupled probeheads extra care had to be taken in order to minimize influence of parasitic capacitances between resonant coil and matching coil, as these reduce width of accessible frequency range. To do this, we typically placed coupling coil (which is nearly on ground potential) near ground terminal of resonant coil. If multilayer rf coil was used, then terminal from the outer layer was the grounded one – this reduces voltage between rf and coupling coil (which was wound on top of the rf coil) again minimizing influence of the parasitic capacitance.

Typical capacitances of tunable capacitors were in range of units to tens of pF. Resistors used to damp the resonant circuit were at the order of several kΩ. The coils depended on desired frequency range, but for ^{57}Fe frequencies ($50-80$ MHz) the typical coils for powder samples (placed in cylindrical teflon containers with 4 mm diameter and 2 cm long) were made of $0.2-1$ mm copper wire and had between 10-20 turns. Coils for single crystals or thin layers were designed with emphasis on good filing of coil volume with sample material – coil dimensions were dictated by the studied sample and desired inductance was set by number of coil turns.

Example of such little more elaborate NMR coil is shown in figure 5.3. This particular coil was used for experiments on single-crystal 330 μm hexaferrite spheres hence its dimensions needed to be appropriately small. The coil was made of thin (diameter 0.06 mm) copper wire tightly wound on thin glass capillary in two layers, totaling about 50 turns. Further there was another 8 turn

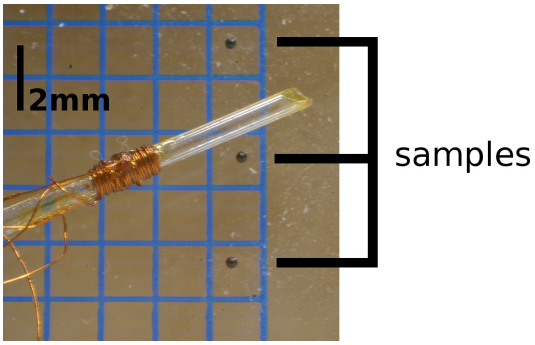

Figure 5.3: Samples of 330 μm hexaferrite spheres and NMR coil used in experiments on these samples. Two of the four leads to the coil connect to resonant coil, the other two to coupling coil. Samples were fixed inside the coil by dried resin. Sample orientation inside coil was set by permanent magnet placed outside the coil while resin dried.

coil wound on top of the resonant coil, which acted as an inductive coupling of probehead rf circuit to the spectrometer. The sample was manipulated into the coil by a permanent magnet and glued in place by diluted resign. Field of the permanent magnet was approximately perpendicular to the coil axis, this guaranteed nearly optimal orientation of sample easy axis for detection of signal from magnetic domains.

Experiments in external magnetic field were performed using either superconducting magnet insert in He Dewar vessel (thus sample temperature was fixed at 4.2 K) capable of fields up to 2.5 T or resistive electromagnet capable of approximately 0.7 T combined with He continuous flow cryostat. Due to space constraints only broadband probeheads were used in experiments with the superconducting magnet.

Most experiments have been done at 4.2 K – NMR probehead with sample was partially submerged in liquid helium stored in transport Dewar vessel. The only exception are experiments performed in the resistive magnet where the cryostat was used.

5.1.2 Experiment optimization

In order to obtain reliable data several parameters of pulse sequence need to be found. First are the excitation conditions – lengths and amplitudes of applied rf pulses. Those were checked prior to all spectra measurements on several frequencies and optimized for signal from magnetic domains. If they were frequency dependent, spectra were measured several times with varying

amplitude of the pulses.

Maximum pulse amplitude was dictated by rf amplifiers together with probehead (if pulses are too strong electrical breakdowns appear in resonant circuit, hence pulses must be weak enough to avoid this). Typical pulse voltages (at rf amplifier output) were in range from units of volts to about 200V (this corresponds to setting rf attenuation to $0 - 40$ dB) and pulse durations were in range from of units of μs to 20μs for $\pi/2$ pulse. Usually the pulses were set as short as possible in order to achieve excitation of broadest possible frequency interval (with $\pi/2$ pulse duration 1.5 μs one can homogeneously excite about 50 kHz interval centered at pulse frequency).

Next one needs at least rough estimate of relaxation times, T_1 in order to set sufficiently long repetition time so the system is in each scan excited from well-defined thermal equilibrium state and T_2 to set appropriate number of echoes in CPMG pulse sequence. The repetition times ranged from 10 ms to few minutes (the latter was case of non-substituted SrM powder). Usually we observed as many echoes as possible, in case of long T_2 the number of echoes was limited by maximum size of data that the analog-to-digital converter was able to process – this in practice meant that at maximum several hundred (or units of thousand) of echoes were recorded.

The last parameter which was always optimized was separation of pulses in the CPMG sequence – this was set to be long enough for the echo to fit between consecutive pulses but not excessively long, which would unnecessarily reduce signal-to-noise ratio (S/N). In samples with broad resonance lines was the echo width proportional to pulse duration, in such a case pulse separation (between consecutive π pulses in CPMG) was at the order of tens of μs. If narrow lines were present, the pulse separation needed to be increased to about 150 μs.

Number of scans was set within limits obtained during experiment optimization (most importantly the repetition time) in order to obtain high enough S/N. This meant using between 8 and several tens of thousand scans depending on absolute signal intensity and available experimental time.

If deemed necessary, more specific information on above discussed parameters used in NMR experiments is given separately in particular chapters.

5.1.3 Data processing

The raw time-domain data have been processed in dedicated software, which allowed summation of selected echoes from CPMG sequence, their Fourier transform and construction of resulting spectra. These were obtained either as envelope of partial spectra obtained at individual frequencies or simply as plot of amplitudes of the partial spectra at individual excitation frequencies.

The excitation frequency amplitude of Fourier transform was also used for evaluation of other experiments (relaxations, pulse intensity optimization).

5.2 Magnetoelectric experiments

There were two types of ME experiment: measurements of sample permittivity as a function of external magnetic field and measurements of sample electrical polarization as a function of external magnetic field. Both experiments were performed at several temperatures between 4.2K and 300K, both shared the same probehead, magnet and cryostat hence one could change experiment simply by switching probehead connections at room temperature without heating or moving the sample – this allowed to observe both properties (sample capacitance C and electric polarization P) under quite similar conditions.

5.2.1 Sample preparation

The studied samples were Y–type hexaferrites which have magnetic easy-plane perpendicular to hexagonal c–axis. The electrical polarisation arising from the magnetic order is perpendicular to magnetization and the c–axis, both vectors lie in hexagonal plane of the sample.

In order to observe ME effects sample has to be prepared as a thin (tenths of mm) plate with two parallel faces, while the c–axis is parallel with the sample plane. To observe ME effects one has to apply magnetic field in both hexagonal plane (perpendicular to c–axis) and sample plane – sample magnetization then aligns with the field, the resulting electrical polarization is perpendicular to sample plane and may be detected by electrodes deposited on the sample faces. The described configuration is depicted in figure 5.4.

The samples usually developed a reflective face which corresponds to hexagonal plane, which was confirmed by X-ray diffraction. We used the reflective faces to determine c–axis orientation in ME experiments.

Samples were cut by diamond disc, then polished on gradually finer sandpaper into shape of planparallel plates. After polishing golden electrodes were deposited on opposite faces of the samples using a thermal evaporator. The samples were fixed on holder and masked by Al foil in order to leave only one face exposed to the vapor, it was necessary to avoid any gold deposition on sample edges since this would short-circuit the electrodes. Gold electrode was deposited on the exposed sample area, then the procedure was repeated for the second face.

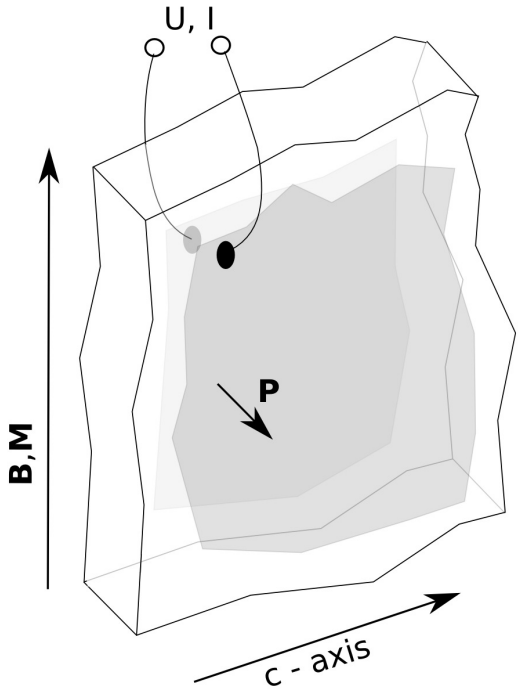

Figure 5.4: Sample orientation in ME experiments. External magnetic field, electrical polarization and sample c–axis are perpendicular to each other. Electrodes are evaporated on opposite faces of sample. ME effects are observed as changes of sample permitivity or depolarizing currents.

5.2.2 Experimental setup

Both sample electrodes were connected to probehead low-temperature terminals via thin golden wire. The wire was attached to a electrode by silver paste and welded to probehead terminal. Each terminal was connected to two coaxial cables which led to room-temperature connectors of the probehead – from the terminals on the experiments were performed as four-point measurements. Samples were fixed on the probehead by a grease which hardened on cooling.

The probehead was inserted in helium-flow cryostat inside superconducting magnet capable of producing filed up to 8 T. The cryostat allowed to set sample temperature in range $4.2 - 300$ K.

The sample with electrodes formed a small capacitor, one could either observe field dependence of its capacitance as a function of magnetic field and temperature, or instead one could observe electrical currents associated with (dis)charging the capacitor.

5.2.3 Capacitance

Sample capacitance was measured by Agilent E4980A precision LCR meter at four different frequencies: 1 kHz, 10 kHz, 100 kHz and 1 MHz.

5.2.4 Polarization

Depolarizing currents were observed by Keithly 6517A electrometer. Prior to measurement sample was polarized by following procedure: At zero magnetic field a voltage (typically 100V) was applied on sample. With voltage on magnetic field was increased to value corresponding to ME phase. This ensured formation of single ferroelectric domain in the sample.

Once the sample has been polarized, voltage was dropped to zero and changes of electrical polarization induced by field sweeping were observed as depolarizing currents. If no depolarizing currents could have been observed due to too high sample conductivity, polarizing voltage was kept on and the currents were measured. With too conductive samples observation of depolarizing currents was no longer possible – they become too small compared to background current generated by polarizing voltage.

5.3 Electronic structure calculations

The calculations were done in WIEN2k program package using GGA approximation to exchange-correlation potential of Perdew, Burke and Ernzerhof [49]

together with effective Hubbard on-site repulsion – the GGA+U(SIC) [39] approach.

5.3.1 Applied procedures

First a structure file for studied system was generated based on experimental structure data. This file contains information on spacegroup, lattice constants, internal structure parameters atomic species occupying the individual crystallographic sites and radii of muffin-tin spheres (S_α) on individual sites. The radii were kept the same for all atoms of particular element, when two calculations were to be compared atomic sphere radii for particular element were kept exactly the same in both of them.

Starting calculations were performed with rather low values of parameters that govern accuracy (and computation time): number of k–points in first Brillouinzone (determines density of k–points mesh), product $R_{\min}K_{\max}$ (controls number of plane waves in basis) and $G_{\max}$ (maximum length of k–vector in Fourier expansion of potentials). This yielded good starting point for further finer calculations in which values of the parameters were gradually increased until the results no longer displayed significant changes upon further increase (typically this meant over 200 k–points, $R_{\min}K_{\max} \geq 6$ and $G_{\max} > 15\mathrm{Ry}^{\frac{1}{2}}$).

Optimizations of internal structure parameters (i.e. minimization of total energy with respect to internal structure parameters) were performed for "intermediate" values of the above mentioned parameters in order to minimize atomic forces in final calculations.

The effective Hubbard U was utilized on $3d$ elements and set to about 1 eV per $3d$–electron. In some cases it was found practical to start the calculation with low U and gradually increase it, if full value of U was set from the beginning, convergence was not always reached.

When spin–orbit interaction was needed, it was included after the above described process (i.e. structure optimization and refinement of results by calculations with increased basis size) as it significantly increases difficulty of calculation (symmetry is reduced, calculation is always complex and generally larger basis is needed).

Most parameters extracted from calculations were taken directly from the WIEN2k output file (e.g. EFG tensor, magnetic moments of ions, total energy of system), valences were calculated using Atoms in Molecules (AIM) program incorporated in the WIEN2k package.

The AIM program is based on theory of Bader [50], it inspects the electron density surrounding selected nucleus for critical surface on which there is zero flux of gradient of electron density: $\nabla\rho(\boldsymbol{r})\cdot\boldsymbol{n}(\boldsymbol{r}) = 0$, where $\boldsymbol{n}(\boldsymbol{r})$ is unit vector normal to the surface. Electron density within volume enveloped in the surface

is then integrated and corresponding valence (difference between number of electrons obtained from the integration and atomic number of the nucleus) is ascribed to the atom. The calculated valences are in absolute values somewhat smaller than the nominal ones. For easier comparison, results of AIM can be rescaled – multiplied by number obtained from condition that average oxygen valence after rescaling is -2, this yields valences of ferric ions close to $+3$.

We also used AIM to calculate magnetic moments of ions – these are obtained as difference of spin-up and spin-down charge contained inside atomic volume. In contrast to magnetic moments listed in WIEN2k output, which are calculated from charge inside atomic sphere, these results are not too sensitive to values of atomic sphere radii. Finally AIM can also provide volumes of individual atoms.

5.3.2 Hyperfine field on ferric cations

Magnetic fields on nuclei of $3d$ elements calculated within LDA+U or GGA+U methods can easily be several tens of percent off as a result of too crude description of exchange and correlation effects. Upon more detailed inspection it can be found, that while anisotropic part of intrinsic fields is predicted quite correctly (and can be used for interpretation of experimental data [51]), the isotropic term is responsible for the error. The reason lies in contact contribution of s electrons, which dominates the isotropic term and which is incorrectly accounted for within the +U methods.

Novák and Chlan introduced empirical correction [52] which bypasses the flawed calculation of contact fields and enables to predict total intrinsic fields on ^{57}Fe in ferric cations with error at the order of one Tesla. They took calculated spin magnetic moments of $3d$ and $4s$ electrons and expressed the contact contribution as:

$$B_c = a_{3d} m_{3d} + a_{4s} m_{4s} \tag{5.1}$$

The first term corresponds to hyperfine field (generated by electrons belonging to the particular ion), the second to transferred field (due to neighbour ions), m_{3d} is spin magnetic moment of $3d$ electrons and m_{4s} is spin magnetic moment of $4s$ electrons of studied ion. These quantities are accessible from calculation results. Constants a_{3d} and a_{4s} were determined from comparison of calculations and experimental data. Their values (in $\mathrm{T}/\mu_\mathrm{B}$) are:

$$a_{3d} = -16.92,\ a_{4s} = 1229 \tag{5.2}$$

We used the above described method to calculate local fields on ^{57}Fe in several of studied systems. For this approach to work properly, atomic sphere

radius of iron should be set to two Bohr radii. It should be noted, that the correction works well only for ferric ions, once the ion starts to have ferrous character, it should still predict reasonable contact field, however accuracy of resulting local field is reduced.

Chapter 6

Size Effects

6.1 Introduction

In this chapter we present two studies on samples in which small grains size plays important role. First are oriented thin layers of SrM, and second are submicron particles of BaM of varying size. In most samples the hexaferrite particles were below single-domain limit and ^{57}Fe NMR spectra were altered by demagnetizing fields.

6.2 Effect of demagnetizing field

In general, presence of additional homogeneous magnetic field $\boldsymbol{B}_{\mathrm{ad}}$ (e.g. external field or demagnetizing field) in sample induces shifts of NMR resonance lines. Following text is aimed on ^{57}Fe NMR in ordered magnetics, i.e. we omit quadrupolar interaction (as it is not present) and assume that dominant component of local field is the contact contribution, which is oriented antiparallel with magnetic moment of the corresponding ion.

In case of collinear magnet the shifts for given isotope spectral lines are of equal magnitude, the sign is given by orientation of corresponding sublattice magnetization $\boldsymbol{M}$ with respect to the field. If $\boldsymbol{M}$ and $\boldsymbol{B}_{\mathrm{ad}}$ are parallel the line shifts to lower frequency by γB_{ad} and vice versa. In case of general orientation of $\boldsymbol{M}$ and $\boldsymbol{B}_{\mathrm{ad}}$, one can in most cases neglect the component of $\boldsymbol{B}_{\mathrm{ad}}$ perpendicular to $\boldsymbol{M}$, so:

$$\Delta\omega = \gamma \frac{\boldsymbol{M} \cdot \boldsymbol{B}_{\mathrm{ad}}}{M} \tag{6.1}$$

This is due to the facts, that intrinsic local field $\boldsymbol{B}_{\mathrm{in}}$ in ferric ions is of the order of tens of Tesla, so typically $B_{\mathrm{ad}} << B_{\mathrm{in}}$, and that magnetization is

nearly antiparallel with local field.

It should be noted, that frequency shift given by equation 6.1 does not include effect of local field anisotropy (equation 3.12) due to $\boldsymbol{B}_{\mathrm{ad}}$ changing orientation of magnetization. In the present case (demagnetizing field altering ^{57}Fe NMR spectra of magnetically hard hexaferrites) this mechanism is of minor importance.

In multidomain magnetic samples the distribution of domains is such, that contributions of magnetic moments outside the Lorentz sphere to local magnetic field on nuclear site do to great extent cancel out, since such distribution of magnetic domains lowers magnetostatic energy. In case of isolated single domain sample this argument no longer holds, hence an additional contribution to magnetic field on nucleus emerges – the demagnetizing field. In case of general sample shape, this field is inhomogeneous, if the sample is an ellipsoid, the demagnetizing field is homogeneous and proportional to the sample magnetization:

$$\boldsymbol{B}_{\mathbf{dem}} = -\mu_0 \boldsymbol{N} \cdot \boldsymbol{M} \tag{6.2}$$

Principal axes of the demagnetizing factor tensor $\boldsymbol{N}$ are identical with those of sample ellipsoid. If $\boldsymbol{M}$ is parallel with one sample axis, the demagnetizing field is antiparallel with $\boldsymbol{M}$ and its value is given by corresponding eigenvalue of demagnetizing factor tensor. All eigenvalues are within the range of $0 - 1$, zero corresponding to infinitely prolate sample magnetized along its longest axis, one to planar sample with magnetization perpendicular to it. In case of spherical sample the demagnetizing factor is (identity times) $1/3$.

In ideal case, one should be able to extract information on demagnetizing factor from observed zero external field NMR lineshifts induced by demagnetizing field, however, there are several complications, which lead both to line broadening and reduction of lineshifts:

- **Grain shape** The grains are not ellipsoids, so $\boldsymbol{B}_{\mathrm{dem}}$ is inhomogeneous, yielding a distribution of lineshifts (i.e. line broadening), further, there is a distribution of grain shapes which as well translates to distribution of lineshifts.

- **Intergrain interaction** Single domain magnetic particles produce strong stray fields, that affect resonance frequencies of nuclei in surrounding grains (e.g. in powder sample), thus again inducing line broadening. Further, since in every grain its magnetization will try to orient parallel with any magnetic field it experiences, the contributions of its own demagnetizing field to the lineshifts and of the external field from the rest of the sample will tend to compensate each other to some degree.

Despite these complications there are features typical for NMR spectra of collinear magnetics altered by demagnetizing fields (or in general by macroscopic magnetic fields):

- All lineshifts are of the same magnitude.
- All lineshapes are convolution of corresponding intrinsic lineshapes with the same profile or its mirror image, depending on orientation of the underlying sublattice magnetization.

The common profile then corresponds to distribution of projection of $\boldsymbol{B}_{\mathrm{ad}}$ to direction of magnetization.

6.3 SrM oriented layers

6.3.1 Samples

Samples of oriented SrM ferrite layers grown on 111 $SrTiO_3$ substrates have been prepared by J. Buršík from Institute of Inorganic Chemistry AS CR, v.v.i. by chemical solution deposition. Oriented thin layeres of SrM may be useful as substrates for oriented growth of more complicated hexaferrite structures. Resulting layers are polycrystalline, with oblate grains. Morphology of layer is sensitive to temperature at which it has been annealed, as observed by x–ray diffraction and SEM. With the temperature increasing from 600°C to 1100°C, the layer of originally randomly oriented ferrite grains develops high degree of orientation, when c–axes of individual grains are perpendicular to sample plane. Increased the annealing temperature also yields samples with larger grain size (diameter about one micron in hexagonal plane) and low porosity. Details on sample growth and characterization may be found in [53].

Two samples of the hexaferrite layers were studied by NMR. First sample was annealed at 800°C, which corresponds to an intermediate state, where orientation of grains is not yet perfect. The second was annealed at 1100°C, which produces larger and well oriented grains.

6.3.2 Results

Observed zero-field ^{57}Fe NMR spectra together with nested plots of fitted line profiles are plotted in figure 6.1, in the inserts the four spectral lines are plotted as shifted from resonant frequencies observed in bulk single crystal.

In comparison to the spectrum of a bulk SrM single crystal it is evident that the spectral lines of magnetic sublattices with magnetization parallel to

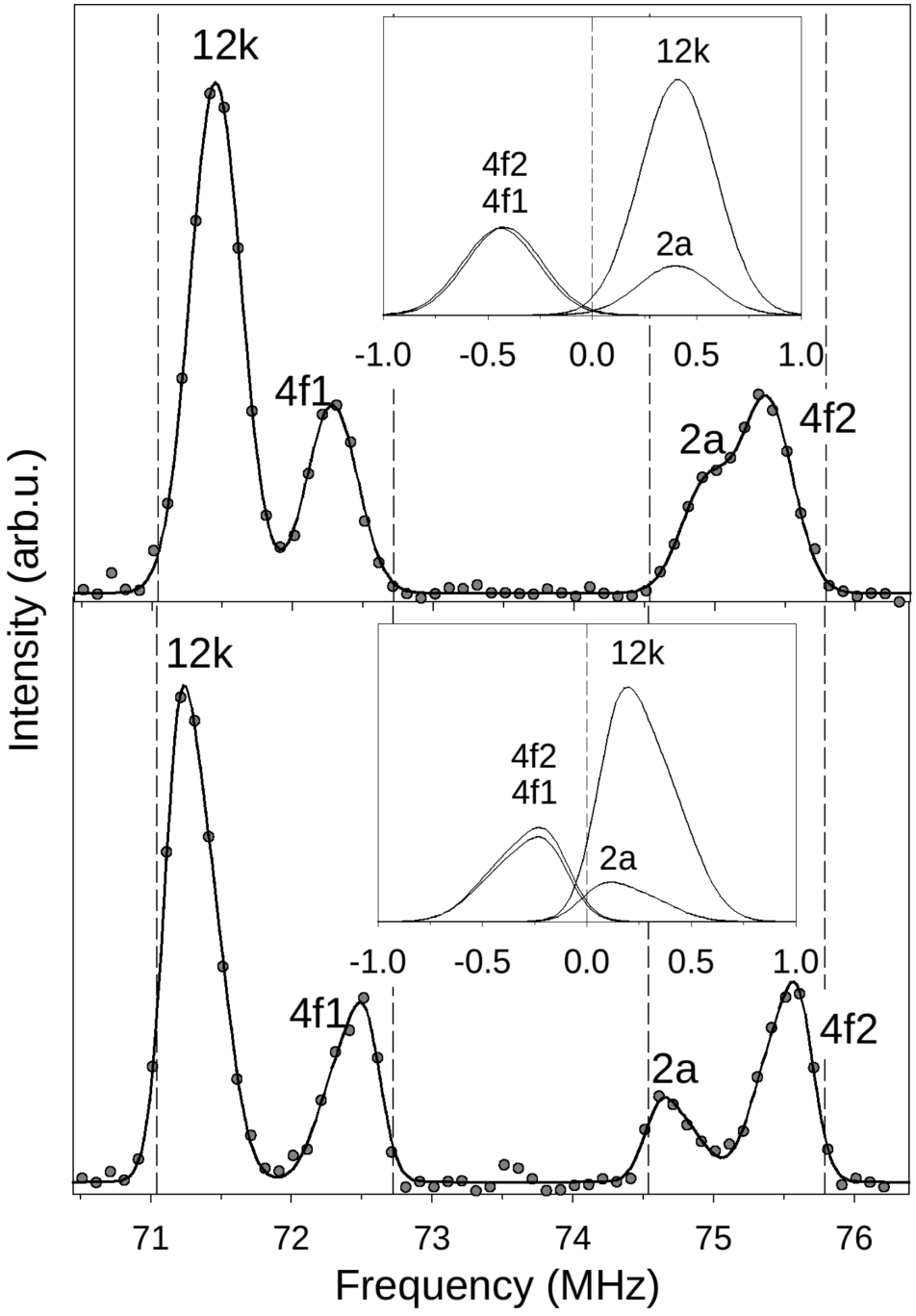

Figure 6.1: ^{57}Fe NMR spectra of sample crystallized at 800 °C (top) and 1100 °C (bottom). Circles are experimental points, lines are fits to the data. In the inserts are profiles of individual lines plotted as shifted from resonance frequencies in bulk material.

Site	Area	$f_{\max}$ (MHz)	f_{CMS} (MHz)	$\Delta f_{\max}$ (MHz)	Δf_{CMS} (MHz)
12k	5.9	71.24	71.30	+0.20	+0.26
$4f_1$	2.1	72.48	72.43	−0.24	−0.30
$2a$	0.9	74.66	74.72	+0.12	+0.18
$4f_2$	2.1	75.57	75.50	−0.22	−0.29

Table 6.1: Fit results for sample crystallized at 1100°C. $f_{\max}$ is frequency of line maximum and f_{CMS} is frequency of line centre of mass, $\Delta f_{\max}$ and Δf_{CMS} are shifts of this frequencies with respect to that observed in bulk material.

Site	Area	$f_{\max}$ (MHz)	f_{CMS} (MHz)	$\Delta f_{\max}$ (MHz)	Δf_{CMS} (MHz)
12k	5.8	71.45	71.45	+0.41	+0.41
$4f_1$	2.1	72.28	72.28	−0.40	−0.40
$2a$	1.1	74.94	74.94	+0.40	+0.40
$4f_2$	2.1	75.37	75.37	−0.42	−0.42

Table 6.2: Fit results for sample crystallized at 800°C. $f_{\max}$ is frequency of line maximum and f_{CMS} is frequency of line centre of mass, $\Delta f_{\max}$ and Δf_{CMS} are shifts of this frequencies with respect to that observed in bulk material.

total magnetization ($12k$ and $2a$, spin "up") are shifted to higher frequencies, while the lines of sublattices with antiparallel magnetization ($4f_1$ and $4f_2$, spin "down") are shifted to lower frequencies.

Shifts of lines found for the sample crystallized at 800°C are markedly (about 0.2MHz) higher relatively to sample crystallized at 1100°C. While the lineshifts of sample 800°C are nearly uniform, in case of sample crystallized at 1100°C the shift of $2a$ line is lower than those of the remaining lines. In addition, the lines are significantly broadened, having the linewidth of approximately 0.4MHz (corresponding to width of the distribution of magnetic field being about 0.3T) which is more than an order of magnitude higher than in the perfect single crystal.

Both spectra were fitted with four lines with common profile (mirror image of the profile was used for spin down sublattices). The fitted lines had variable intensity and center frequency. In case of sample crystallized at 1100°C asymmetric profile had to be used, for sample crystallized at 900°C a gaussian profile was sufficient. Intensities of individual lines and their frequencies obtained from fits are listed in tables 6.1 and 6.2

Good agreement of experimental and fitted spectra proves the validity of the presumption of spectra being altered mainly by demagnetization fields (and stray fields generated by neighboring particles). Integral intensities of individual resonance lines obtained from the fit well correspond to multiplicities

of underlying sites.

Assuming that magnetization of a grain is the same as of a bulk material, then the demagnetizing field within an isolated single domain grain should fall in range of 0–0.65T.

Fitted lineshape of the sample anneaed at 800°C is symmetrical and the lineshift corresponds to internal macroscopic field of 0.31 T. For an isolated single domain particle this value implies aspect ratio c/a equal to 0.62 (c and a being particle dimensions along and perpendicular to hexagonal axis respectively). Since the interparticle interaction reduces the internal field, the real c/a value is lower.

Lineshape of sample annealed at 1100°C is asymmetrical, fitted lineshape has approximately the same width as in 800°C, but its maximum as well as mean value are shifted towards single crystal values. Internal field corresponding to maximum of lineshape is approximately 0.15 T. Such demagnetizing field in single domain particle would imply needle like shape ($c/a > 1$), which have not been observed by SEM. Increase of inter-grain contribution should be held responsible for the low value of observed shift. It is an expectable outcome, for the grains in sample are well oriented, thus allowing more efficient compensation of demagnetizing and stray fields. Further, lateral grain size is about 1 μm, hence one should not exclude possibility of formation of domain walls, which, if present, would yield further reduction of the internal macroscopic fields.

Not perfectly uniform lineshifts ($2a$ shift is approximately half of other ones) in sample annealed at 1100°C indicate, that mechanism other than macroscopic field contributes to resulting spectrum. Additional effects, other than macroscopic fields, could bring along slight modification of electronic structure, which would alter hyperfine field in each iron site differently. Strains, or structural defects are the most probable candidates.

6.4 Submicron BaM particles

In this section we deal with particle size effect on NMR spectra of BaM ferrites and its implications for internal fields in the particles. We observed, that as particle size decreases further below single-domain limit, the spectra cannot be interpreted in terms of demagnetizing fields only and additional mechanisms have to be taken into account.

sample	A	B	C
σ_s at 15 kOe (Gcm^3/g)	63.6	60.2	21.6
σ_∞ extrapolated (Gcm^3/g)	69.3	64.1	23.3
Remanence ratio M_r/M_∞	0.49	0.50	0.31
H_c (Oe)	4046	2796	1780
Particle mean diameter (nm)	340	67	16
Particle mean thickness (nm)	90	11	not determined

Table 6.3: Basic characteristics of BaM powder samples obtained by VSM at room temperature and by TEM. σ_s is specific magnetization at 15 kOe, σ_∞ is an extrapolated value, H_c is coercive force.

6.4.1 Samples

We studied three samples of BaM particles of different mean particle sizes, the samples were prepared by glass crystallization by P. Görnert from Innovent e.V. Jena [54]. Additionally a high quality single crystal prepared by flux technique was used as reference.

The powder samples were characterized by electron microscopy (TEM) and magnetometry (VSM) at room temperature. The characteristics are given in table 6.3

6.4.2 Results

The ^{57}Fe NMR spectra were recorded at 4.2 K in zero external magnetic field using GPMG pulse sequence. Echo separation in the CPMG train was 400 μs for sample B and 180 μs for sample C.

Herein presented spectra correspond to signal from magnetic domains or from single domain particles. In sample A also a weak domain wall signal was observed, it was not found in samples B and C, which complies with their dimensions being well bellow single-domain limit.

Spectra of samples B and C displayed a dependence on which echoes from the CPMG train were used for their evaluation – spectra obtained from first echo differed from that corresponding to echoes further in the train, while in case of sample B there was only a slight difference, spectra of sample C varied significantly with sequential number of echo used for evaluation.

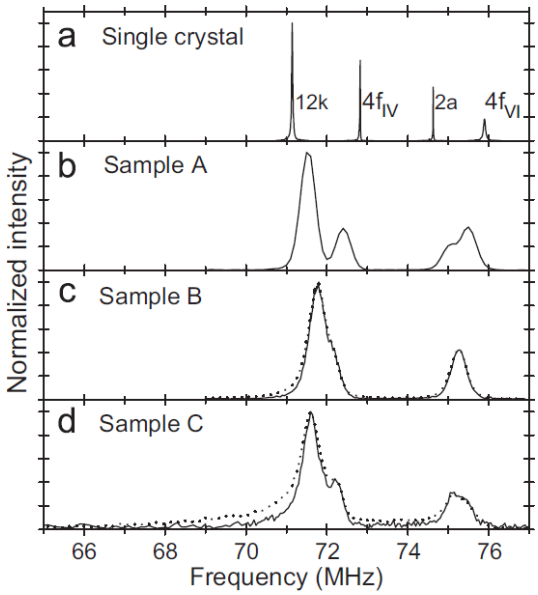

Figure 6.2: Normalized ^{57}Fe NMR spectra in region of $12k-4f_{\mathrm{VI}}$ resonance recorded at 4.2K in zero magnetic field. (a) single crystal; (b) sample A, (c) sample B, dotted – spectrum from echo no. 1, solid – spectrum from echo no. 50; (d) sample C, dotted – spectrum from echo no. 1, solid – spectrum from echo no. 20.

Observed spectra of BaM particles display shifts and broadening of resonance lines when compared to single crystal spectrum. Mechanisms inducing these changes may be broken up into two sets according to their effect on NMR pattern. The demagnetizing fields, which are always present in single-domain particles, induce shifts of equal magnitude for all lines with sign of the shift given by orientation of corresponding sublattice magnetization with respect to total magnetization. Point defects of ideal structure, deviations of magnetization from easy axis, noncollinearities in magnetic structure or reduction of static ionic magnetic moment due to missing exchange interactions near surface, they all induce broadenings, shifts or splittings which are site-specific, i.e. each resonance line is influenced in a unique way.

Normalized spectra of sample C are strongly dependent on sequential number of echo used for evaluation. This implies, that the observed signal is a sum of components with different T_2 relaxation times. We constructed spectra out of individual echoes and treated the resulting series by singular value decomposition (SVD) [55]. The results show, that the series can be broken up into two frequency profiles. The NMR spectral components were constructed out of

the SVD frequency profiles by requesting non-negative spectral intensities and single-exponential decay of the components. Both the criteria independently yielded the same transformation matrix between the SVD frequency profiles and NMR components, this means, that the SVD allowed for unambiguous determination of the NMR components. Relaxation times of components are 0.8 ms for the fast relaxing component and 5.0 ms for the slow relaxing one. The components are plotted in figure 6.3.

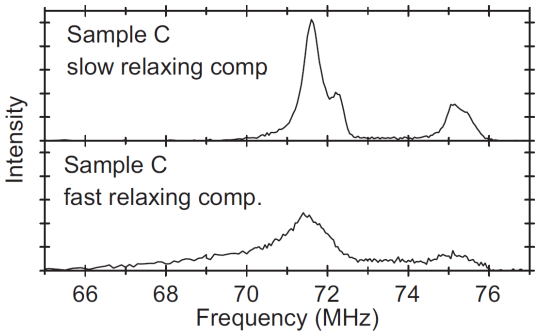

Figure 6.3: Slow and fast relaxing components obtained by SVD for ^{57}Fe NMR on sample C at 4.2 K. The components are plotted in the same intensity scale.

In order to compare all samples with respect to role of demagnetizing (or more generally macroscopic) fields in observed broadenings and shifts of resonance lines we decided to characterize samples by centers of masses of $12k+4f_{\mathrm{IV}}$ and $2a + 4f_{\mathrm{VI}}$ overlapped lines. These two numbers represent a point in a plane, since macroscopic magnetic fields induce shifts of equal magnitude for all sublattices, points representing samples with spectra altered solely by the macroscopic fields have to lie along a straight line, position on the line then corresponds to effective magnitude of the field. Since demagnetizing fields are expected to be important source of observed uniform shifts, we marked values of demagnetizing factor corresponding to the fields.

The line and positions of the samples in aforementioned plane are plotted in figure 6.4. While symbols of single crystal and sample A are well on the line corresponding to effect of macroscopic field only, the sample B is slightly deviated and both spectral components of sample C are considerably off the line. For both samples B and C the deviation is larger when fast relaxing component or (in case of sample B) only the first echo are evaluated. The large deviation of sample C fast relaxing component is due to low value of $12k+4f_{\mathrm{IV}}$ component, which is likely to be predominantly influenced by signal from $12k$ sublattice.

As samples B and A show little or no deviation from behavior of spectra

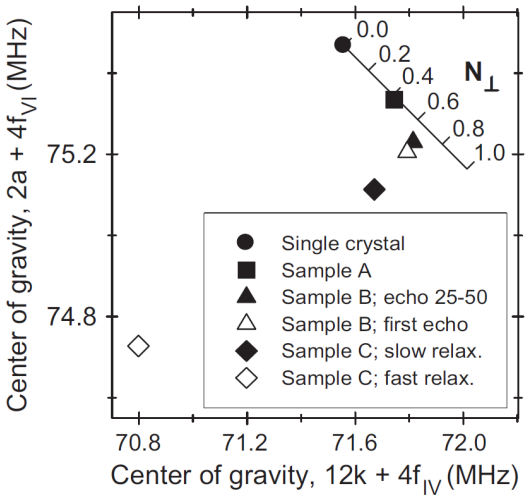

Figure 6.4: Center of mass for lines $12k + 4f_{\mathrm{IV}}$ versus $2a + 4f_{\mathrm{VI}}$ extracted from zero field spectra measured at 4.2K. Macroscopic magnetic field induces shifts which put sample symbol on the marked line, ticks denote values of demagnetizing factor required to generate corresponding demagnetizing field in homogeneously magnetized ellipsoidal sample.

expected from action of demagnetizing field, we fitted the spectra by sum of four Pearson functions with fixed intensities $12 : 4 : 2 : 4$, and common linewidth. In case of sample B spectrum evaluated from echoes $25 - 50$ was used. Results of the fits are in table 6.4, as one can see, the obtained lineshifts are reasonably uniform, which is in accord with demagnetizing fields being the dominant mechanism of line shifting and broadening.

It is interesting to compare demagnetizing fields observed by NMR (the field is proportional to observed lineshift by factor $\gamma_{\mathrm{Fe}} = 1.38\ \mathrm{MHzT}^{-1}$) with that expected from shape of particles. If one approximates the particles as homogeneously magnetized oblate rotational ellipsoids with dimensions given

sample	lineshift (MHz)					width (MHz)
	$12k$	$4f_{\mathrm{IV}}$	$2a$	$4f_{\mathrm{VI}}$	mean	
A	0.389	-0.402	0.417	-0.398	0.402	0.312
B					0.624	0.330

Table 6.4: Fit results for spectra of samples A and B (spectrum obtained from echoes $20 - 50$ was used in case of sample B). Mean lineshift is average magnitude of lineshifts obtained for the particular sample.

sample	$N_\perp$	demagnetizing field (T)	
		TEM	NMR
A	0.691	0.46	0.292
B	0.787	0.52	0.453

Table 6.5: Comparison of demagnetizing fields observed by NMR and calculated from particle size obtained from TEM.

in table 6.3 and magnetization along the shortest semi-principal axis one can calculate the expected demagnetizing fields as product of demagnetizing factor $N_\perp$ and bulk magnetization ($\mu_0 M = 0.66$ T [56]). The comparison is given in table 6.5. While in case of sample B there is reasonable agreement of observed demagnetizing fields (NMR column) and that expected for homogeneously magnetized ellipsoids (TEM column), in case of sample A the observed field is lower than expected from particle shape. This reduction is probably caused by residual shielding due to remaining domain structure which is present in sample A as documented by observation of weak domain wall signal.

The observed shifts and broadenings of $12k-4f_2$ resonance lines in samples A and B can be to ascribed to demagnetizing fields in single-domain particles. The observed lineshifts in samples A and B correspond to estimates of demagnetizing field based on particle dimensions in sample B and are smaller than the estimates for sample A, this is likely due to residues of domain structure in sample A.

In spectrum of sample C (smallest particles, size $\sim$ 16 nm) we identified additional component with shorter T_2 relaxation time. This component is spread out to lower frequencies, the low frequency signal is expected to be $12k$ resonance in surface layer. Weaker exchanges interactions in $12k$ sublattice or rotation of total magnetization out of hexagonal axis are possible causes of the low frequency signal.

6.5 Summary

Lowering particle size induces shifts of NMR frequencies due to emergence of macroscopic fields in the sample, as these fields add to intrinsic fields on nuclei resonance frequencies change. By comparison of demagnetizing fields estimated from particle shape and observed frequency shifts contribution of interparticle interaction to the macroscopic fields can be estimated. Upon further decrease of particle size influence of surface layer on NMR spectra becomes more pronounced.

Chapter 7

Y–type hexaferrites

7.1 Introduction

This chapter deals with $Ba_{2-x}Sr_xZn_2Y$ hexagonal ferrites, which have been studied for promising magnetoelectric (ME) properties of $x_{Sr} = 1.5$ system that in principle should persist up to room temperature [14, 57]. However, electrical conductivity of these materials increases with raising temperature and obscures the ME behavior.

Zinc is expected to preferentially enter tetrahedral sites [3, 4, 58, 59], these are: $6c_{IV}$ in S block and $6c^*_{IV}$ in T block. As there are 12 tetrahedral sites in hexagonal unit cell and only 6 Zn^{2+} cations, various distributions of zinc between the structural blocks are possible. To describe the distribution, γ parameter was introduced – fraction γ of all Zn^{2+} ions is in S blocks and $1-\gamma$ is in T blocks.

Electrical conductivity and ME behavior of the system are linked to γ. Electronic structure calculations indicate, that ideal Zn distribution is 50:50 ($\gamma = 1/2$) [60, 61], which might be achievable by annealing and subsequent quenching of samples.

Main goal of our efforts was to asses possibility of improving ME performance by thermal treatment. We employed NMR in combination with electronic structure calculations and of ME measurements (magnetocapacitance and electric polarization).

The NMR part of study was aimed on assessing Zn distribution (γ parameter) experimentally, to achieve this, electronic structure calculations of several Y–type systems with varying γ were performed. Resulting theoretical spectra were then used to interpret the experimental ones.

The ME experiments were done in order to gain information on actual effect of thermal treatment on ME performance of the very samples studied by

NMR thus allowing us to test hypothesis of link between magnetoelectrictity and zinc distribution directly.

Most effort was devoted to samples of magnetoelectric composition as these samples allowed for direct observation of ME effect (as well as NMR experiments), the other compositions were studied by NMR only.

7.2 Samples

We studied several samples of Y–type Ba–Sr hexaferrites which came from group of T. Kimura, from Osaka University who provided us with single crystals of $Ba_{2-x}Sr_xZn_2Y$ ($x = 0, 1.4, 1.5$), the crystals were grown by Y. Hiraoka using a Na2O-Fe2O3 flux technique in Pt crucibles [62].

The ME single crystals ($x = 1.5$) were prepared in two batches. Sample from the first batch was used for preliminary tests and NMR experiments in external magnetic field, while a more detailed study of effects of annealing was done on three samples selected from second batch (denoted as 1, 2, 5), which yielded larger crystals of higher quality than the first batch.

After measuring zero-field NMR spectra, the three samples from second batch were cut in half and one part of each sample was annealed in oxygen atmosphere (table 7.2), the other was kept as-grown for reference. The reference parts are denoted 1NA, 2NA, 5NA, numbers correspond to that of original crystals, NA stands for non-annealed, the annealed parts are denoted in similar fashion as 1A, 2A and 5A. The resulting six samples were cut into planparallel plates and silver electrodes were evaporated on the planar surfaces (see table 7.3 for their dimensions), the plates were then studied by ME and NMR techniques.

Further we also studied one $x = 1.4$ and four $x = 0$ small single crystals (tens of mg each), these compositions are not multiferroic, but the samples were used to asses influence of Ba–Sr ratio on NMR spectra.

The above review of samples is summarized in table 7.1.

sample	experiments
$x = 0$	^{57}Fe and ^{67}Zn NMR in zero field
	^{57}Fe and ^{67}Zn NMR in external field
$x = 1.4$	^{57}Fe NMR in zero field
$x = 1.5$	^{57}Fe and ^{67}Zn NMR in zero field
first batch	^{57}Fe and ZnN NMR in external field
	preliminary ME and annealing experiments
$x = 1.5$	three crystals (denoted 1, 2, 5)
second batch	^{57}Fe and ^{67}Zn NMR in zero field on all crystals
	annealing of part of each crystal (table 7.2)
	ME on resulting six crystals (denoted 1NA, 1A,
	2NA, 2A, 5NA, 5A)
	^{67}Zn NMR on annealed crystals and one reference crystal

Table 7.1: Summary of Y–type hexaferrite samples and performed experiments.

sample	temperature (°C)	time (days)	cooling
1A	900	8	fast
2A	900	7	slow
5A	800	7	slow

Table 7.2: Annealing of samples from second batch. The annealing took place in flowing oxygen gas. Fast cooling corresponds to removing sample from hot furnace, slow cooling to temperature drop at rate 1°C/min.

sample	area (mm^2)	thickness (mm)
1NA	2.3	0.25
1A	2.8	0.5
2NA	3.0	0.8
2A	3.0	0.4
5NA	5.1	0.6
5A	4.7	0.8

Table 7.3: Electrode areas and thicknesses of samples from the second batch.

7.3 Electronic structure calculations

The main goal of electronic structure calculations was to determine influence of Zn distribution on ^{67}Zn NMR spectra, which would than be used in to estimate γ of real samples and its changes due to thermal treatments.

The calculations were done on $Ba_2Zn_2Fe_{12}O_{22}$ for three different distributions of small cations corresponding to $\gamma = \{0; 0.5; 1\}$ (in order to achieve feasible computation time the Ba–Sr substitution was not considered). There are two Zn atoms in rhombohedral unit cell and four tetrahedral sites which can be occupied either by Zn or by Fe (two equivalent sites in S block and two in T block). Unit cell in $\gamma = 1$ case had both Zn atoms in S block, $\gamma = 0.5$ had one in each block and $\gamma = 0$ both Zn atoms were in T block tetrahedral sites. Owing to this simplifications there was no need for supercell. In all three cases lattice parameters (unit cell volume and c/a ratio) as well as free parameters in atomic positions within the unit cell were optimized.

Result of the calculations were electric and magnetic hyperfine parameters on ^{67}Zn sites in two situations: either all three nearest tetrahedral neighbors were Zn or they were Fe ions. The calculated parameters are in table 7.4, all tetrahedral sites have threefold symmetry axis parallel with hexagonal axis – the EFG tensors have zero asymmetry, the local z axes (axes of symmetry) are parallel with hexagonal axis of unit cell. In order to estimate hyperfine parameters for cases with one or two Zn nearest neighbors we employed linear superposition scheme:

$$P_n = \frac{1}{3}\left(nP_3 + (3-n)P_0\right);\ n = 1, 2 \tag{7.1}$$

where P_n stands for a hyperfine parameter (V_{zz}, B_{loc}) of nucleus with n nearest neighbors being Zn ions.

	S block		T block	
	nn:Zn	nn:Fe	nn:Zn	nn:Fe
V_{zz} ($10^{21}\mathrm{Vm}^{-2}$)	1.755	1.504	3.514	1.787
η	0	0	0	0
B_{loc} (T)	10.248	10.384	8.931	11.387

Table 7.4: Calculated hyperfine parameters on Zn in tetrahedral sites of Ba_2Zn_2Y.

7.3.1 Modelling of ^{67}Zn NMR spectra

In order to estimate influence of γ on spectra we calculated hyperfine parameters on Zn nuclear site in both S and T block. For each block we got 4 sets of hyperfine parameters corresponding to $0-3$ nearest tetrahedral neighbors being Zn (while the rest is Fe).

The NMR spectra for given value of γ were then calculated as follows:

1. Using Fermi golden rule (equations 3.4 and 3.5) and calculated hyperfine parameters, 8 sets of line positions and relative intensities were found corresponding to ^{67}Zn being in S or T block and its $n \in \{0,1,2,3\}$ nearest tetrahedral neighbors being Zn cations. Let those sets be S_n and T_n (e.g. S_2 corresponds to ^{67}Zn being in S block and having 2 nn Zn).

   ^{67}Zn has spin 5/2 hence in general case there are up to 15 observable nuclear transitions – each set may be expressed as:

$$X_n(\omega) = \sum_{i=1}^{15} I_i^{X,n} \delta(\omega - \omega_i^{X,n}) \; ; X \in \{S,T\}$$

2. Using binomial distribution, probability p_n^X of ^{67}Zn in S or T block having n Zn nearest tetrahedral neighbors was estimated.

3. Subspectra of S and T blocks were calculated as $X = \sum_n X_n * p_n^X$, by summing the S and T subspectra we obtained the whole spectrum. In the end, convolution of the calculated spectrum with squared lorentzian has been done in order to get a smooth profile.

Resulting spectra for several values of γ are shown in figure 7.1 together with subspectra from S and T blocks. Both subspectra are broadened by substantial contribution of quadrupolar interaction. While the S block subspectrum does not change its shape considerably with γ, the T block contribution shifts to higher frequencies as γ decreases. This is mere reflection of fact that while in S block the calculated hyperfine parameters are not much changed upon changing the nearest neighbors from iron to zinc, in T block the parameters vary significantly upon change of species in nearest tetrahedral sites (see table 7.4). Also the T block subspectrum is broader than that from S block as in T block there is stronger quadrupolar interaction.

The resulting lineshape is strongly dependent on value of γ – as it decreases, relative amplitude of narrow S block subspectrum is reduced while broad T block component gains intensity and shifts to higher frequencies.

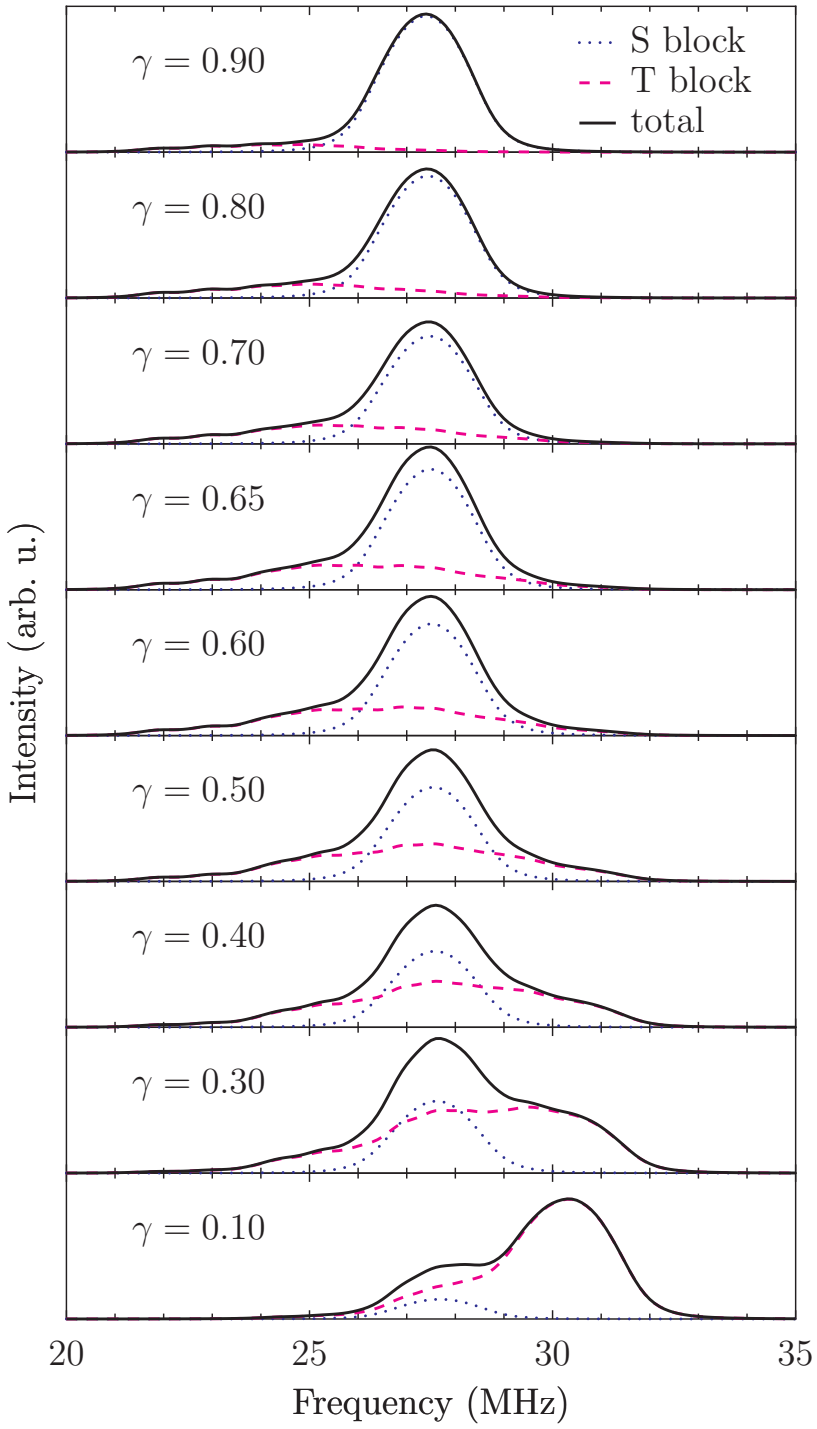

Figure 7.1: Calculated ^{67}Zn spectra and contributions from S and T blocks for varying γ–fraction.

7.4 Experimental NMR spectra

In this section we will present experimental NMR spectra of studied Y–type hexagonal ferrites. All NMR spectra were recorded at 4.2K.

7.4.1 ^{57}Fe resonance

Zero-field spectra of ^{57}Fe NMR of studied samples with different Sr content are shown in figure 7.2. When untuned probehead was used ($x_{\mathrm{Sr}} = 0$, 1.4) the spectra depended on excitation conditions. In order to correct for this effect we recorded spectra at several rf power levels and constructed resulting spectrum as their envelope. While this approach ensures optimal excitation in whole frequency range it does not eliminate modulation of observed lineshape originating from frequency dependent sensitivity of signal detection [63].

The spectra lie in frequency interval $65 - 78$ MHz, most intensity is in interval 65–70 MHz in unresolved broad peak centered at about 69 MHz for all three Sr contents. Most pronounced differences between samples are found in interval 70–73 MHz. Last there are two weaker peaks at 74.5 MHz and 77 MHz which are again found in all three samples.

Next we measured ^{57}Fe spectra of $x_{\mathrm{Sr}} = 0, 1.5$ samples in external magnetic field using untuned probehead. The external field was in both cases parallel with hexagonal axis of crystals – electron magnetization was forced by the field out of the easy plane. Spectra of $x_{\mathrm{Sr}} = 0$ crystal are in figure 7.3, these of $x_{\mathrm{Sr}} = 1.5$ are in figure 7.4 (in this experiment we used the crystal from the first batch).

Spectra of both samples show quite similar development in external field – the strongest peak with maximum at 69 MHz in zero field splits into two components, peak at 71.5MHz shifts to higher frequencies with increasing field, the two weaker peaks at 74.5 MHz and 77 MHz shift to lower frequencies and the small narrow peak overlapped with that at 77MHz shifts to higher frequencies.

The $x_{\mathrm{Sr}} = 1.5$ sample from the first batch, which was used in external field experiments turned out to be rather peculiar in comparison with samples of nominally identical composition from second batch. Its NMR spectra were dependent on direction of rf field – there were two possible NMR patterns depending on whether the rf field was in or perpendicular to hexagonal plane of the sample.

When the rf field was perpendicular to hexagonal plane, the NMR pattern was similar to the typical one (described above and shown in figure 7.2), however relatively weak, while when the rf field was in the hexagonal plane, the other, anomalous, pattern emerged, which was observed only for this sam-

ple. Further, when the sample was cooled and then temporarily exposed to magnetic field (0.01 T was sufficient) this anomalous spectrum switched to "normal" one.

There is one marked difference between "normal" spectrum of the sample and spectra of samples from second batch – additional peak centered slightly bellow 76 MHz, which is found only in spectrum of the sample from first batch. This peak appears to shift to higher frequencies as external field is applied, however for fields above 0.5 T it either vanishes or it merges with peak which found at 77MHz in zero field.

The anomalous pattern observed for sample from first batch indicates, that in this sample after zero field cooling the magnetic structure is likely different than in these from second batch. Upon application of external field the magnetic structure changed and yielded spectra more resembling these observed on samples from second batch. However as this hysteresis of NMR spectra was observed only for single sample details its origin were not further investigated.

Interpretation of ^{57}Fe NMR spectra is complicated for several reasons and as result unambiguous assignment of spectral lines to individual sublattices is not possible. The main factors hampering the line assignment are:

- substantial linewidth – individual contributions to resulting spectrum overlap strongly and cannot be separated.

- complicated subspectra – contributions coming from individual sublattices do not necessarily consist of single resonance line. There are two independent factors in play – disorder in small as well as large cation sublattices (Ba–Sr, and Fe–Zn substitution), which leads to to emergence of satellite patterns and anisotropy of local field, which can lead to additional line splitting.

Despite these complications the spectra can be partially interpreted when results of experiments in external field are used.

Due to orientation of external field parallel with hexagonal axes of studied samples one cannot expect signals from individual sublattices to shift linearly with the field even in case that magnetic structure is collinear – the magnetization is gradually rotated into direction of hard axis contribution of external field itself to lineshift is expected to be quadratic, additional nonlinear contributions arise from anisotropy of local field and tensor of demagnetizing factor. However this experiment still allows to distinguish sublattices with magnetizations parallel with the total magnetization (up) from the antiparallel (down) ones – the first shift to low frequencies while the latter to higher frequencies.

Given the collinear magnetic structure of Y–structure [64] (up: $18h_{\mathrm{VI}}$, $3a_{\mathrm{VI}}$, $3b_{\mathrm{VI}}$, down: $6c_{\mathrm{IV}}$, $6c^{*}_{\mathrm{IV}}$, $6c_{\mathrm{VI}}$), the large peak at 69 MHz has to be composed

of overlapped subspectra from $18h_{\mathrm{VI}}$ and two of three $6c$ sublattices – then it should split in two components with ratio of intensities approximately 2:3, the peak at 71.5MHz, which shifts to high frequencies should belong to the remaining $6c$ sublattice. The two weaker peaks at 74.5 MHz and 77 MHz should correspond to resonances from $3b_{\mathrm{VI}}$ and $3a_{\mathrm{VI}}$ sublattices.

Last, there is small narrow signal slightly below 77 MHz which shifts to higher frequencies – its low intensity suggests that it corresponds to a defect in the structure, from shift we see, that magnetic moments of its ferric ions are antiparallel with total magnetization. Possible reason may be stacking faults in which R blocks are introduced into the structure. Such a fault should give three signals at frequencies near $2b$, $12k$ and $4f_{\mathrm{VI}}$ resonances in M–phase. The signal corresponding to $2b$ would most likely be below frequency range in which these spectra were recorded, analog of $12k$ at approximately 71MHz, where it can be obscured by strong resonances from Y–phase. Frequency of $4f_{\mathrm{VI}}$ signal in M–phase is slightly below 76 MHz it is likely, that its resonance in such a stacking fault shifts to higher frequency and gives rise to observed signal – such a shift is expectable, because in M ferrite the $4f_{\mathrm{VI}}$ resonance shifts to higher frequencies when magnetization is oriented perpendicular to hexagonal axis (effect of anisotropy of local field) [65, 66].

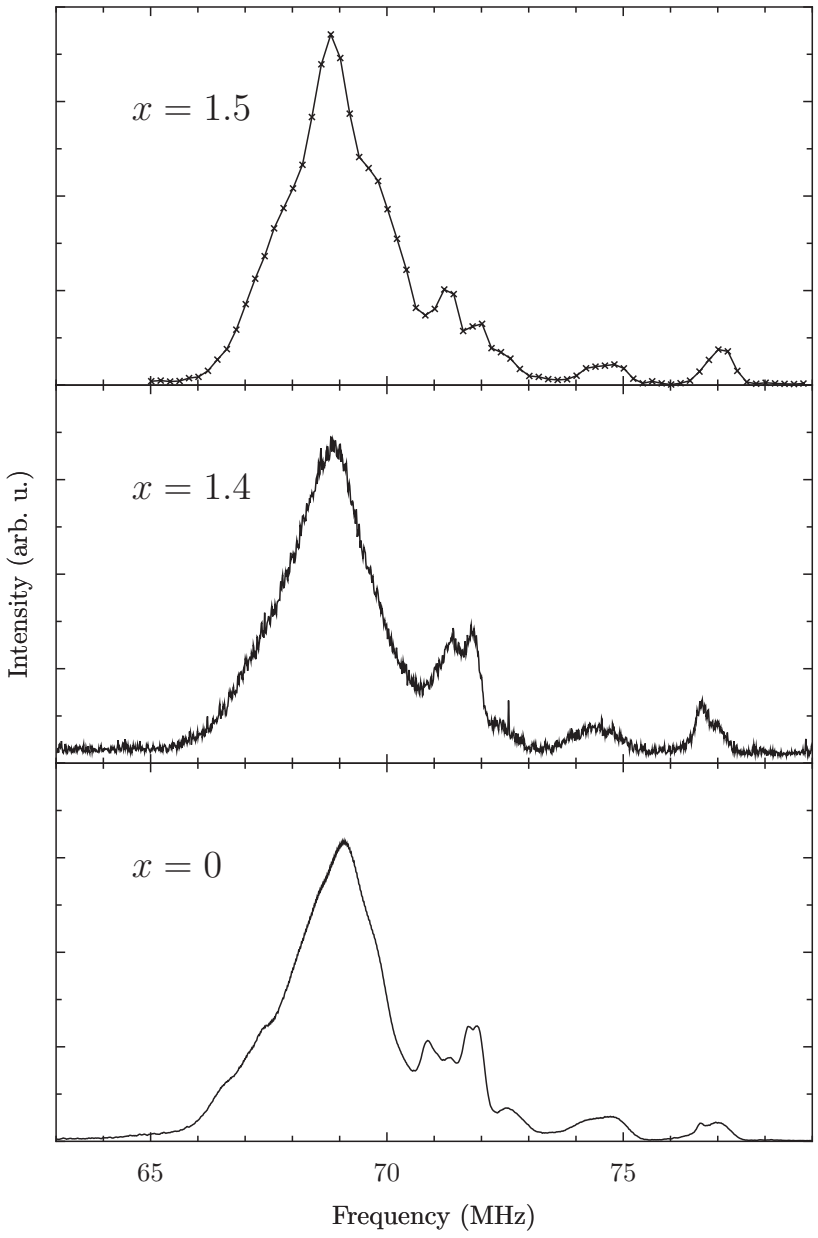

Figure 7.2: Spectra of $Ba_{2-x}Sr_xZn_2Fe_{12}O_{22}$ samples at 4.2K in zero external field. Except for $x = 1.5$ sample all spectra were recorded using a non-tuned probehead and constructed as envelope of three spectra recorded at different excitation conditions (rf power levels). The $x = 1.5$ spectrum was measured using a tuned probehead and on sample 2 from the second batch (the original crystal before cut). The spectra have been normalized to unit area.

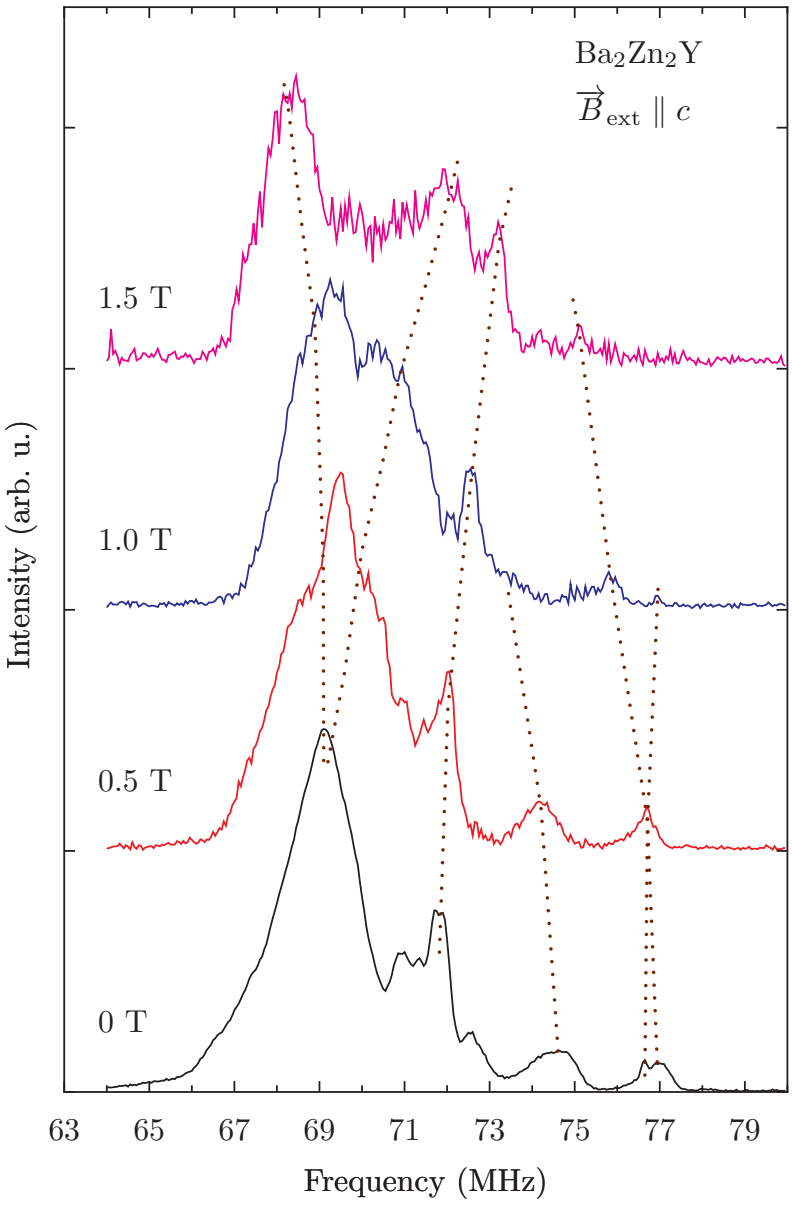

Figure 7.3: ^{57}Fe NMR spectra of $Ba_2Zn_2Fe_{12}O_{22}$ single crystal recorded at 4.2K in external magnetic field up to 1.5T. The field was oriented perpendicular to hexagonal plane of the crystal. Each shown spectrum is an envelope of three spectra recorded with different pulse intensities. The dotted lines track shifts of spectral features with increasing magnetic field. The spectra were normalized to unit area.

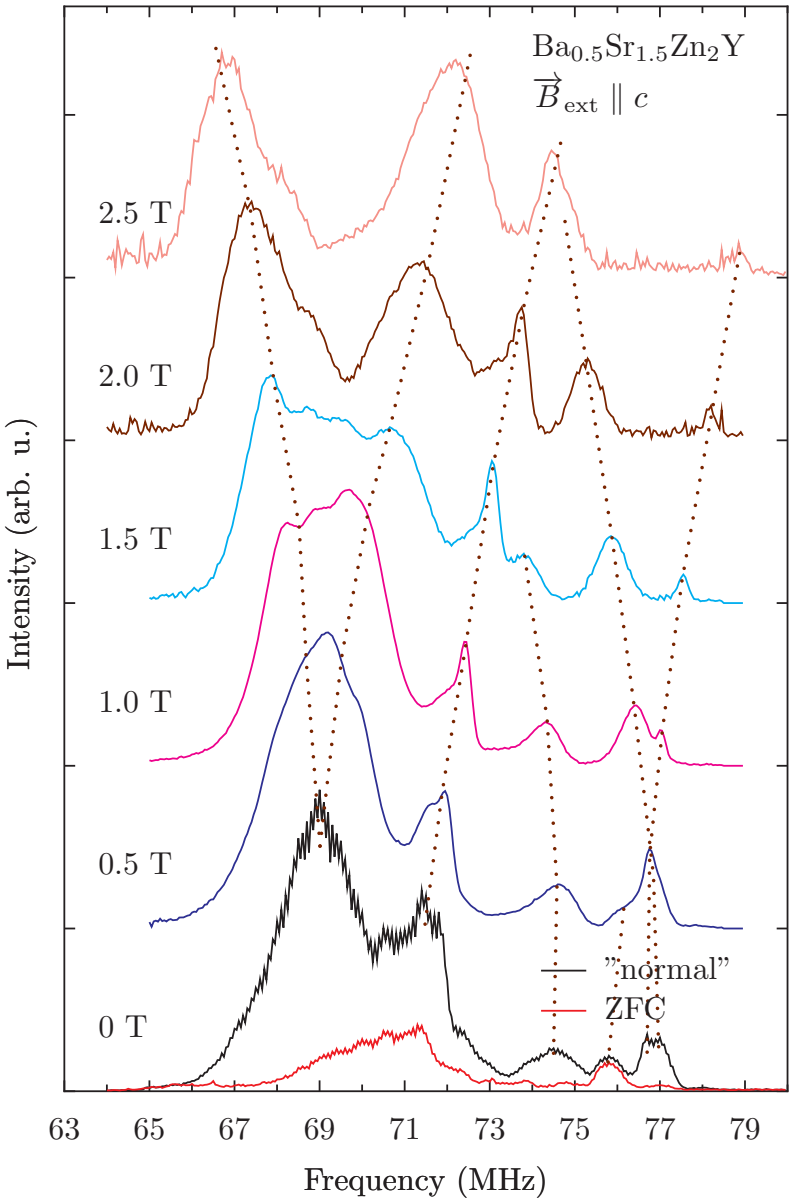

Figure 7.4: ^{57}Fe NMR spectra of $Ba_{0.5}Sr_{1.5}Zn_2Fe_{19}O_{19}$ single crystal from first batch. Spectra were recorded at 4.2K in external field up to 2.5 T. The field was oriented perpendicular to hexagonal plane of crystal. Each shown spectrum is envelope of three spectra measured with different excitation conditions. The dotted lines track shifts of spectral features with increasing magnetic field. Spectrum in zero field was dependent on sample history (see text). Except for "ZFC" spectrum all spectra are normalized to unit area. Ratio of "normal" and "ZFC" spectrum intensity corresponds to experiment.

7.4.2 ^{67}Zn resonance

Typical NMR spectra of ^{67}Zn are in figure 7.5, it is rather broad poorly resolved lineshape stretching from 10 MHz up to 30 MHz with relatively narrow maximum at 19 MHz.

We also performed measurements in external magnetic field results of which are in figure 7.6. This figure contains data obtained on two single crystals: sample with Sr content $x_{\mathrm{Sr}} = 0$ and $x_{\mathrm{Sr}} = 1.5$ crystal from the first batch. The first crystal ($x_{\mathrm{Sr}} = 0$) was oriented with static field in (magnetically easy) hexagonal plane and the observed resonance frequency dependence on external field soon becomes linear. We fitted the data with linear function (the first point from demagnetized sample at $B_{\mathrm{ext}} = 0$ was excluded from the fit). The second crystal was oriented with hexagonal plane perpendicular to external field. In this configuration, magnetization is gradually rotated by external field out of the easy-plane and resonance frequency dependence on the is field approximately quadratic. Results of the fits are in table 7.5.

In ^{67}Zn NMR experiments on $x_{\mathrm{Sr}} = 1.5$ sample from first batch we observed similar anomalies as in ^{57}Fe case (dependence on rf field orientation and history), however in this case, there was no signal on zero field cooled sample when rf field was in hexagonal plane.

Simulated spectra shown in figure 7.1 resemble the experimental ones (figures 7.5 and 7.12) in shape, however the frequency scale is rather off – the calculated spectra are shifted to higher frequencies and stretch over narrower frequency interval than the experimental ones. This is likely due to calculation of local magnetic field, namely the contact contribution, on zinc sites. The magnetic field, unlike the EFG, can be subject to large systematic error stemming from inaccurate description of electron exchange and correlation in DFT calculations. Despite these discrepancies the experimental as well as calculated lineshapes appear to be composed of narrow and broad component. Based on calculation results, we interpret the narrow peak at 19MHz as signal from S blocks and the broad component as signal from T blocks.

The two tetrahedral sublattices, which may be occupied by Zn ions, have their magnetizations parallel, hence separation of ^{67}Zn signals from S and T

Sample	Orientation	Fit function	Fit results
$x_{\mathrm{Sr}} = 0$	$\boldsymbol{B}_{\mathrm{ext}} \perp c$	$f_{\max} = {}^{l}f_0 + {}^{l}AB_{\mathrm{ext}}$	${}^{l}f_0 = 18.88 \pm 0.07$ MHz ${}^{l}A = 2.40 \pm 0.15$ MHzT^{-1}
$x_{\mathrm{Sr}} = 1.5$ first b.	$\boldsymbol{B}_{\mathrm{ext}} \parallel c$	$f_{\max} = {}^{q}f_0 + {}^{q}AB^2_{\mathrm{ext}}$	${}^{q}f_0 = 18.97 \pm 0.06$ MHz ${}^{q}A = 0.78 \pm 0.05$ MHzT^{-2}

Table 7.5: Fits of ^{67}Zn NMR data in external field (figure 7.6)

block by increasing magnetic field was neither expected nor observed. We focused on shifts of NMR signal maximum in external field in order to show that the resonance does come from ^{67}Zn nuclei.

In case of $x_{\mathrm{Sr}} = 0$ sample the field was in easy plane, further the magnetic structure is collinear for this composition, so as soon as the sample is in single domain state, the signal shift can be expected to be proportional to gyromagnetic ratio of zinc which is 2.68 MHz/T (dotted red line in figure 7.6). Due to quadrupole interaction the real dependence is more complex, however on average the signal shift is linear in with applied field and the slope is close to zinc gyromagnetic ratio.

In the second geometry, when external field is perpendicular to hexagonal plane ($x_{\mathrm{Sr}} = 1.5$ sample) the situation is more complex. Magnetization is forced out of easy plane and its orientation is given by competition of magnetocrystalline anisotropy and external field. Neglecting shape anisotropy and demagnetizing field, using only first term of magnetocrystalline anisotropy expression and neglecting possible dependence of magnitude of magnetization on external field one can obtain formula:

$$M B_{\mathrm{ext}} + 2K_1 \cos\theta = 0 \tag{7.2}$$

Where M is magnetization of the sample, B_{ext} external magnetic field, K_1 anisotropy constant ($K_1 < 0$) of sample material and θ angle between magnetization and hexagonal axis. If one further neglects demagnetizing field, local field anisotropy, quadrupolar contribution to resonance frequency and takes into account only component of external field parallel with magnetization, one arrives at (obviously) approximate relation for position of signal maximum:

$$f_{\max} = \begin{cases} f_0 - \frac{\gamma_{\mathrm{Zn}}}{2\pi} \frac{M}{2K_1} B_{\mathrm{ext}}^2 & \text{if } B_{\mathrm{ext}} < -2K_1/M \\ \\ f_0 + \frac{\gamma_{\mathrm{Zn}}}{2\pi} B_{\mathrm{ext}} & \text{if } B_{\mathrm{ext}} \geq -2K_1/M \end{cases} \tag{7.3}$$

When magnetization is rotated completely (i.e. it is parallel with the field), the dependence becomes (within the approximation) linear.

As one can see from figure 7.6 , magnetic field of 1.5 T is not sufficient to turn magnetization of the sample into the hard axis.

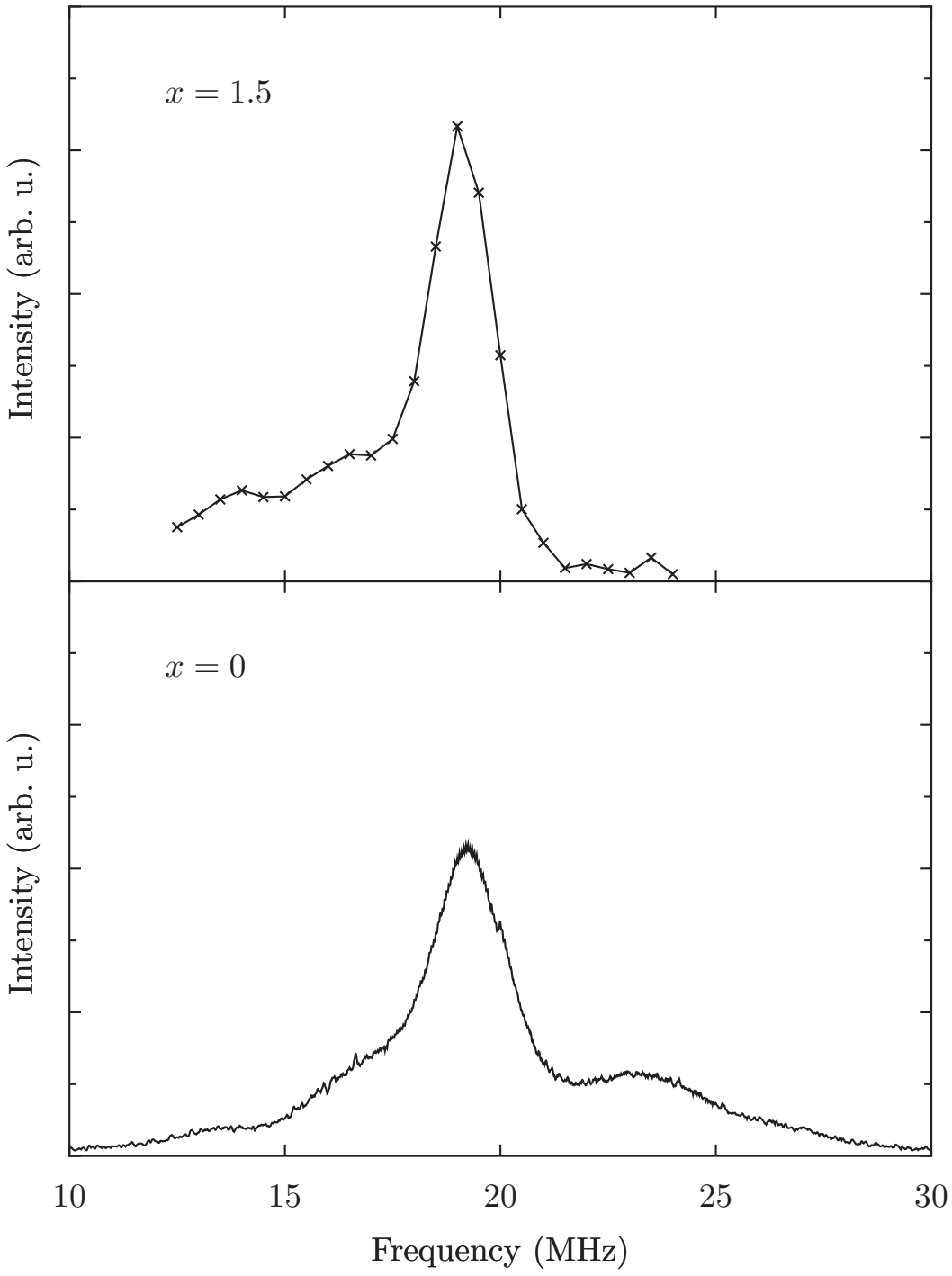

Figure 7.5: ^{67}Zn NMR spectra of $Ba_{2-x}Sr_xZn_2Y$ single crystals. Spectrum of $x = 0$ sample was measured using untuned probehead, $x = 1.5$ crystal (sample 2NA), spectrum was measured using tuned probehead.

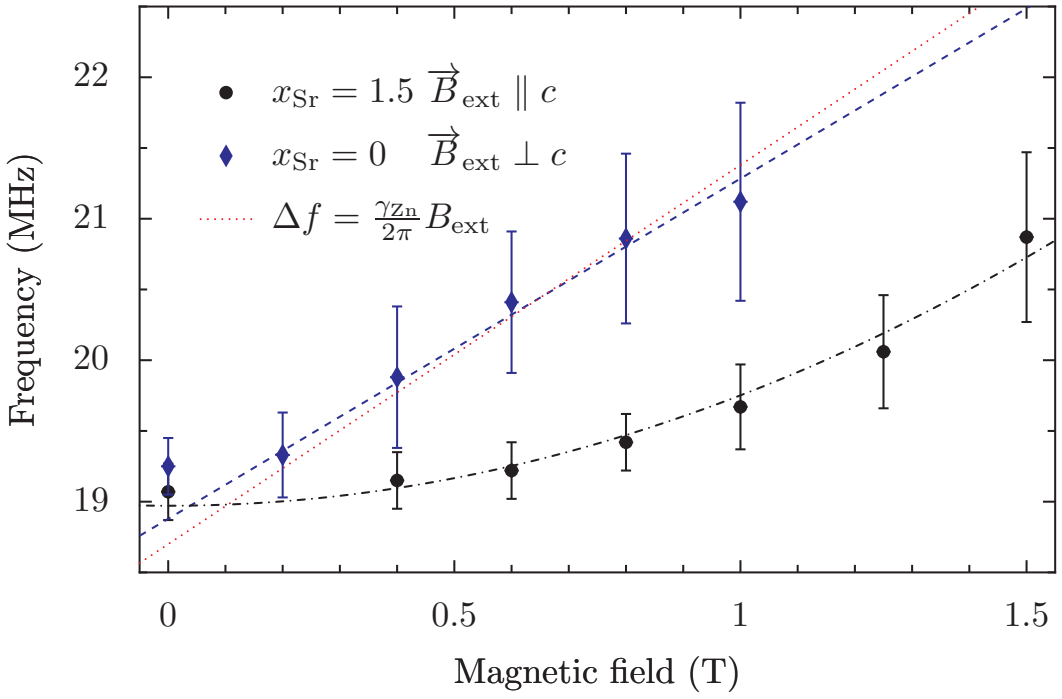

Figure 7.6: Positions of maxima of ^{67}Zn resonance in external magnetic field at 4.2 K. The $x_{Sr} = 0$ crystal was oriented to have (magnetically easy) hexagonal plane parallel with the field, while the $x_{Sr} = 1.5$ had the plane perpendicular to applied field. Data obtained on $x_{Sr} = 0$ were fitted with linear function disregarding the first point ($B_{ext} = 0$), fit is shown as dashed blue line. Data obtained on $x_{Sr} = 1.5$ crystal were fitted with quadratic function (black dash-dot line). Fit results are in table 7.5, slope of the red line is gyromagnetic ratio of ^{67}Zn .

7.5 Magnetoelectric Properties

We performed two types of ME experiments – magnetocapacitance (dependence of sample capacity on external magnetic field) and polarization (dependence of polarizing current on external magnetic field). Typically the magnetocapacitance curve shows two peaks, which indicate transitions to/from ME phase. The polarization experiment detects currents due to changes of sample electrical polarization, the currents are non-zero only in interval of magnetic fields corresponding to ME phase, sample electrical polarization is determined by time-integrating the currents.

7.5.1 Magnetocapacitance

The magnetocapacitance measurements were performed at four frequencies (1, 10, 100, 1000kHz), at 11 temperatures in range $4.2 - 300$ K on $Ba_{0.5}Sr_{1.5}Zn_2Fe_{12}O_{22}$ samples from the second batch. In these experiments magnetic field was swept from zero to 3 T and back at rate 1 T/min and capacitance of sample was recorded. Upon entering or leaving interval of magnetic fields in which ME phase exists characteristic maxima of sample capacitance were observed. At 300 K the lower magnetocapacitance maximu is located at zero field, hence the sweep from 3 T to low field was not stopped at zero field, but instead it was left to continue to negative values (i.e. increasing field of opposite direction was applied after reaching zero field). As an example of magnetocapacitance data we present results obtained on annealed part of sample 5, data recorded at 4.2 K and 100 K are shown in figure 7.7, those measured at 200 K and 300 K are in figure 7.8.

In general, as frequency decreases and temperature increases, intensity of noise and artifacts in the data increases and the magnetocapacitance maxima cease to be observable. At 4.2 K the second maximum (located at 2 T) is only poorly observable and there is slight hysteresis in the data – maxima observed on raising the field are shifted to slightly higher fields with respect to that observed on lowering field. Similar behavior was observed also at 20 K. At 40 K and above the data resemble that obtained at 100 K. The higher-field peak appears to be split into two, especially at temperatures above 100 K. Also at higher temperatures artifacts begin to obscure the magnetocapacitance peaks. Finally it is worth noting, that apparent capacitance of a sample increases dramatically with temperature, especially at low frequencies. These are most likely effect of (field dependent) sample conductivity increasing with temperature. The described features in magnetocapacitance data are common to all studied samples (hysteresis and weak high-field peak at low temperatures, splitting of high-field peak, increasing capacity).

We used the magnetocapacitance data obtained at 1 MHz to construct ME phase diagrams of the samples. The procedure is shown in figure 7.9, at each temperature four magnetic field were read from magnetocapacitance data – the fields at which the magnetocapacitance peaks reach half their total height. The fields obtained at different temperatures were then plotted into phase diagram breaking it up into three regions: magnetoelectric region, two transition regions (with widths given by widths of magnetocapacitance peaks) and the rest, where material is not magnetoelectric.

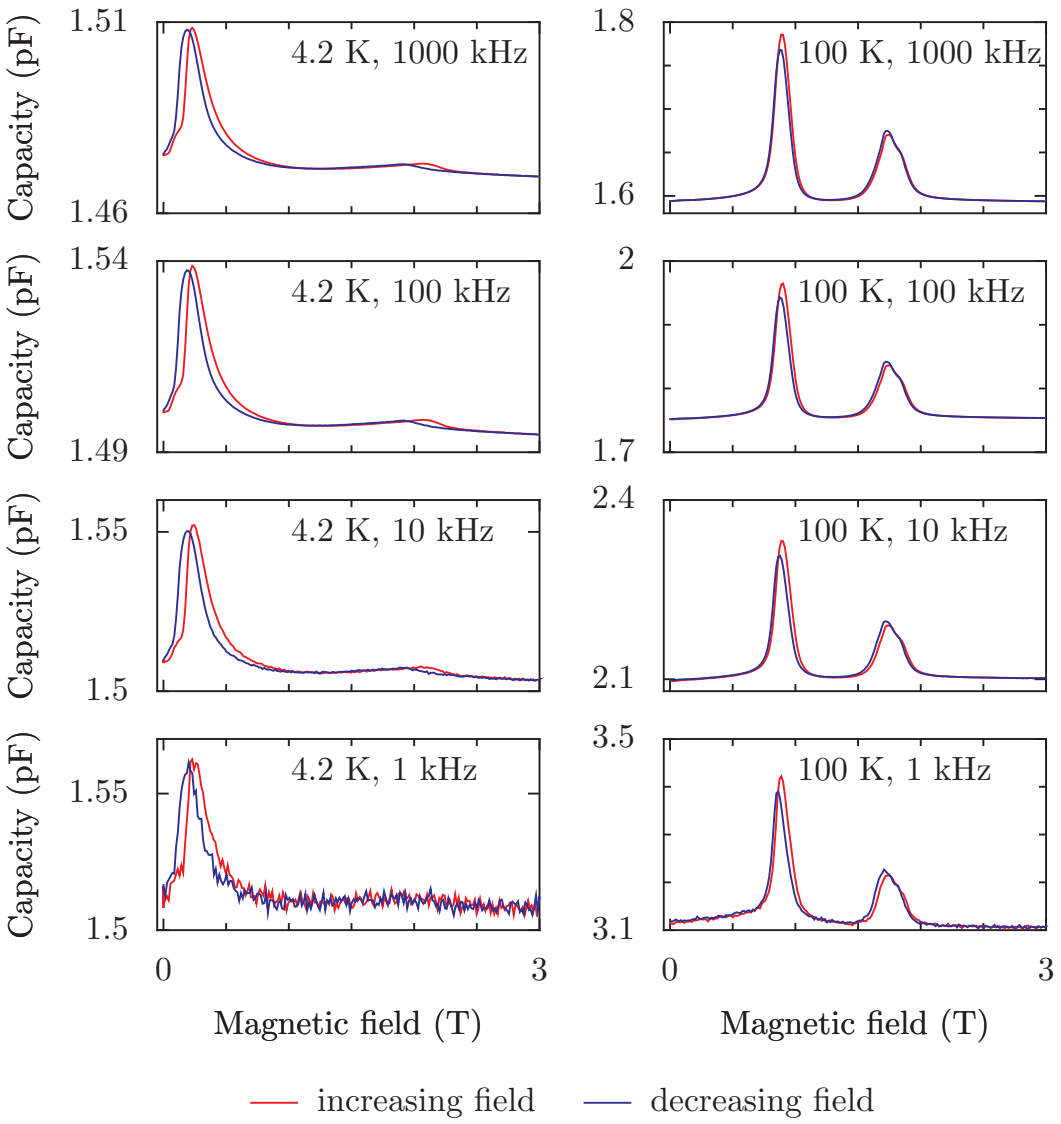

Figure 7.7: Magnetocapacitance results obtained on sample 5A at 4.2 K (left column) and 100 K (right column) at frequencies from 1kHz (bottom row) to 1MHz (top row). In each experiment field was swept from zero to 3 T and back. Data obtained on increasing field are shown in red, data obtained on decreasing field are in blue.

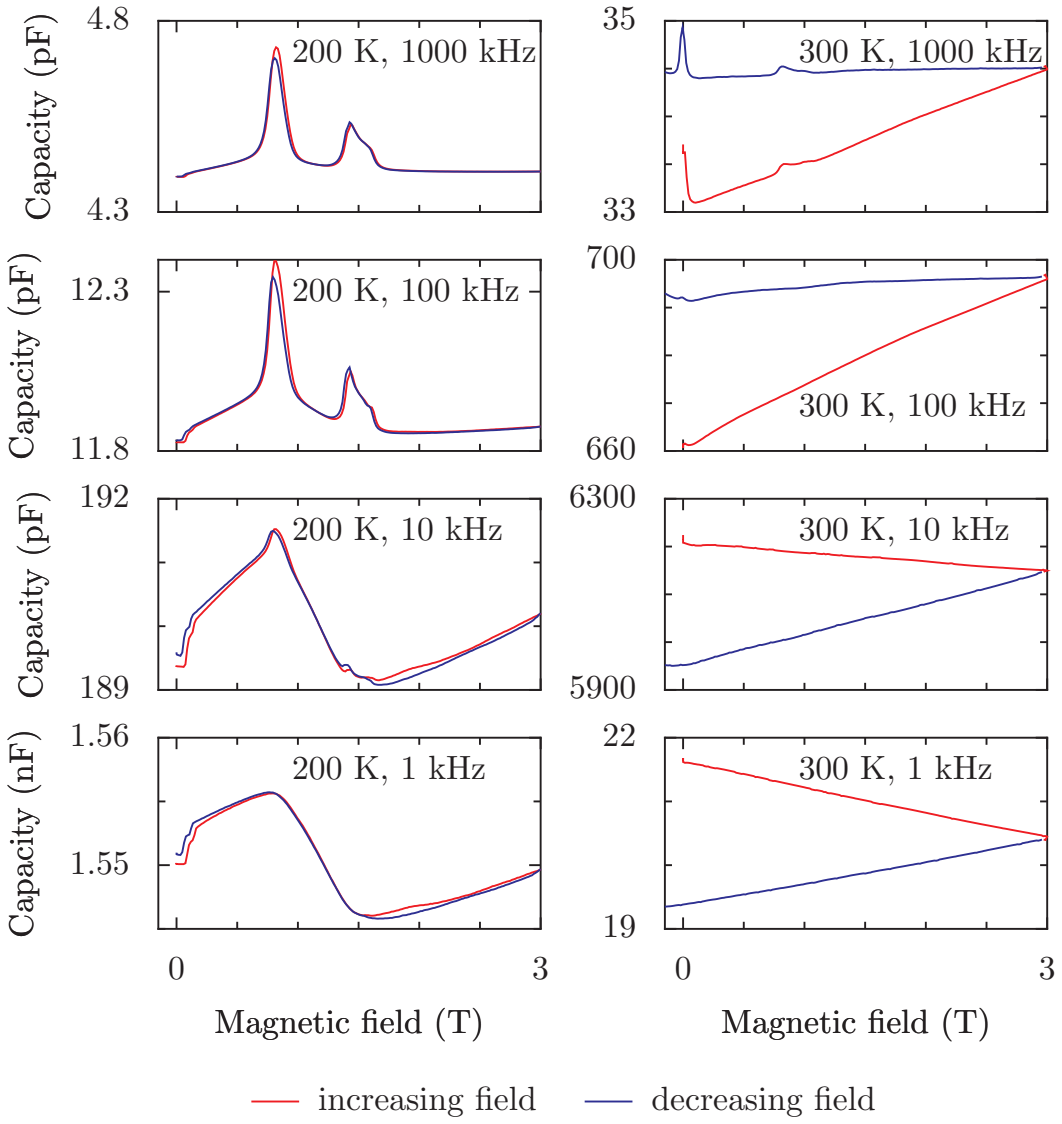

Figure 7.8: Magnetocapacitance results obtained on sample 5A at 200 K (left column) and 300 K (right column) at frequencies from 1kHz (bottom row) to 1MHz (top row). In each experiment field was swept from zero to 3 T and back, in experiments performed at 300 K the field was not stopped at zero but left to rise in negative values (i.e. opposite orientation). Data obtained on increasing field are shown in red, data obtained on decreasing field are in blue.

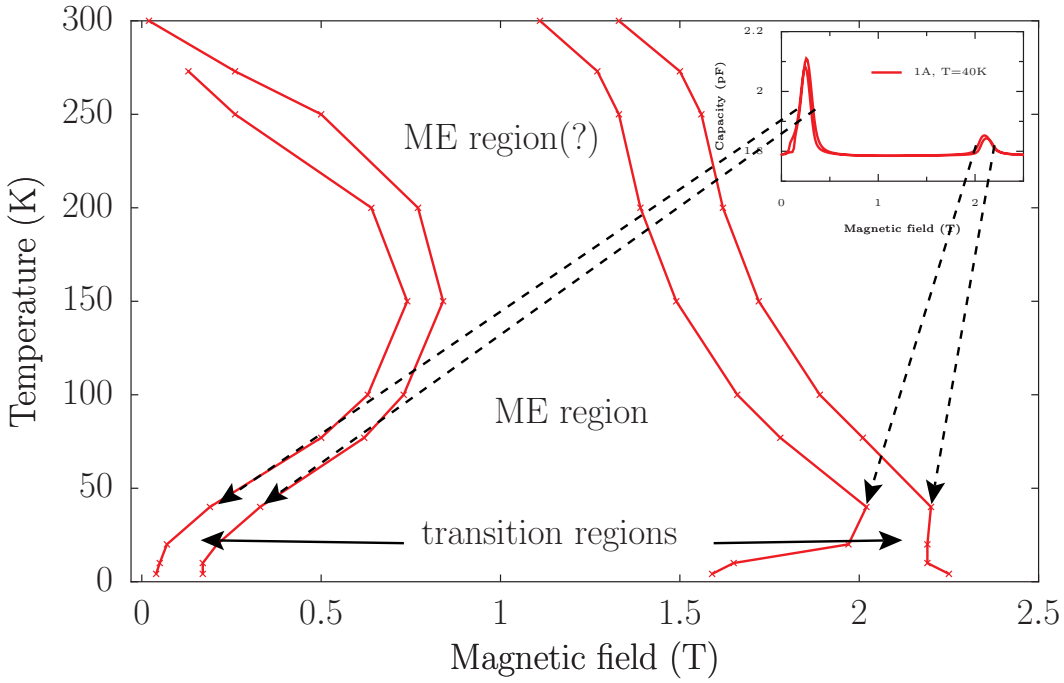

Figure 7.9: Illustration of how ME phase diagrams were constructed.

7.5.2 Polarization

Electrical polarization of samples was more difficult to observe, than changes of permittivity. Electrical conductivity of samples reduces measured depolarization current in zero bias voltage experiment, while in experiments with applied voltage it leads to parasitic current which adds to the observed currents induced by polarization changes. For this reasons we performed most experiments at 4.2 K with zero bias, as the main goal was to demonstrate presence of electrical polarization and to estimate its value.

After poling (applying voltage to sample while raising field to 1 T), depolarizing currents were measured in two situations – either field was swept to high values (up to 8 T, typically 5 T), subsequently reduced to zero and finally swept back to original 1T, or field was first reduced to zero, then increased to a high value and reduced back to 1 T, in both cases voltage bias was zero during the experiment.

Typical results of a polarization experiment are shown in figure 7.10. The peaks in depolarizing currents coincide with limits of ME region of magnetic fields determined from magnetocapacitance data thus indicating, that one can use the (easier to perform) magnetocapacitance experiment to estimate limits of ME region.

There is a stark difference between results of the two variants of polarization experiment described above – if field is first reduced to zero, no substantial polarization is recovered on its subsequent increase while when field is first increased to high value (we tested it up to 8 T) and then reduced back to values corresponding to the ME phase, the polarization is recovered. This evidences, that non-polar high-field phase contains information on orientation of electric polarization while the low-field phase does not. Collinear magnetic order in high-field phase is unlikely to play a role in the observed "memory effect", however if some non-collinearity was present in fields up to 8 T it could explain the observed behavior.

In figure 7.11 there is dependence of sample 2NA electrical polarization on magnetic field which was obtained by integration of depolarizing currents as field was swept out of ME interval. It can be seen that the polarization drops rapidly as field deviates from its original value. Peak value of the polarization is quite small compared to classical ferroelectrics.

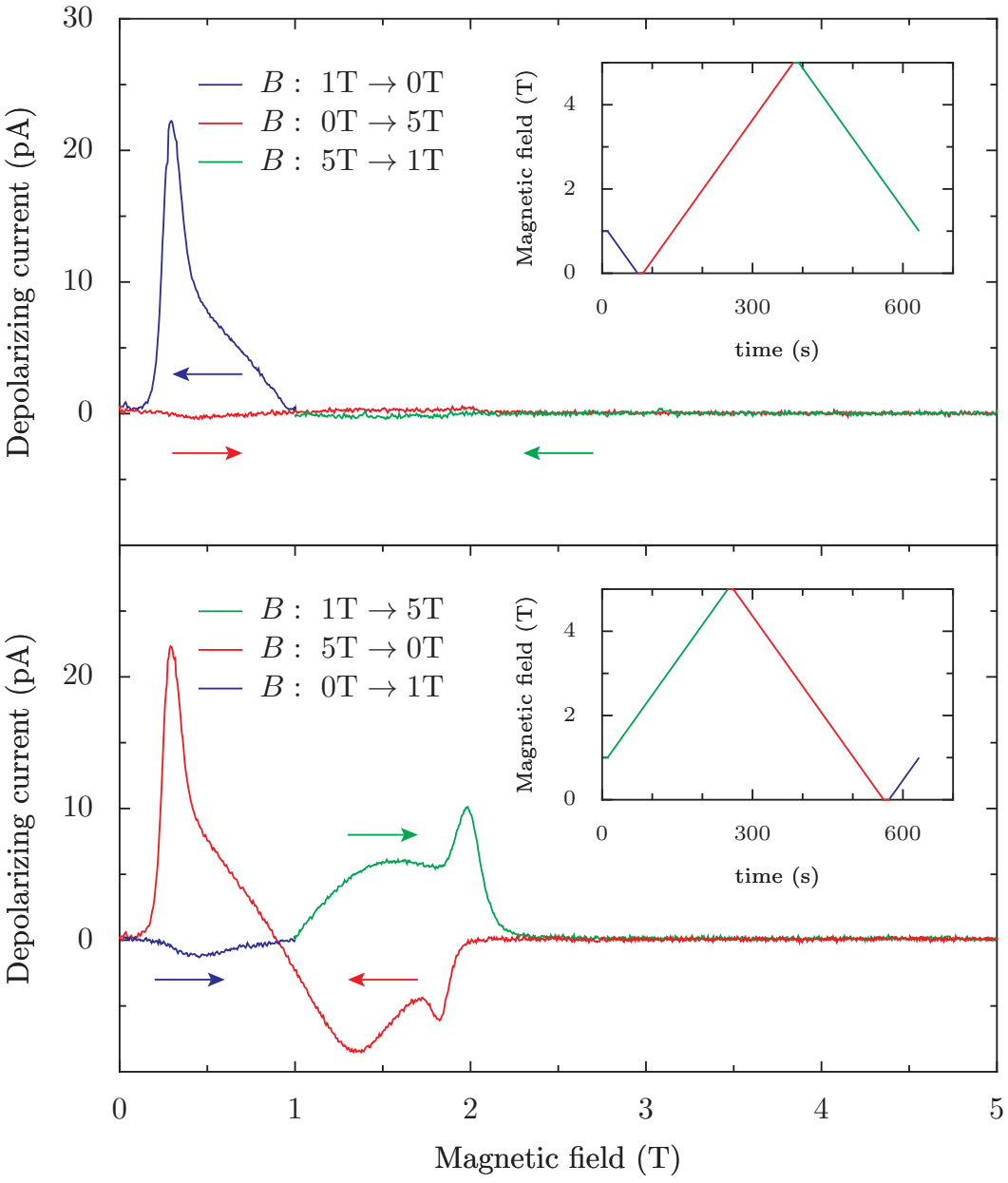

Figure 7.10: Depolarizing currents detected on non-annealed part of sample 2 at 4.2K. Top plot: after poling the sample magnetic field was decreased to zero, then increased to 5 T and reduced back to 1 T. Bottom plot: after poling the field was first increased to 5 T, then reduced to zero and finally increased back to 1 T. The inserts show time dependence of applied magnetic field, arrows indicate sense of magnetic field sweep.

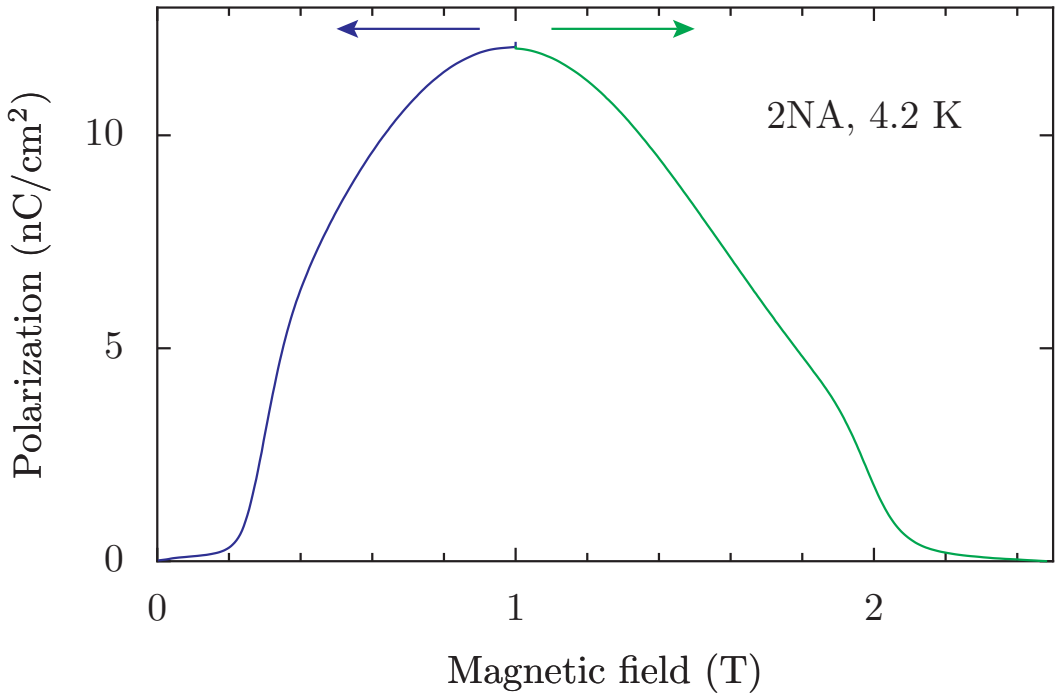

Figure 7.11: Dependence of electric polarization on magnetic field obtained by integration of depolarizing currents observed on sample 2NA at 4.2 K. The sample was poled at 1 T and then the field was swept to above 2.5 T or to zero. This yielded the two branches of polarization dependence on applied field.

7.6 Effect of annealing

7.6.1 NMR

To asses influence of annealing on actual distribution Zn cations between S and T blocks compared ^{67}Zn and ^{57}Fe NMR spectra of "as grown" samples from the second batch and annealed parts of the samples, or when feasible, we compared spectra of reference and annealed parts.

The main focus was on ^{67}Zn spectra, since results of electronic structure calculations allowed us to interpret the lineshapes in terms of Zn distribution (γ fraction), which was not case of the ^{57}Fe spectra.

Resulting ^{67}Zn spectra are in figure 7.12, ^{57}Fe spectra are in figure 7.13. One can see that there is no substantial change of lineshapes due to annealing. By comparison with calculated ^{67}Zn spectra 7.1 we estimated the γ to be about 0.65.

Minor effects of annealing on ^{67}Zn and ^{57}Fe spectra indicate, that changes of microstructure induced by the annealing are of subtle character. The invariance of ^{67}Zn profile implies that gamma is not significantly altered by the annealing.

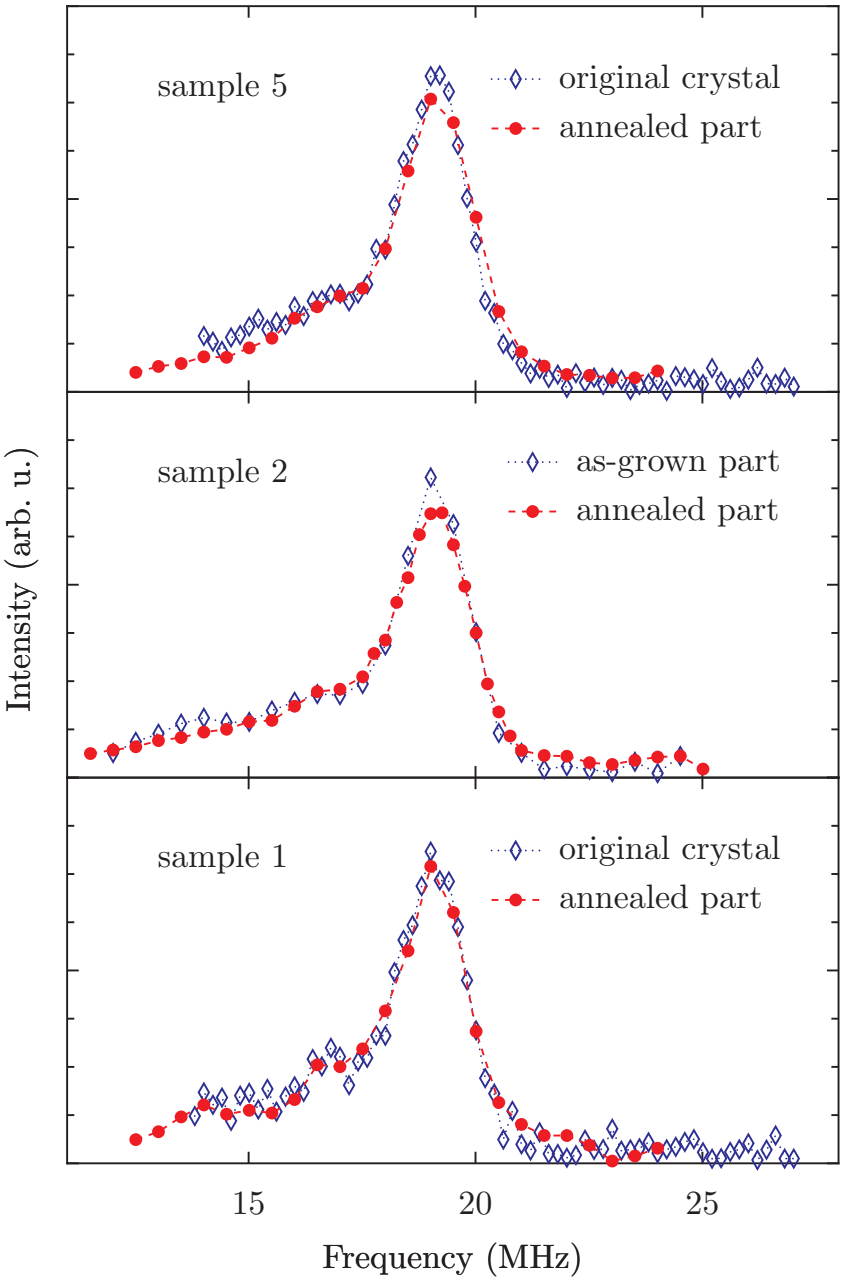

Figure 7.12: Comparison of ^{67}Zn NMR spectra of annealed and as grown parts of $Ba_{0.5}Sr_{1.5}Zn_2Y$ single crystals from second batch. Spectra were recorded using tuned probehead.

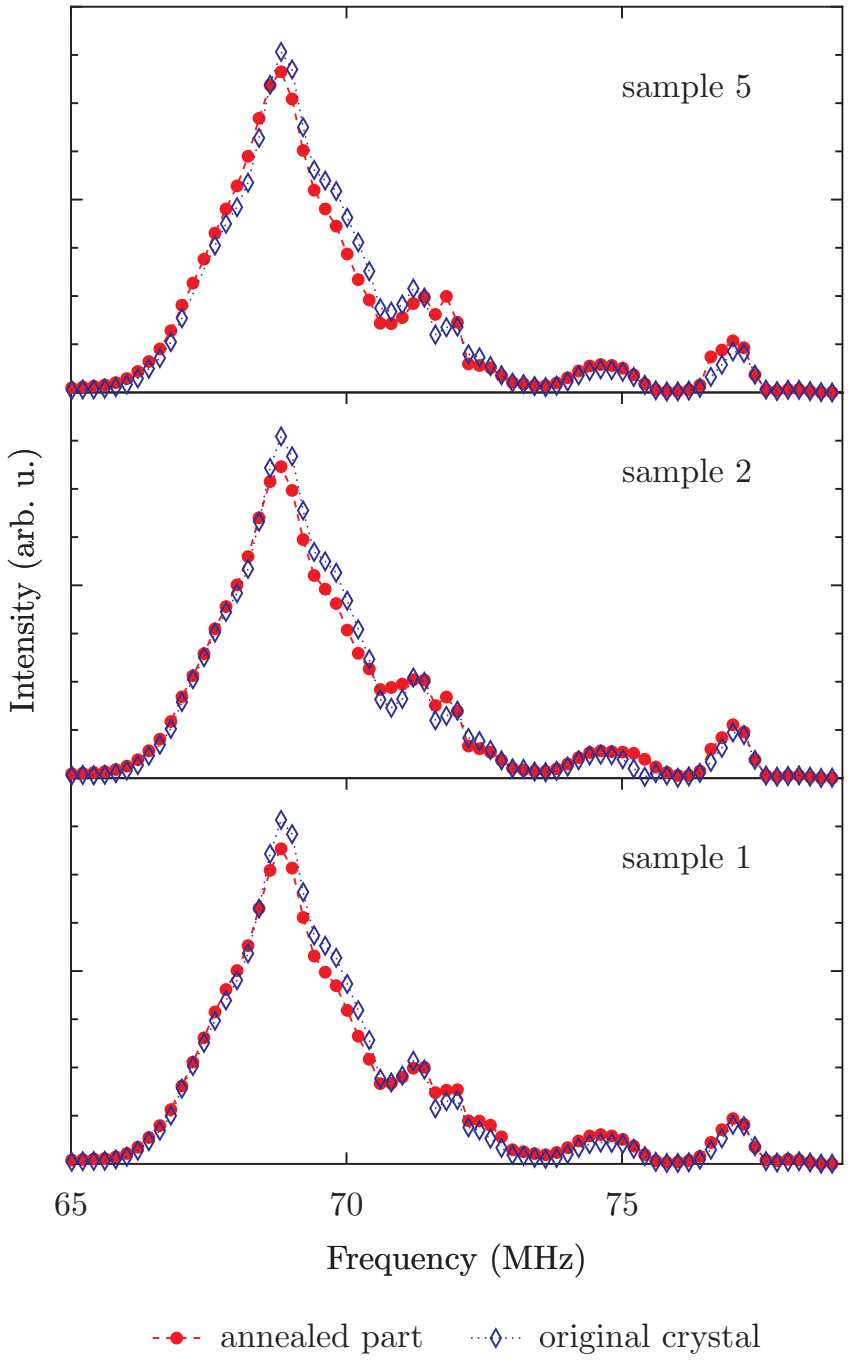

Figure 7.13: Comparison of ^{57}Fe NMR spectra of annealed and as grown parts of $Ba_{0.5}Sr_{1.5}Zn_2Y$ single crystals from second batch. Spectra were recorded using tuned probehead.

7.6.2 ME properties

Apart from attempting to learn about influence of annealing on microstructure of samples from NMR we also studied its effect on their ME properties.

In table 7.6 are values of electrical polarization observed on all six samples. In general the annealing led to reduction of electric polarization of material by about 20%.

Next we performed magnetocapacitance experiments on all samples, typical data obtained on annealed and non-annealed parts of one sample are shown in figure 7.14, it can be seen that after annealing the ME peaks are more pronounced and observable up to room-temperatures.

From the magnetocapacitance data we determined ME phase diagrams of all samples, which together with results of polarization experiments are shown in figure 7.15. In general one can see, that after annealing the ME region is broadened and that its boundary shifts to zero magnetic field as temperature increases above 150K. We were able to observe the ME peaks at 300K for all annealed samples.

In figure 7.14 it can also be seen, that apparent sample capacity increases by several order of magnitude as temperature is raised from 4.2 K to 300 K. We calculated relative permittivities of all samples from their capacitances determined at 1 MHz in 1 T field at various temperatures – results are plotted in figure 7.16. It can be seen that all annealed samples follow the same dependence, as well as the non-annealed ones. We fitted the temperature dependences for samples 5A and 5NA with empirical relation:

$$\varepsilon_r(T) = a\mathrm{e}^{-(T/T_0)^k} \tag{7.4}$$

In case of sample 5NA the last two points (273 K and 300 K) were omitted from the fit. Fit results are shown in table 7.7. The observed increase of apparent permittivity is likely to be caused by increase of conductivity – the annealing has clearly reduced conductivity of the samples.

	P (nC/cm^2)	
sample	inc.	dec.
1NA	13.3	12.4
1A	10.5	7.1
2NA	12.1	12.3
2A	10.5	10.4
5NA	16.7	17.2
5A	12.5	12.4

Table 7.6: Electrical polarization observed on samples from second batch at 4.2K after poling. The inc. and dec. column charge observed when magnetic field was increased or decreased from its starting value of 1T.

Sample	a	T_0 (K)	k
5A	27.8 ± 1.0	196.4 ± 2.2	2.71 ± 0.05
5NA	37 ± 4	115 ± 3	2.15 ± 0.06

Table 7.7: Parameters of empirical fits of temperature dependence of apparent sample permittivity.

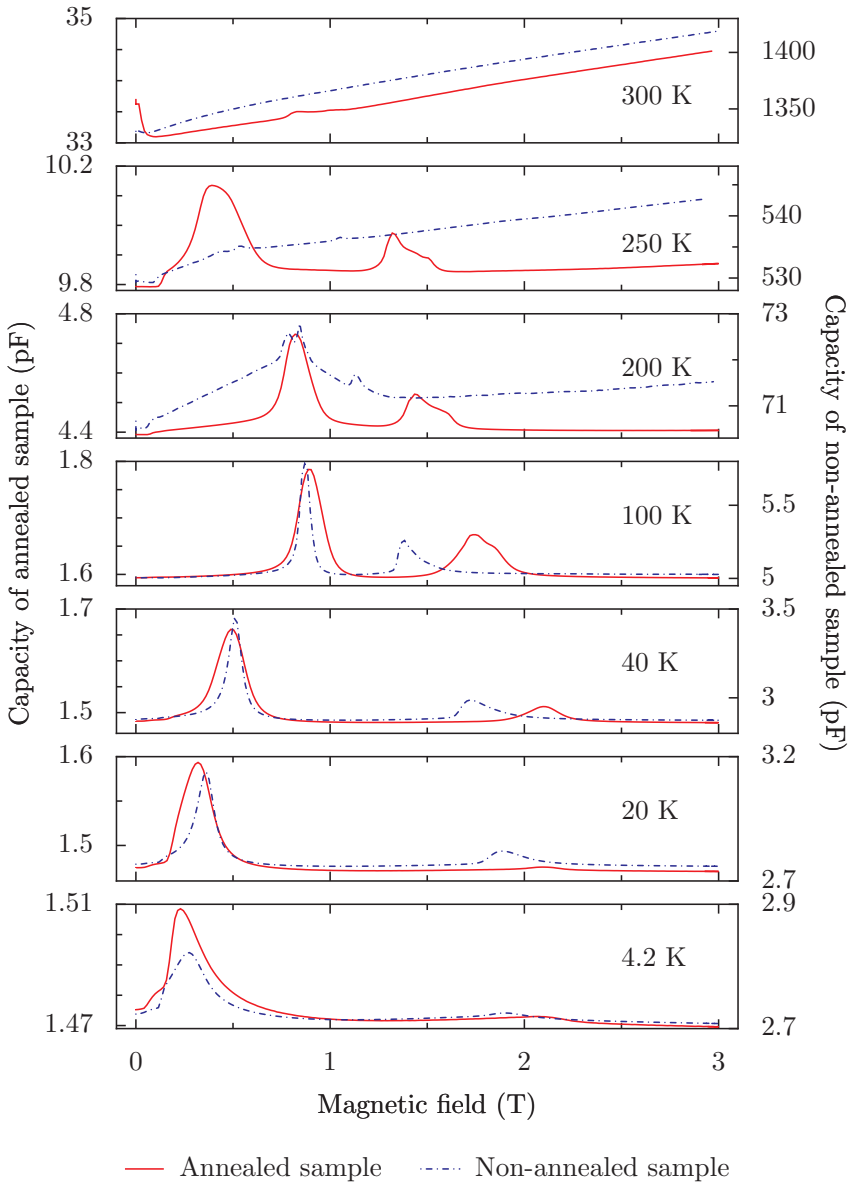

Figure 7.14: Magnetocapacitance results obtained on samples 5A and 5NA at various temperatures in range 4.2−300 K (bottom to top). Data were obtained on raising magnetic field. Capacities were measured at 1 MHz

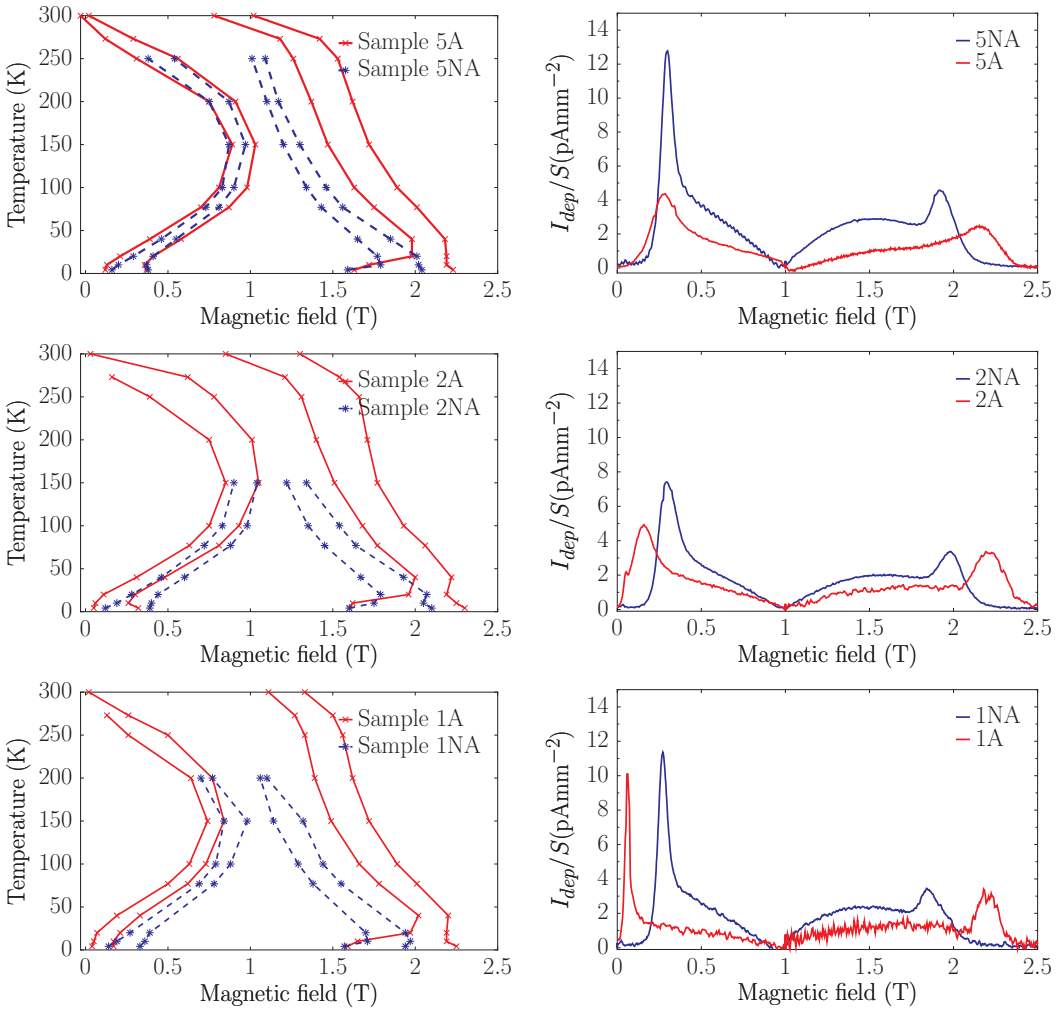

Figure 7.15: Comparison of annealed (A) and reference(NA) parts of samples from second batch. Blue lines correspond to as-grown samples, red to annealed ones. On the left, there are phase diagrams determined from magnetocapacitance results, on the right, there are electric polarization data obtained at 4.2 K.

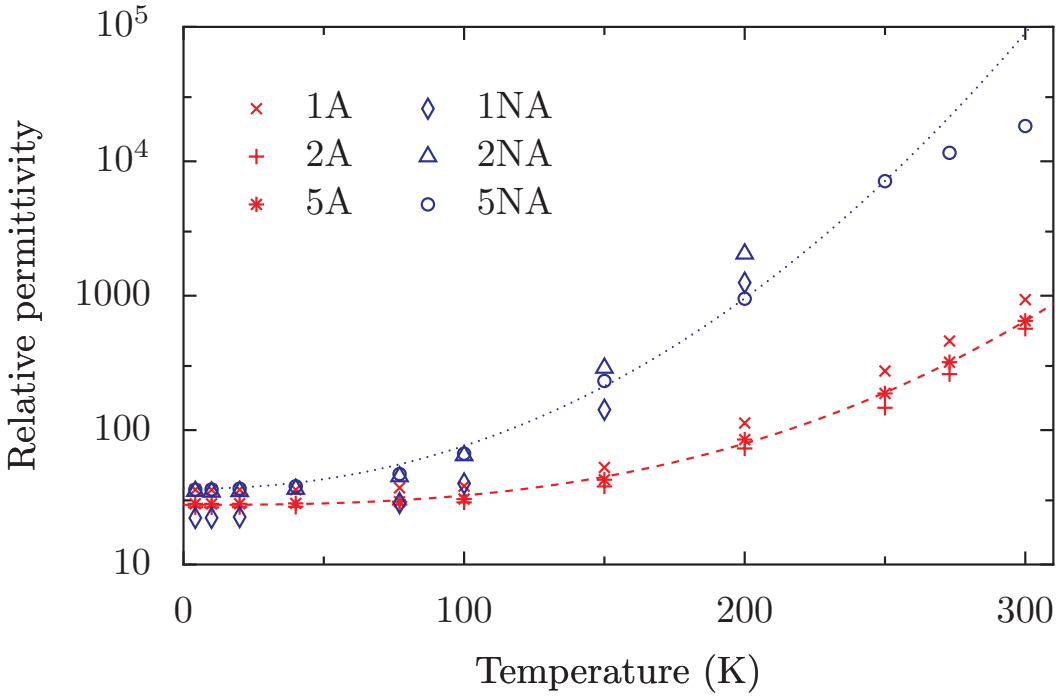

Figure 7.16: Temperature dependence of relative permittivities of all samples from second batch. The permittivities were measured at 1 MHz in 1 T magnetic field. Annealed samples are shown in red, non-annealed in blue. Lines correspond to fits of data on samples 5A and 5NA with empirical function 7.4, fit results are in table 7.7.

7.7 Summary

We were able to observe ^{57}Fe and ^{67}Zn NMR signals in samples of $Ba_{2-x}Sr_xZn_2Y$ hexaferrites and to partially interpret them. Upon annealing the spectra of magnetoelectric $Ba_{0.5}Sr_{1.5}Zn_2Y$ were not significantly altered thus indicating that there were only minor changes of Zn distribution.

In ME experiments on $Ba_{0.5}Sr_{1.5}Zn_2Y$ we observed electrical polarization dependent on magnetic field at 4.2K and constructed ME phase diagrams based on magnetocapacitance experiments. Annealing improved range of magnetic fields and temperatures in which magnetocapacitance was observable, most importantly in annealed samples we were able to observe the magnetocapacitance effect at room temperature. The annealing also lowers maximum electrical polarization of samples by about 20%.

The magnetoelectric phase perishes in high magnetic fields, however the high field phase retains information on polarization orientation in fields up to 8 T.

Chapter 8

Satellite patterns in NMR spectra of M ferrite

As we studied various substituted M type systems, in this chapter we will present theoretical considerations on effect of substitution on ^{57}Fe NMR in M ferrite.

8.1 Mechanisms of satellite formation

Substitution atoms alter local fields on nuclei in their vicinity, resonance of these nuclei appears at shifted frequencies – satellite lines are formed in NMR spectrum. The observed ^{57}Fe NMR shifts in magnetic oxides, are up to few MHz. There are three main mechanisms of the local field alteration: the substitution atom changes transfered hyperfine fields on nuclei of its neighbors, exchange interactions with its neighbors (which in the end alters on-site components of hyperfine fields of its neighbors) and generates different dipolar magnetic field on its neighbor sites. Apart from this one can consider second order effects – substitution alters properties of its neighbor and the altered neighbor acts on its neighbors.

In case of more than one substitution atoms in vicinity of resonant nucleus one can use the additivity hypothesis [67] which assumes that changes to local field on resonant nucleus due to substitution atoms at different positions are approximately additive. A sketch of NMR satellite pattern formed from originally single resonance line due to substitution entering sites in vicinity of the resonant site is shown in figure 8.1.

Effect of substitution on transfered hyperfine fields cannot be predicted with reasonable accuracy. The mechanisms in question are quite complex and use of electronic structure calculations is inevitable, however, the effect is of

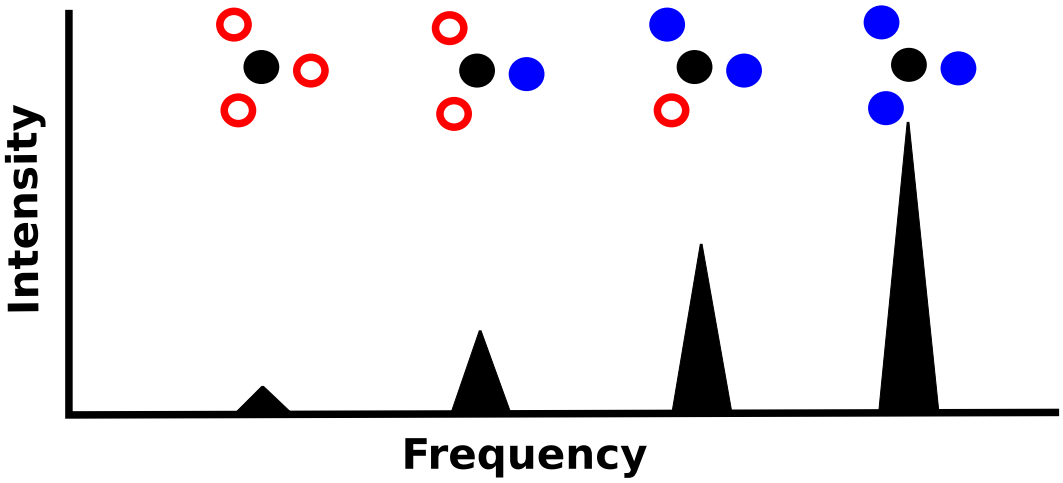

Figure 8.1: Sketch of NMR spectrum influenced by substitution. A resonant site (black circle) has three equivalent nearest neighbors which can be occupied by substitution atom (red ring) or original atom (blue circle). Four resonance lines (black triangles) corresponding to four possibilities (0–3 nearest neighbors being substituted) are observed. The lines are approximately equidistant as predicted by additivity hypothesis. Intensities of lines are proportional to number of realizations of corresponding variants of nn arrangement within studied sample.

size comparable to error of present electronic structure calculations even after the semi-empirical correction [52].

Alteration of exchange interactions gains importance as temperature is increased towards ordering temperature of studied material. Hyperfine component of local field on nucleus is proportional to mean magnetic moment of its ion, change of the moment can be observed as a shift of resonance frequency. In general alteration of exchange interactions results in different mean magnetic moment of the ion, however at low temperatures ($T \ll T_c$) the mean moments are nearly saturated and are not expected to be much sensitive to variation of exchange field.

The dipole contribution (change of $\boldsymbol{B}_{\text{latt}}$ due to substitution) is the only one, which is straightforward to quantify. It can be estimated by placing an effective magnetic moment on position of the substituted ion and calculating magnetic field generated by the dipole. We will consider only collinear magnetic order with moments parallel with hexagonal axis. Magnitude and orientation of the moment should be such that the added moment combined with moment of original ion yields magnetic moment of the substitution. The

resulting resonance frequency of ^{57}Fe is given only by magnitude of local field. The dipole fields are in order of tenths of Tesla, hence one can estimate the frequency shift as proportional to component of dipole field parallel with total magnetization:

$$\Delta f = \pm \frac{\gamma_{\mathrm{Fe}}}{2\pi} \frac{\mu_0 m}{4\pi r^3} \left(3\cos^2\theta - 1\right) \tag{8.1}$$

where μ_0 is permeability of vacuum, m effective magnetic moment of substitution, r distance from substitution to resonant nucleus and θ angle between vector connecting the substitution with resonant nucleus and direction of magnetization. In case of nonmagnetic substitution for ferric cation the magnetic moment is $5\mu_{\mathrm{B}}$ oriented antiparallel with moment of substituted ion. Sign of the shift depends on mutual orientation of effective magnetic moment of substitution and of local magnetic field on resonant nucleus (which is antiparallel with magnetic moment of the ferric ion the nucleus is in), the positive sign corresponds to effective magnetic moment being parallel with the local magnetic field.

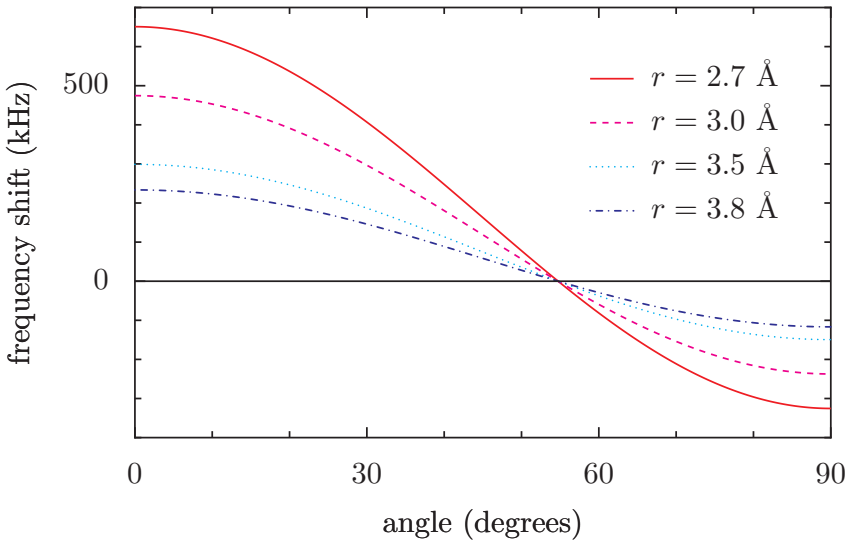

Figure 8.2: Angular dependence of dipole contribution to ^{57}Fe NMR frequency shifts induced by substitution atom with effective moment $5\mu_{\mathrm{B}}$ (nonmagnetic substitution for ferric ion) oriented parallel with effective field on resonant nucleus (equation 8.1). The dependence is plotted for four typical distances between ferric nearest neighbors in M–type hexaferrite.

8.2 Calculation of satellite pattern intensities

While in general it is not possible to predict positions (shifts) of satellite lines, mainly due to unknown contribution of transfered hyperfine fields, relative intensities of satellite lines can be estimated with much greater confidence. Intensity of a satellite is proportional to number of positions in sample with the corresponding defect pattern in their vicinity. It is then possible to calculate relative intensities of satellites for a given model of distribution of substitution atoms within the sample. As content of substitution increases, not only the intensity of satellites increases, but simultaneously intensity of the main line drops as total intensity of resonance coming from the affected sublattice is constant (or lowers when the substitution enters the affected sublattice). Of course, positions of main line and satellite lines do vary with substitution content as overall character of material changes, and the widths tend to increase (due to combined effect of substitution atoms further away of resonant nucleus on local field).

In following we will calculate expected relative intensities of satellite lines induced by substitution with content x in M–type ferrite: $A_{1-x}B_{1-x}Fe_{12}O_{19}$ (substitution on large cation site) or $AFe_{12-x}M_xO_{19}$ (substitution on small cation site). In case of small cation substitution we will assume, that the substitution has a strong preference to one of five small cation sites. We will limit the analysis to nearest neighbor (nn) effects only (distance between substituted and resonant site below 4 Å). We will also assume that distribution of substitution is "random", i.e. probability of occupation of a site within selected sublattice by substitution is independent of occupation state of remaining sites. The procedure is following:

1. The substitution enters site sS where s is multiplicity and S type of the site (e.g. for $12k$, $s = 12$, $S = k$). The satellites will be observed on resonances of nearest neighbors of the site sS: the n_iN_i sites (n_i is multiplicity and N_i type of the site), there are several types of nn sites (hence the index i), each of them is to be analyzed separately.

2. For a particular nN site (particular i), find the t nearest neighbors of sS type. These nns will generate at least t satellite lines depending on number of sites occupied by substitution atoms (not all of them are necessarily found in experiment, typically due to low intensity or overlap with another lines).

3. Relative intensities of lines are given by probabilities of finding $q \in \{0, 1, .., t\}$ substitution atoms in vicinity of resonant nucleus. To

estimate the probabilities $p(q)$ we use binomial distribution:

$$p(q) = \binom{t}{q} \left(\frac{2x}{s}\right)^q \left(1 - \frac{2x}{s}\right)^{t-q} \tag{8.2}$$

where x is content of substitution, $p(0)$ corresponds to intensity of the main line (I_0) and $p(1, 2, \ldots t)$ to intensities of satellites ($I_{1,2,\ldots t}$).

4. For each $0 < q < t$ there may be several groups of magnetically inequivalent patterns of q substitution atoms distributed amongst the t sites of S type. Each of the patterns generates its own satellite line and the $p(q)$ corresponds sum of their intensities. Relative intensities of these satellite lines are proportional to numbers of possible realizations of each pattern. In considerations of magnetic equivalency we will assume that magnetic moments are parallel with hexagonal axis.

We use normalization of ^{57}Fe NMR intensity in which the whole spectrum has intensity equal to number of ferric ions in formula unit, i.e. in pure M compound with trivalent large cation the total intensity of ^{57}Fe NMR spectrum is 12 and intensities of subspectra of individual sublattices are:

$$I_{\text{tot}}^{nN} = \frac{n}{2} \tag{8.3}$$

If substitution enters the resonant sublattice, the total intensity needs to be reduced to:

$$I_{\text{tot}}^{nN} = \frac{n}{2} - x \tag{8.4}$$

as resonant ^{57}Fe nuclei in the sublattice are diluted by the substitution atoms.

For intensities of resonance lines we get:

$$I_q^{nN} = I_{\text{tot}}^{nN} p(q) \tag{8.5}$$

In doubly substituted samples, the situation is more complex. If substitution contents are small (hence most NMR intensity stays in main lines) the resulting pattern can be estimated as average of patterns expected for individual substitutions (since cases when resonant nuclei have two different substitution atoms in vicinity are not very frequent). As the content increases, new satellites emerge, these are generated by nuclei with both kinds of substitution atoms in their vicinity. In such case it is practical to first calculate expected pattern generated by substitution which has stronger effect on particular resonant sublattice (it draws more intensity from the main lines) and then consider each of found lines as a main line to be split into satellite sub-pattern by the second substitution (this is analogous to point 4 of the above procedure where

intensity is divided between several inequivalent configurations of substitution atoms).

When substitution has no strong preference towards one sublattice but to two or more, it is analogous to simultaneous substitution with two (or more) virtual species with strong preferences towards the sublattices that the actual substitution enters. One can proceed in similar manner as in case of doubly substituted material, the main difference is, that contents of the virtual substitutions are not known – one knows only the sum (content of the real substitution) and its distribution amongst the virtual substituions is parameter of model and can only be found by comparison with experiment.

In next two sections we will calculate expected schemes and intensities of satellite patterns for substitution contents relevant for systems discussed in following chapters.

8.3 Substitution on large cation site

The $2d$ large cation site has three types of nearest neighbor small cation sites: three $2b$ sites, six $4f_{\mathrm{VI}}$ sites and six $12k$ sites. Satellites on ^{57}Fe NMR lines can be expected when there is substitution on large cation site, i.e. in M type structure with formula $\mathrm{A}_{1-x}\mathrm{B}_x\mathrm{Fe}_{12}\mathrm{O}_{19}$ where A and B are large atoms (e.g. Sr and Pb) and x is content of substitution B.

A $12k$ site has only one nearest neighbor $2d$ site, hence one satellite line with intensity $I_1 = 6x$ can be expected and intensity of main $12k$ line should drop with increasing content of substitution as: $I_0 = 6 - 6x$.

A $2b$ site has three equivalent nn 2d sites, hence up to three satellites corresponding to 1–3 substitution atoms in vicinity of resonant nucleus can be formed, their intensities are in table 8.1.

A $4f_{\mathrm{VI}}$ site has also three nn $2d$ sites, hence situation is analogous to that of $2b$ resonance, only difference is that multiplicity of the $4f_{\mathrm{VI}}$ sublattice is double of that of $2b$, hence table 8.1 can be used, only the intensities listed there need to be doubled.

$2b$ resonance				
y	substituted $2d$ nn			
	0	1	2	3
0.21	0.49	0.39	0.10	0.01
0.25	0.42	0.42	0.14	0.02
0.50	0.13	0.38	0.38	0.13
0.75	0.02	0.14	0.42	0.42

Table 8.1: Intensities of $2b$ lines in case of substitution entering the $2d$ sublattice for various contents of substitution x. Total intensity of $2b$ resonance is set to 1. The table can also be used for satellite pattern generated on $4f_{\mathrm{VI}}$ resonance, only the intensities should be doubled.

8.4 Substitution on small cation sites

In this section we deal with satellite patterns in system with general formula: $\mathrm{AFe}_{12-x}\mathrm{M}_x\mathrm{O}_{12}$, where A is large cation, M is substitution atom and x is content of substitution. We will deal with five cases of substitution having strong preference towards entering one of five small cation sites in M structure.

To find which sublattices are to be affected by substitution entering selected sublattice we constructed lists of nearst neighbors within small cation sites – resonance lines of sites adjacent to substituted ones are expected to form satellite patterns. The lists are in table 8.2.

site	nearest neighbors						
$2a$	6 $12k$ 3.059Å	6 $4f_{\mathrm{IV}}$ 3.455Å					
$2b$	6 $4f_{\mathrm{VI}}$ 3.657Å	6 $12k$ 3.660Å					
$4f_{\mathrm{IV}}$	3 $2a$ 3.455Å	6 $12k$ 3.504Å	3 $12k$ 3.576Å	3 $4f_{\mathrm{IV}}$ 3.622Å	1 $4f_{\mathrm{VI}}$ 3.783Å		
$4f_{\mathrm{VI}}$	1 $4f_{\mathrm{VI}}$ 2.705Å	6 $12k$ 3.491Å	3 $2b$ 3.657Å	1 $4f_{\mathrm{IV}}$ 3.783Å			
$12k$	2 $12k$ 2.907Å	2 $12k$ 2.977Å	1 $2a$ 3.059Å	2 $4f_{\mathrm{VI}}$ 3.491Å	2 $4f_{\mathrm{IV}}$ 3.504Å	1 $4f_{\mathrm{IV}}$ 3.576Å	1 $2b$ 3.660Å

Table 8.2: Lists of nearest neighbors within set of small cation sites in SrM. First row of each entry gives number of, second row type of, and third row distance to equivalent nearest neighbor sites.

8.4.1 Substitution in $2a$

A $2a$ site has six $12k$ nearest neighbors and six $4f_{\mathrm{IV}}$ nn, hence if substitution atom enters the $2a$ sublattice, its effect should be observable on satellite patterns of $12k$ and $4f_{\mathrm{IV}}$ lines.

A $12k$ site has only one $2a$ type nn – we can expect one satellite line with intensity $I_1 = \frac{n_{12k}}{2} p(1) = 6x$ and main $12k$ line with intensity $I_0 = 6(1-x)$.

A $4f_{\mathrm{IV}}$ site has three equivalent $2a$ nn, hence three satellite lines corresponding to 1, 2 and 3 substitution atoms in vicinity of a $4f_{\mathrm{IV}}$ site can be expected. Intensities of the lines are in table 8.3.

$4f_{\mathrm{IV}}$ resonance

x	substituted $2a$ nn			
	0	1	2	3
0.06	1.66	0.32	0.02	–
0.20	1.02	0.77	0.19	0.02
0.21	0.99	0.79	0.21	0.02
0.25	0.84	0.84	0.28	0.03
0.30	0.69	0.88	0.38	0.05
0.35	0.55	0.89	0.48	0.09
0.40	0.43	0.86	0.58	0.13
0.50	0.25	0.75	0.75	0.25
0.75	0.03	0.28	0.84	0.84
1.00	–	–	–	2.00

Table 8.3: Intensities of $4f_{\mathrm{IV}}$ lines in case of substitution entering the $2a$ sublattice for various contents of substitution x. Total intensity of $4f_{\mathrm{IV}}$ resonance is set to 2. The table is also valid for satellite pattern generated on $4f_{\mathrm{VI}}$ resonance by substitution entering $2b$ sublattice.

8.4.2 Substitution in $2b$

If substitution enters the $2b$ sublattice, situation is analogous to that of substitution entering the $2a$. Satellites are expectable on $12k$ and $4f_{\mathrm{VI}}$ lines, numbers of nearest neighbors are the same as in $2a$ case. We can again expect one satellite on $12k$ resonance and up to three on $4f_{\mathrm{VI}}$ line, intensities are given by the same formulae (in case of $4f_{\mathrm{VI}}$ resonance the table 8.3 can be used).

8.4.3 Substitution in $4f_{\mathrm{IV}}$

Nearest neighbors of a $4f_{\mathrm{IV}}$ site are three $2a$ sites, nine $12k$ sites, three $4f_{\mathrm{IV}}$ sites and one $4f_{\mathrm{VI}}$ site. The $12k$ type nn consist of two groups of equivalent sites of three and six members.

A $2a$ site has six equivalent nn of $4f_{\mathrm{IV}}$ type, expected intensities of $2a$ resonances are in table 8.4

A $12k$ site has three nn of $4f_{\mathrm{IV}}$ type, one is approximately above or bellow (the "up" direction being parallel with hexagonal axis) the site, the other two are rather sideways from the site, i.e. there are two magnetically inequivalent types of $4f_{\mathrm{IV}}$ neighbors.

Intensities of resonance lines corresponding to 0–3 substitution atoms entering the three $4f_{\mathrm{IV}}$ adjacent to a $12k$ site are given in table 8.5. As the $4f_{\mathrm{IV}}$ sites are not equivalent (with respect to particular $12k$ site), the satellite lines

$2a$ resonance

x	substituted $4f_{\mathrm{IV}}$ nn						
	0	1	2	3	4	5	6
0.06	0.83	0.15	0.01	–	–	–	–
0.20	0.53	0.35	0.10	0.01	–	–	–
0.21	0.51	0.36	0.11	0.02	–	–	–
0.25	0.45	0.38	0.14	0.03	–	–	–
0.30	0.38	0.40	0.18	0.04	0.01	–	–
0.35	0.32	0.40	0.21	0.06	0.01	–	–
0.40	0.26	0.39	0.25	0.08	0.02	–	–
0.50	0.18	0.36	0.30	0.13	0.03	–	–
0.75	0.06	0.21	0.32	0.26	0.12	0.03	–
1.00	0.02	0.09	0.23	0.31	0.23	0.09	0.02

Table 8.4: Intensities of $2a$ resonance in case of substitution entering $4f_{\mathrm{IV}}$ sublattice calculated for various contents of substitution x. Total intensity of $2a$ resonance is normalized to 1, only intensities greater than 0.005 are shown. This table is also valid for influence of substitution on $4f_{\mathrm{VI}}$ site influencing $2b$ resonance in scenario when there is no correlation in occupation of $4f_{\mathrm{VI}}$ sites.

$12k$ resonance

x	substituted $4f_{\mathrm{IV}}$ nn			
	0	1	2	3
0.06	5.48	0.51	0.02	–
0.20	4.37	1.46	0.16	0.01
0.21	4.30	1.51	0.18	0.01
0.25	4.02	1.73	0.25	0.01
0.30	3.68	1.95	0.34	0.02
0.35	3.37	2.14	0.45	0.03
0.40	3.07	2.30	0.58	0.05
0.50	2.53	2.53	0.84	0.09
0.75	1.46	2.64	1.58	0.32
1.00	0.75	2.25	2.25	0.75

Table 8.5: Intensities of $12k$ lines in case of substitution entering the $4f_{\mathrm{IV}}$ sublattice for various contents of substitution x. Total intensity of $12k$ resonance is normalized to 6. In cases of one and two substitution atoms in vicinity of resonant nucleus the intensity of satellite is divided in ratio 1:2 between satellite lines corresponding to inequivalent distribution of substitution atoms amongst the three $4f_{\mathrm{IV}}$ sites in vicinity of resonant $12k$ site.

corresponding to one and two substitution atoms next to a $12k$ site can be split in ratio 2 : 1, in case of 1 substitution atom the weaker line corresponds to substitution in site "above" the resonant $12k$, and the stronger to substitution in one of $4f_{\mathrm{IV}}$ the remaining two sites. In case of two substitution atoms, the stronger line corresponds to the site above being one of the ones occupied by substitution and the weaker to it being being occupied by iron.

Next one can observe effect of substitution entering $4f_{\mathrm{IV}}$ sublattice on $4f_{\mathrm{IV}}$ resonance itself as any $4f_{\mathrm{IV}}$ site has three equivalent nn of the same type. Apart from emergence of satellite lines, intensity of whole $4f_{\mathrm{IV}}$ resonance pattern should be lowered by substitution atoms (equation 8.4). Expected intensities of $4f_{\mathrm{IV}}$ resonance lines are in table 8.6

Finally the $4f_{\mathrm{VI}}$ resonance should be influenced, each $4f_{\mathrm{VI}}$ site has one $4f_{\mathrm{IV}}$ nn – one satellite line with intensity $I_1 = x$ can be expected, intensity of main $4f_{\mathrm{VI}}$ line should be lowered to $I_0 = 2 - x$.

$4f_{\mathrm{IV}}$ resonance				
x	substituted $4f_{\mathrm{IV}}$ nn			
	0	1	2	3
0.06	1.77	0.16	0.01	–
0.20	1.31	0.44	0.05	–
0.21	1.28	0.45	0.05	–
0.25	1.17	0.50	0.07	–
0.30	1.04	0.55	0.10	0.01
0.35	0.93	0.59	0.13	0.01
0.40	0.82	0.61	0.15	0.01
0.50	0.63	0.63	0.21	0.02
0.75	0.31	0.55	0.33	0.07
1.00	0.13	0.38	0.38	0.13

Table 8.6: Intensities of $4f_{\mathrm{IV}}$ lines in case of substitution entering the $4f_{\mathrm{IV}}$ sublattice for various contents of substitution x. Total intensity of $4f_{\mathrm{IV}}$ resonance is normalized to $2 - x$.

8.4.4 Substitution in $4f_{\mathrm{VI}}$

Nearest neighbors of a $4f_{\mathrm{VI}}$ site are one $4f_{\mathrm{VI}}$ site, six equivalent $12k$ sites, three equivalent $2b$ sites and one $4f_{\mathrm{IV}}$ site. The $4f_{\mathrm{VI}}$ sites come in pairs where the sites are only about 2.7Å apart, it is then worth considering also possibilities that substitution has strong preference toward occupying only one site of a pair or contrary that there is a strong preference towards occupation of both sites simultaneously.

Effect of substitution entering $4f_{\mathrm{VI}}$ sublattice on $4f_{\mathrm{VI}}$ resonance should be reduction of total $4f_{\mathrm{VI}}$ intensity to $I_{\mathrm{tot}} = 2 - x$ and formation of satellite line corresponding to the nearest neighbor $4f_{\mathrm{VI}}$ site occupied by substitution atom. In case of random distribution of substitution over $4f_{\mathrm{VI}}$ sublattice should intensity of the satellite be $I_1 = x - x^2/2$ and intensity of the main line $I_0 = 2 - 2x + x^2/2$. Terms $x^2/2$ correspond to occurrence of two adjacent $4f_{\mathrm{VI}}$ sites occupied by substitution atom simultaneously. If we assume strong tendency towards occupation of only one site in a pair, the $x^2/2$ terms should be omitted. If on the other hand there is a strong preference to occupying both sites in a $4f_{\mathrm{VI}}$ pair simultaneously, the satellite is not formed and only effect of substitution is reduction of $4f_{\mathrm{VI}}$ main line intensity to $I_{\mathrm{tot}} = 2 - x$.

A $12k$ site has two nearest neighbors of $4f_{\mathrm{VI}}$ type, a preference or disfavor towards occupation of both adjacent $4f_{\mathrm{VI}}$ sites should have no significant effect on intensities of satellites structure induced on $12k$ resonance. Expected intensities of $12k$ lines are in table 8.7

A $2b$ site has six nearest neighbors of $4f_{\mathrm{VI}}$ type, which can be broken up into three equivalent pairs. In case that substitution avoids entering both sites of a pair simultaneously, we can assume that there are three equivalent sites for substitution to enter in vicinity of any $2b$ site, multiplicity of these sites is then 2. The expected intensities of $2b$ resonances are in table 8.8. If substitution strongly prefers to enter both adjacent $4f_{\mathrm{VI}}$ sites simultaneously its content is effectively reduced to half of its value, $2b$ resonance intensities for this case are in table 8.9. If the substitution has neither preference nor disfavor towards entering both sites simultaneously (i.e. it occupies all six sites with the same probability regardless of state of next $4f_{\mathrm{VI}}$ in the pair), the situation is analogous to that of influence of substitution on $4f_{\mathrm{IV}}$ site affecting $2a$ resonance and table 8.4 should be used.

Finally the $4f_{\mathrm{IV}}$ resonance should be influenced, each $4f_{\mathrm{IV}}$ site has one $4f_{\mathrm{VI}}$ nearest neighbor – one satellite line with intensity $I_1 = x$ can be expected, intensity of main $4f_{\mathrm{IV}}$ line should be lowered to $I_0 = 2 - x$.

$12k$ resonance

x	substituted $4f_{\mathrm{VI}}$ nn		
	0	1	2
0.06	5.65	0.35	0.01
0.20	4.86	1.08	0.06
0.21	4.81	1.23	0.07
0.25	4.59	1.31	0.09
0.30	4.34	1.53	0.14
0.35	4.08	1.73	0.18
0.40	3.84	1.92	0.24
0.50	3.38	2.25	0.38
0.75	2.34	2.81	0.84
1.00	1.50	3.00	1.50

Table 8.7: Intensities of $12k$ lines in case of substitution entering the $4f_{\mathrm{VI}}$ sublattice for various contents of substitution x. Total intensity of $12k$ resonance is set to 6.

$2b$ resonance

x	substituted $4f_{\mathrm{VI}}$ nn			
	0	1	2	3
0.06	0.83	0.16	0.01	–
0.20	0.51	0.38	0.10	0.01
0.21	0.49	0.39	0.10	0.01
0.25	0.42	0.42	0.14	0.02
0.30	0.34	0.44	0.19	0.03
0.35	0.27	0.44	0.24	0.04
0.40	0.22	0.43	0.29	0.06
0.50	0.13	0.38	0.38	0.13
0.75	0.02	0.14	0.42	0.42
1.00	–	–	–	1.00

Table 8.8: Intensities of $2b$ lines in case of substitution entering the $4f_{\mathrm{VI}}$ sublattice for various contents of substitution x assuming that substitution does not enter both sites in any f_{VI} pair simultaneously. Total intensity of $2b$ resonance is set to 1.

$2b$ resonance

x	substituted $4f_{\mathrm{VI}}$ nn			
	0	2	4	6
0.06	0.91	0.08	–	–
0.20	0.73	0.24	0.03	–
0.21	0.72	0.25	0.03	–
0.25	0.67	0.29	0.04	–
0.30	0.61	0.33	0.06	–
0.35	0.56	0.36	0.08	0.01
0.40	0.51	0.38	0.10	0.01
0.50	0.42	0.42	0.14	0.02
0.75	0.24	0.44	0.26	0.05
1.00	0.13	0.38	0.38	0.13

Table 8.9: Intensities of $2b$ lines in case of substitution entering the $4f_{\mathrm{VI}}$ sublattice for various contents of substitution x assuming that substitution does preferentially enter both sites in a f_{VI} pair simultaneously. Total intensity of $2b$ resonance is set to 1.

8.4.5 Substitution in $12k$

A $12k$ site has four nearly equivalent nn of $12k$ type (this are two pairs of equivalent sites), one $2a$ nn, two equivalent $4f_{\mathrm{VI}}$ nn, three $4f_{\mathrm{IV}}$ nn, two of which are equivalent and finally one $2b$ nn.

Intensities of satellite pattern on $12k$ resonance induced by substitution entering $12k$ sublattice are in table 8.10, the intensities were calculated under assumption that all four $12k$ nn of a $12k$ site are equivalent.

Influence of substitution entering $12k$ sublattice on resonances of $2a$ and $2b$ sublattices is the same (in terms of satellite pattern intensities, positions of resonances do of course differ) as any site of this type has six equivalent $12k$ nearest neighbors. Intensities of satellite patterns are in table 8.11.

Effect on $4f_{\mathrm{VI}}$ resonance is very similar to that on $2a$ and $2b$, again the $4f_{\mathrm{VI}}$ has six equivalent $12k$ nn, the only difference is, that multiplicity of resonance site is now four, hence intensities of satellite patterns are doubled, the calculated intensities are listed in table 8.12.

Last remaining is the resonance of $4f_{\mathrm{IV}}$ sites. A $4f_{\mathrm{IV}}$ site has six equivalent $12k$ neighbors approximately in directions within hexagonal plane and another three approximately in direction of hexagonal axis – this two groups cannot be considered as nearly equivalent. Despite this, we calculated intensities of satellite patterns as if all nine $12k$ sites in vicinity of resonant $4f_{\mathrm{IV}}$ site were equivalent, the results are in table 8.13.

$12k$ resonance

x	substituted $12k$ nn				
	0	1	2	3	4
0.06	5.71	0.23	–	–	–
0.20	5.06	0.70	0.04	–	–
0.21	5.02	0.73	0.04	–	–
0.25	4.85	0.84	0.06	–	–
0.30	4.64	0.98	0.08	–	–
0.35	4.44	1.11	0.10	–	–
0.40	4.25	1.21	0.13	0.01	–
0.50	3.88	1.41	0.19	0.01	–
0.75	3.08	1.76	0.38	0.04	–
1.00	2.41	1.93	0.58	0.08	–

Table 8.10: Intensities of $12k$ lines in case of substitution entering $12k$ sublattice calculated for various contents of substitution x. Total intensity of $12k$ resonance is set to $6 - x$.

$2a$ or $2b$ resonance

x	substituted $12k$ nn						
	0	1	2	3	4	5	6
0.06	0.94	0.06	–	–	–	–	–
0.20	0.82	0.17	0.01	–	–	–	–
0.21	0.81	0.18	0.02	–	–	–	–
0.25	0.77	0.20	0.02	–	–	–	–
0.30	0.74	0.23	0.03	–	–	–	–
0.35	0.70	0.26	0.04	–	–	–	–
0.40	0.66	0.28	0.05	–	–	–	–
0.50	0.59	0.32	0.07	0.01	–	–	–
0.75	0.45	0.38	0.14	0.03	–	–	–
1.00	0.33	0.40	0.20	0.05	0.01	–	–

Table 8.11: Intensities of $2a$ or $2b$ lines in case of substitution entering $12k$ sublattice calculated for various contents of substitution x. Total intensity of $2a$ or $2b$ resonance is set to 1.

$4f_{\mathrm{VI}}$ resonance

x	substituted $12k$ nn						
	0	1	2	3	4	5	6
0.06	1.88	0.11	–	–	–	–	–
0.20	1.63	0.34	0.03	–	–	–	–
0.21	1.62	0.35	0.03	–	–	–	–
0.25	1.55	0.40	0.04	–	–	–	–
0.30	1.47	0.46	0.06	–	–	–	–
0.35	1.39	0.52	0.08	0.01	–	–	–
0.40	1.32	0.57	0.10	0.01	–	–	–
0.50	1.19	0.65	0.15	0.02	–	–	–
0.75	0.90	0.77	0.27	0.05	0.01	–	–
1.00	0.67	0.80	0.40	0.11	0.02	–	–

Table 8.12: Intensities of $4f_{\mathrm{VI}}$ lines in case of substitution entering $12k$ sublattice calculated for various contents of substitution x. Total intensity of $4f_{\mathrm{VI}}$ resonance is set to 2.

As one can see, substantial intensities are expected only for 0–3 nn $12k$ sites being occupied by substitution atom. If none of the nn sites is occupied we get single (main) line. If one is occupied there is 2/3 probability that the substitution is in one of six equivalent sites and 1/3 probability, that it is in one of three remaining equivalent sites, hence the intensity corresponding to 1 nn substitution atom is split in ratio 1:2 between satellites corresponding to this two configurations. If two of the nine $12k$ sites are occupied, we can analogously expect three satellites with intensities 5:3:1 corresponding to both one and none substitution atoms entering the six member group of equivalent nn $12k$ sites. Finally, if three substitution atoms are in the nn sites, four satellites with ratio of intensities 20:15:6:1 can be expected, and again intensity of satellite increases with number of substitution atoms in the six member group.

$4f_{\mathrm{IV}}$ resonance

x	substituted $12k$ nn									
	0	1	2	3	4	5	6	7	8	9
0.06	1.83	0.17	0.01	–	–	–	–	–	–	–
0.20	1.47	0.46	0.06	0.01	–	–	–	–	–	–
0.21	1.45	0.47	0.07	0.01	–	–	–	–	–	–
0.25	1.36	0.53	0.09	0.01	–	–	–	–	–	–
0.30	1.26	0.60	0.13	0.02	–	–	–	–	–	–
0.35	1.16	0.65	0.16	0.02	–	–	–	–	–	–
0.40	1.07	0.69	0.20	0.03	–	–	–	–	–	–
0.50	0.91	0.75	0.27	0.06	0.01	–	–	–	–	–
0.75	0.60	0.77	0.44	0.15	0.03	–	–	–	–	–
1.00	0.39	0.70	0.56	0.26	0.08	0.02	–	–	–	–

Table 8.13: Intensities of $4f_{\mathrm{IV}}$ lines in case of substitution entering $12k$ sublattice calculated for various contents of substitution x. Total intensity of $4f_{\mathrm{VI}}$ resonance is set to 2.

8.5 Summary

We discussed impact of cation substitution in M type hexaferrite on its ^{57}Fe NMR spectra, namely on number and relative intensities of expected satellite lines. These results will be used in following chapters for analysis of experimental ^{57}Fe NMR spectra.

Chapter 9

Sc doped BaM spheres

9.1 Introduction

We measured spectra and relaxation times of ^{57}Fe NMR at 4.2K in zero external magnetic field in small Sc doped BaM hexaferrite ($BaFe_{12-x}Sc_xO_{19}$) spheres fabricated out of crystals much larger than the spheres. Primal reason for this study was observed dependence of FMR linewidth of the spheres on position of the sphere material within the original crystal (for sample notation and FMR linewidths see table 9.2). If the FMR linewidth dependence was due to changing concentration of Sc or a contaminant (if present) throughout the original crystal, there should be corresponding variation of spectra and relaxation times T_1 as well.

9.2 Samples

Two kinds of Sc substituted BaM sample series were studied: T–V14 and V24.

The T–V14 ($x_{Sc} = 0.2$) crystals were grown on a [2 $\bar{1}$ $\bar{1}$ 0] oriented Ba–hexaferrite seed by a TSSG growth technique using the slow-cooling method. The V24 crystals ($x_{Sc} = 0.3$) were grown by spontaneous nucleation of hexaferrite crystals at the crucible bottom by the slow-cooling method.

The crystal T–V14 was cut parallel to the hexagonal (0 0 0 1) plane. From the centre (seed region) to the crystal boundaries (facets) nine slices have been cut. Slice no. 9 was the outermost slice (facet) and slice no. 2 the innermost slice (seed). The slices were approximately 0.75 mm thick and the thickness of the cutting blade was 0.5 mm. Spheres with diameter 330 μm were cut were cut from the layers.

In case of spheres fabricated out of V24 crystal, the original position of sphere within parent crystal was not specified, however the two spheres differed

significantly in FMR linewidths.

In addition to samples prepared in form of spheres we studied T–V13 ($x_{\mathrm{Sc}} = 0.06$) crystal grown TSSG technique using the slow-cooling method. This crystal was used to obtain spectra of material with lower x_{Sc} than that of T–V14 and V24 samples, relaxations were not studied on this sample.

The samples were prepared by C. Dubs from Innovent e.V. Jena.

9.3 Experimental

Spheres were oriented with easy axis approximately perpendicular to direction of rf field, this configuration should yield strongest signal from magnetic domains.

Longitudinal relaxation T_1 was measured by modified inversion recovery pulse sequence (figure 5.2). The observed echo was Fourier-transformed and amplitude of the transform at excitation frequency was evaluated.

The relaxation delay was swept from tens of μs to about half a second, time from the $\pi/2$ pulse to echo was 40 μs. The repetition times used for inversion recovery experiments are in tab 9.1. Typically about 1000 scans were sufficient to obtain good S/N for lines $12k$, $4f_{\mathrm{IV}}$, $2a$ and $4f_{\mathrm{VI}}$, in case of $2b$ line tens of thousands had to be used – to achieve this in reasonable time number of different relaxation delays had to be severely reduced (from typical 30 to about 10).

The transversal relaxation time T_2 was measured by the CPMG pulse sequence (figure 5.1). For evaluation of the T_2 relaxation we used time domain data (i. e. the signal was not Fourier transformed), namely amplitude of spin echo (its maximum) as a function of time from the beginning of pulse sequence. Typical separation of π pulses was about 200 μs.

9.4 Results

9.4.1 Relaxations

The observed relaxation decays (both T_1 and T_2) could not be well described by single-exponential decay, to deal with this we employed a stretched exponential function [68]:

$$A = A_0 \mathrm{e}^{-(t/\tau_0)^{\beta}},\ 0 < \beta \leq 1 \tag{9.1}$$

The τ parameter stands for relaxation time T_1 or T_2. In this decay there is an underlying distribution $f(\tau)$ of relaxation times τ to which correspond single-exponential decays $a \sim \mathrm{e}^{-t/\tau}$. Mean relaxation time is defined as first

moment of relaxation time distribution. While the $f(\tau)$ corresponding to decay described by equation 9.1 is quite complex, the mean relaxation time can be expressed as:

$$\langle\tau\rangle = \tau_0\Gamma\left(1+\frac{1}{\beta}\right) \tag{9.2}$$

where $\Gamma(x)$ is the gamma-function.

The inversion recovery data were fitted with relation:

$$I(t) = |A - 2B\,\mathrm{e}^{-(t/T_1)^{\beta_1}}| + b;\ b > 0 \tag{9.3}$$

the B constant was kept independent of A in order to correct for imperfections in experiment settings, typically pulse lengths and amplitudes (in ideal case there should be $A = B$ and in general $A > B$). The CPMG decay data were fitted with:

$$I(t) = A\mathrm{e}^{-(t/T_2)^{\beta_2}} + b;\ b > 0 \tag{9.4}$$

The mean values of relaxation times were calculated using equation 9.2, namely:

$$\langle T_{1,2}\rangle = T_{1,2}\Gamma\left(1+\frac{1}{\beta_{1,2}}\right) \tag{9.5}$$

Examples of typical relaxation data and their fits are in figure 9.1.

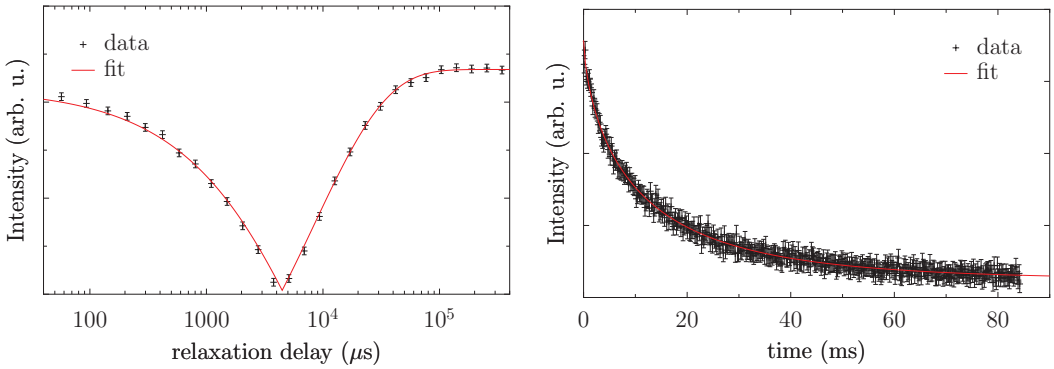

Figure 9.1: Left: Example of inversion recovery data used to determine longitudinal relaxation time T_1. Right: Example of CPMG data used to determine transversal relaxation time T_2.

We measured NMR relaxation of all six spheres, in T–V14 series we chose samples from layers 7 and 9 for more detailed examination (because of their smallest/largest FMR linewidts within the series) in the other two samples only $12k$ line relaxation was measured. In $V24$ samples relaxations of all resonance

sample		τ_{rep} (ms)	$\langle T_1 \rangle$(ms)
T–V14 s.6	(A01)	100	10.9 ± 1.8
T–V14 s.7	(A03)	60	10.8 ± 1.1
T–V14 s.8	(A05)	100	10.7 ± 1.3
T–V14 s.9	(A07)	100	9.6 ± 1.1
V24 bottom c.	(A09)	50	6.2 ± 1.0
V24 bottom c.	(A11)	50	5.0 ± 1.1

Table 9.1: Repetition times τ_{rep} (time interval between consecutive scans) and longitudinal relaxation times of studied samples. One can see, that used repetition times were sufficiently long to allow system return to thermal equilibrium. For influence of repetition time on reliability of fit results see figure 9.2.

lines were observed. The only exception from the above were the $2b$ lines, in case of which it was not always possible to determine relaxation times with reasonable accuracy due to low signal to noise ratio, however the observed longitudinal relaxation data did have the characteristic minima of intensity for relaxation delays about 5ms.

In the fit of inversion recovery data we used the A and B constants in order to correct for possible errors in experiment optimization (equation 9.3). To test its effect we performed two experiments where we swept vital pulse sequence parameters (pulse intensity and relaxation delay) and used them to acquire inversion recovery data.

In figure 9.2 on the left there are results of inversion recovery experiments performed with varying pulse level measured $12k$ line of sample A05 (T–V14 series, slice 8). If excitation conditions are not optimal, the obtained β parameter decreases which results in shorter $\langle T_1 \rangle$ regardless of whether too strong or too weak pulses were applied.

Dependence of inversion recovery results on used repetition time τ_{rep} is in figure 9.2 on the right. If $\tau_{\mathrm{rep}} > 5\langle T_1 \rangle$ the obtained relaxation time does no longer depend on repetition time. The dependence was measured on $4f_2$ line of sample A03 (T–V14 series, slice 7).

The rf power level was checked with step of 1dB – its error should be less than this value, and the repetition times were set to be above $5\langle T_1 \rangle$ (table 9.1) hence artificial shortening of observed longitudinal relaxations due to imperfections of experiment optimization should be below 0.5ms.

Based on our experience with fitting the data we estimate error in mean relaxation time $\langle T_{1,2} \rangle$ to be at least 1 ms for $\langle T_1 \rangle$ and at least 2 ms for $\langle T_2 \rangle$.

The T_2 results are meant for rough orientation only – the applied technique where the echoes themselves instead of their Fourier transforms are used is not

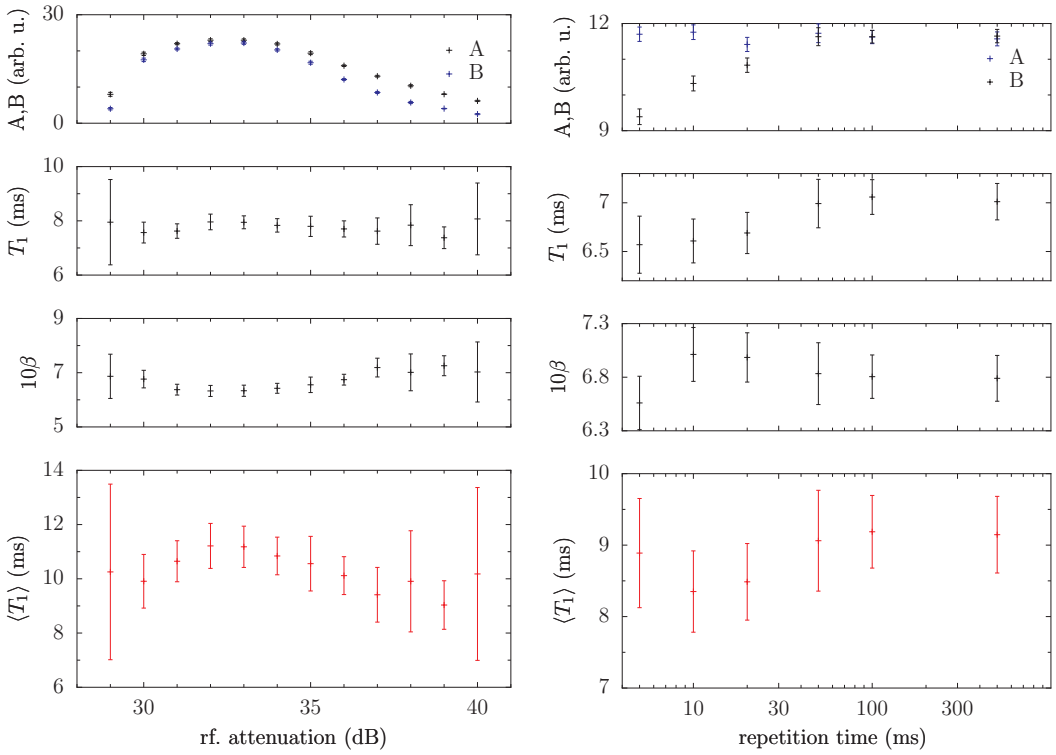

Figure 9.2: Left: Dependence of inversion recovery fit results on rf pulse intensity. If excitation is not optimal (optimum corresponds to maximum of A in top panel) the resulting relaxation time is artificially shortened. Right: Dependence of the fit results on repetition time (for optimal amplitude of rf. pulses). Long enough repetition time needs to be set, otherwise results are biased towards shorter relaxation times. Errors are from fits only. Mean longitudinal relaxation times $\langle T_1 \rangle$ are calculated from fit results using equation 9.5

Sample		$\langle T_1 \rangle$(ms)	$\langle T_2 \rangle$(ms)	FMR LW(Oe)
T–V14 s. 6	(A01)	10.9 ± 1.8	14.9 ± 2.1	73.7
T–V14 s. 7	(A03)	10.8 ± 1.1	16.1 ± 2.6	76.3
T–V14 s. 8	(A05)	11.2 ± 1.3	14.2 ± 2.1	70.3
T–V14 s. 9	(A07)	9.6 ± 1.1	16.8 ± 2.7	58.3
V24 bottom c.	(A09)	6.2 ± 1.0	9.4 ± 2.8	96.3
V24 bottom c.	(A11)	5.0 ± 1.1	5.4 ± 2.1	57.7

Table 9.2: Mean values of longitudinal (T_1) and transversal (T_2) relaxation times observed at $12k$ line of all samples together with FMR linewidths.

very accurate.

In the sample T–V13 relaxation times were not determined by above described techniques. From the data recorded during optimization of repetition times for measurement of spectra we estimate the T_1 to be roughly about $100 - 200$ ms as the signal intensity did not increase significantly with increasing τ_{rep} for $\tau_{\text{rep}} > 1$ s.

Table 9.2 provides a brief comparison of all six spheres, there are mean values of observed relaxation times for all five samples measured at $12k$ resonance line. All results of relaxation experiments are presented in table 9.3.

The most pronounced difference is between T–V14 and V24 series – relaxation times of the latter are about half of those of the former. Within each series the relaxation times vary and there seems to be a weak correlation with the FMR linewidth – samples with narrower FMR lines tend to have shorter $\langle T_1 \rangle$. Nevertheless, the observed differences within a sample series are comparable to experimental error.

In case of transversal relaxation the errors are larger and there is bigger spread of $\langle T_2 \rangle$ within one sample, however in case of T–V14 series the $\langle T_2 \rangle$ seems to be uncorrelated with position of layer (and with FMR linewidth) and it V24 also the $\langle T_2 \rangle$ tend to shorten as FMR linewidth decreases.

Relaxation times do not vary much among sublattices, this is most likely true also for the $2b$ sublattice although in this case most observations were rather qualitative.

The observed relaxation times are remarkably short for a M type hexaferrite at 4.2 K, furthermore quite generally there is $T_1 < T_2$ (which is close to the limit $T_2 \leq 2T_1$). In pure BaM T_1 is of the order of hundreds of miliseconds or more and $T_2 \ll T_1$ [69, 70]. This means that in studied samples main contribution to both relaxation times comes from energy exchange between nuclei and "lattice". Processes related to slow (compared to resonance frequency) fluctuations of magnetic field on nuclear site, which induce loss of coherence

s.	line	T_1(ms)	$10\beta_1$	$\langle T_1\rangle$(ms)	T_2(ms)	$10\beta_2$	$\langle T_2\rangle$(ms)
	$2b$	-	-	-	-	-	-
A01	$12k$	8.5 ± 0.7	6.9 ± 0.4	10.9 ± 1.8	11.5 ± 0.2	6.8 ± 0.1	14.9 ± 2.1
V14	$4f_{\mathrm{IV}}$	-	-	-	-	-	-
s. 6	$2a$	-	-	-	-	-	-
	$4f_{\mathrm{VI}}$	-	-	-	-	-	-
	$2b$	9.4 ± 1.1	6.5 ± 0.7	12.9 ± 4.2	11.2 ± 0.4	6.4 ± 0.3	15.6 ± 4.2
A03	$12k$	8.4 ± 0.2	6.9 ± 0.1	10.8 ± 1.1	11.3 ± 0.5	6.3 ± 0.3	16.1 ± 2.6
V14	$4f_{\mathrm{IV}}$	8.7 ± 1.1	6.7 ± 0.5	11.4 ± 2.5	11.1 ± 0.3	6.7 ± 0.2	14.6 ± 2.2
s. 7	$2a$	8.1 ± 0.3	6.9 ± 0.3	10.4 ± 1.3	9.6 ± 0.5	6.6 ± 0.3	13.0 ± 2.4
	$4f_{\mathrm{VI}}$	7.0 ± 0.2	6.8 ± 0.2	9.1 ± 1.3	8.3 ± 0.3	6.9 ± 0.2	10.7 ± 2.1
	$2b$	-	-	-	-	-	-
A05	$12k$	8.0 ± 0.2	6.3 ± 0.2	11.2 ± 1.3	10.7 ± 0.3	6.7 ± 0.2	14.2 ± 2.1
V14	$4f_{\mathrm{IV}}$	-	-	-	-	-	-
s. 8	$2a$	-	-	-	-	-	-
	$4f_{\mathrm{VI}}$	-	-	-	-	-	-
	$2b$	-	-	-	-	-	-
A07	$12k$	7.3 ± 0.1	6.7 ± 0.2	9.6 ± 1.1	11.7 ± 0.5	6.3 ± 0.3	16.8 ± 2.7
V14	$4f_{\mathrm{IV}}$	7.1 ± 0.2	6.8 ± 0.2	9.3 ± 1.1	11.8 ± 0.8	6.4 ± 0.4	16.5 ± 3.1
s. 9	$2a$	7.4 ± 0.8	6.9 ± 0.5	9.5 ± 1.8	9.1 ± 0.4	8.0 ± 0.5	10.3 ± 2.2
	$4f_{\mathrm{VI}}$	6.4 ± 0.2	6.6 ± 0.2	8.6 ± 1.2	9.0 ± 0.4	7.3 ± 0.4	10.9 ± 2.2
	$2b$	4.9 ± 0.3	8.6 ± 0.7	5.3 ± 3.1	-	-	-
A09	$12k$	4.7 ± 0.1	6.7 ± 0.2	6.2 ± 1.0	6.2 ± 0.6	5.9 ± 0.5	9.4 ± 2.8
V24	$4f_{\mathrm{IV}}$	5.3 ± 0.2	6.9 ± 0.3	6.8 ± 1.1	6.6 ± 0.7	7.1 ± 0.8	8.3 ± 2.6
	$2a$	5.7 ± 0.2	6.9 ± 0.3	7.3 ± 1.2	6.3 ± 0.4	7.6 ± 0.6	7.5 ± 2.2
	$4f_{\mathrm{VI}}$	5.4 ± 0.5	6.6 ± 0.6	7.3 ± 1.7	6.1 ± 0.6	6.0 ± 0.6	9.3 ± 3.0
	$2b$	-	-	-	-	-	-
A11	$12k$	3.6 ± 0.2	6.4 ± 0.3	5.0 ± 1.1	4.0 ± 0.2	6.6 ± 0.3	5.4 ± 2.1
V24	$4f_{\mathrm{IV}}$	4.6 ± 0.1	7.0 ± 0.2	5.8 ± 1.0	5.7 ± 0.2	7.6 ± 0.3	6.8 ± 2.0
	$2a$	4.2 ± 0.1	6.9 ± 0.2	5.4 ± 1.0	4.1 ± 0.2	7.4 ± 0.4	5.0 ± 2.1
	$4f_{\mathrm{VI}}$	3.5 ± 0.1	6.6 ± 0.2	4.8 ± 1.0	4.5 ± 0.8	6.5 ± 0.1	6.1 ± 2.0

Table 9.3: NMR relaxations – full comparison.

(and contribute only to T_2) play only a minor role.

Presence of the relaxation times distribution rather than single-exponential decays may be understood in terms of relaxation times varying throughout the sample, e.g. due to relaxation time dependence on distance from a relaxation centre.

Increasing Sc concentration appears to shorten the relaxation times – samples from V24 series ($x_{\mathrm{Sc}} = 0.3$) have the relaxation times about half of those of samples from T–V14 series ($x_{\mathrm{Sc}} = 0.2$) and in T–V13 sample ($x_{\mathrm{Sc}} = 0.06$) the longitudinal relaxation is about order of magnitude larger than in the spheres.

9.4.2 Spectra

Observed NMR spectra of all samples are in figure 9.3. Within a series, the line profiles are very consistent. The $12k$ and $4f_{\mathrm{VI}}$ lines are apparently broader than the $4f_{\mathrm{IV}}$ and $2a$. The $2b$ line is broadened towards higher frequencies (this may be interpreted as unresolved satellite structure on $2b$ resonance). There are several satellites lines, next to $12k$ resonance, the most distinct one is centered at 70.7 MHz. There is also weak satellite at frequency above that of $4f_{\mathrm{VI}}$ line in spectrum of T–V13 sample, in spectra from samples with higher Sc contents, the $4f_{\mathrm{VI}}$ resonances have a weak shoulders on its frequency – the satellite is probably broadened and overlapped with the main $4f_{\mathrm{VI}}$ lines.

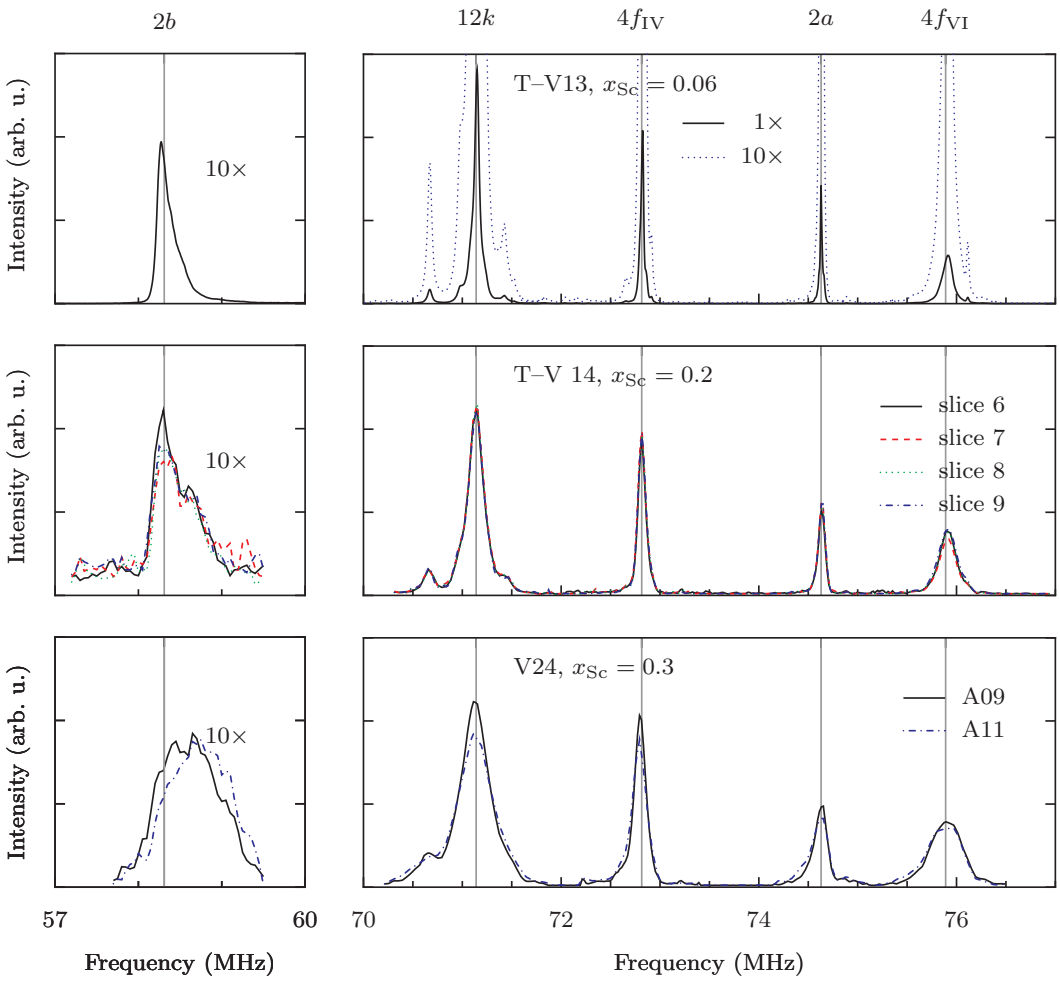

Figure 9.3: ^{57}Fe NMR spectra of all studied samples. Positions of resonance lines in BaM ferrite are shown.

Sample	x_{Sc}	Intensity	$^{4f_{VI}}x_{Sc}$	$^{2b}x_{Sc}$
T–V13	0.06	0.26 ± 0.02	0.044 ± 0.004	0.043 ± 0.003
T–V14	0.20	0.48 ± 0.12	0.084 ± 0.022	0.080 ± 0.020
V24	0.30	0.57 ± 0.15	0.10 ± 0.03	0.095 ± 0.025

Table 9.4: Intensities of $12k$ satelite at 70.7 MHz estimated from spectra in normalization which has total intensity of $12k$ resonance equal to 6. The last two columns correspond to theoretical concentrations of Sc in $4f_{VI}$ or $2b$ sublattice given that the satellite is induced by Sc in the particular sublattice.

The consistency of spectra indicates that there are no significant variations of composition amongst samples from given series.

The observed spectral features (line broadening with increasing Sc content and formation of satellites on $2b$, $12k$ and $4f_{\mathrm{VI}}$ lines) can be understood as effect of Sc entering preferentially the $4f_{\mathrm{VI}}$ and $2b$ sublattices, as $4f_{\mathrm{VI}}$ site is coupled to three $2b$ sites, six $12k$ sites and is very close to one $4f_{\mathrm{VI}}$ site. A $2b$ site is coupled to six $4f_{\mathrm{VI}}$ sites and six $12k$ sites.

The satellite at 70.7 MHz is probably coming from $12k$ sites with one Sc substitution in vicinity, however it cannot be decided whether the Sc is in $4f_{\mathrm{VI}}$ site or $2b$ site adjacent to resonant $12k$ site. The remaining satellite structure on $12k$ line is probably induced by Sc in the second sublattice, situations where there are more than one substitution atoms in vicinity of resonant $12k$ nucleus and effect of further lying substitution atoms.

We estimated intensities of the satellite from integrals of spectra and fits of resonance lines. Results are listed in table 9.4 together with calculated concentrations of Sc in $4f_{\mathrm{VI}}$ and $2b$ sublattices. The calculations are based on assumption that the satellite is due to Sc in sublattice for which the concentration is evaluated.

The calculated concentrations in both models (the satellite being due to Sc either in $4f_{\mathrm{VI}}$ or $2b$) are quite close to each other. Ratio of Sc concentration in one of sublattices to total Sc concentration drops as more Sc is added into the system, this indicates that the preference is lost gradually, and distribution of Sc amongst the sublattices changes as total Sc concentration increases. The observed preference of Sc towards $2b$ and $4f_{\mathrm{VI}}$ sites is in accord with results of Mössbauer studies [71–73].

9.5 Summary

Based on ^{57}Fe relaxations and spectra we found, that spheres within a series have very similar microstructure which is nearly independent on position of sphere within original crystal. We found possible correlation between NMR relaxations and FMR linewidth within a series, however the observed differences in NMR relaxations are comparable to experimental error.

The Sc significantly enhances longitudinal relaxation which in samples with $x_{\mathrm{Sc}} = 0.3$ four orders of magnitude faster than what is typical for non-substituted M ferrite.

The spectra indicate that Sc enters $2b$ and $4f_{\mathrm{VI}}$ sublattices and ratio of concentrations of Sc in the sublattices appears to be dependent on total Sc content.

Chapter 10

La substituted and La+(Zn, Cu, Co) co-substituted SrM

10.1 Introduction

In this chapter we deal with substituted SrM powder systems. In first part, effects of substitution on large cation site are discussed – divalent Sr is substituted by trivalent La thus inducing formation of ferrous ions. In second part co-substituted systems are studied: simultaneously with La–Sr substitution, iron is substituted by Zn, Co or Cu in order to compensate for extra charge brought into the systems by introduction of La.

Throughout this chapter spectra in region of $12k - 4f_{\mathrm{VI}}$ ^{57}Fe resonance are normalized to total area equal to $11 - x_{\mathrm{La}}$ where $x -$ La is La content. Such normalization yields (under *a posteriori* satisfied assumptions – see text) unit integral intensity per ferric ion in formula unit.

10.2 Samples

We studied five samples from LaSrM series: $Sr_{1-x}La_xFe_{12}O_{19}$, La content was varied in full available range: $x_{\mathrm{La}} \in \{0,\ 0.25,\ 0.5,\ 0.75,\ 1\}$. Samples are summarized in table 10.1. Next we studied nine doubly substituted samples $Sr_{1-x}La_xFe_{12-y}M_yO_{19}$, M $\in \{$Zn, Co, Cu$\}$, with La concentrations same as the three intermediate La concentrations in samples from LaSrM series, for each La concentration three samples were studied with iron partly substituted by Zn, Co or Cu, concentrations of substitutions are summarized in table 10.2.

All samples were in form of powders, they were were prepared by J. Töpfer from University of Applied Sciences Jena using standard ceramic process [74]. Doubly substituted samples were characterized by XRD and TEM in order to

Sample	SrM	La025	La050	La075	LaM
x_{La}	0.00	0.25	0.50	0.75	1.00

Table 10.1: Samples from La–Sr series, $Sr_{1-x}La_xFe_{12}O_{19}$

.

x_{La}	y		
	Zn	Co	Cu
0.25	0.25	0.21	0.20
0.50	0.30	0.30	0.20
0.75	0.40	0.35	0.20

Table 10.2: Doubly substituted samples of general formula: $Sr_{1-x}La_xFe_{12-y}M_yO_{19}$, M $\in$ {Zn, Co, Cu}.

detect second phases and by chemical titration to get amount of ferrous ions. Results are in tables 10.3, 10.4 and 10.5, for LaSrM systems substituted by Zn, Cu and Co respectively. In several samples traces of second phase were detected, amounts of ferrous ions detected by titration were generally higher than theoretical values based on nominal compositions of samples.

LaSrM:Zn

sample		phases		Fe^{2+} (wt%)	
x_{La}	y_{Zn}	SEM	XRD	theory	titration
0.25	0.25	single	single	0	–
0.50	0.30	single	single	1.02	1.18
0.75	0.40	second	single	1.77	2.09

Table 10.3: Characterization of Zn substituted LaSrM samples, second phases were looked for by SEM and XRD (single indicates no second phases were found, "second" indicates that traces of second phase were detected), amount of ferrous ions was measured by chemical titration.

LaSrM:Cu

sample		phases		Fe^{2+} (wt%)	
x_{La}	y_{Cu}	SEM	XRD	theory	titration
0.25	0.20	second	single	0.26	0.88
0.50	0.20	second	single	1.54	2.04
0.75	0.20	second	single	2.79	2.96

Table 10.4: Characterization of Cu substituted LaSrM samples, second phases were looked for by SEM and XRD (single indicates no second phases were found, "second" indicates that traces of second phase were detected), amount of ferrous ions was measured by chemical titration.

LaSrM:Co

sample		phases		Fe^{2+} (wt%)	
x_{La}	y_{Co}	SEM	XRD	theory	titration
0.25	0.20	second	single	0.26	0.88
0.50	0.20	single	single	1.54	2.04
0.75	0.20	single	single	2.79	2.96

Table 10.5: Characterization of Co substituted LaSrM samples, second phases were looked for by SEM and XRD (single indicates no second phases were found, "second" indicates that traces of second phase were detected), amount of ferrous ions was measured by chemical titration.

10.3 LaSrM systems

La substitution on large cation sites in SrM has been reported to modify magnetocrystalline anisotropy [9, 75, 76], which makes the hexaferrite system more attractive for some permanent magnet applications. In this section we deal with La–Sr distribution and charge compensation due to excess electrons introduced by La substitution. Mössbauer studies have shown, that the extra charge likely localizes on iron ions in $2a$ sublattice [77, 78]. We approached these matters by means of NMR experiment and electronic structure calculations.

10.3.1 NMR

^{57}Fe resonance from all five iron sublattices observed in all samples from LaSrM series are shown in figure 10.1. In case of intermediate compositions are the resonance lines significantly broadened. One can see formation of satellites S_1 and S_2, splitting of $2b$ and $4f_{\mathrm{VI}}$ lines into satellite patterns and weaker satellites at 70.5MHz and 73 MHz. As La content increases $12k$ and $4f_{\mathrm{IV}}$ lines merge into a common lineshape, similar interfusion takes place in case of $2a$ and $4f_{\mathrm{VI}}$ resonances. The $12k + 4f_{\mathrm{IV}}$ and $2a + 4f_{\mathrm{VI}}$ lineshapes remain well separated for all La concentrations. Despite the overlap, it can be seen, that intensity of $2a$ line gradually diminishes with increasing La content.

In case of LaM sample low frequency signal was observed up to 20 MHz consisting of three peaks centered at 9, 13, and 17 MHz; the spectrum is shown in figure 10.2. A NMR signal in this frequency range is present in intermediate samples as well, however rather than well resolved lines only a broad resonance stretching over the frequency range was found.

We ascribe the low frequency signal in LaM (figure 10.2) to resonance of ^{139}La . This interpretation is supported by electronic structure calculations (see below) and experiments in external field on LaM sample – we found that mean resonance frequency changed in accordance with gyromagnetic ratio of ^{139}La (as we studied powder sample, the resonance broadened severely upon application of the field).

Satellites on $2b$ and $4f_{\mathrm{VI}}$ lines can be explained by effect of disorder in large cation sublattice (see corresponding section in chapter 8) and are discussed in more detail in following subsection.

As transition from ferric to ferrous ion happens (extra charge is added to the ion), its ^{57}Fe resonance is expected to shift to low frequencies, line to broaden and relaxation times to shorten. “Purely” ferrous ions are usually invisible to ^{57}Fe NMR due to too fast relaxations. The diminishing $2a$ intensity indicates localization of ferrous ions induced by the La substitution in $2a$ sublattice.

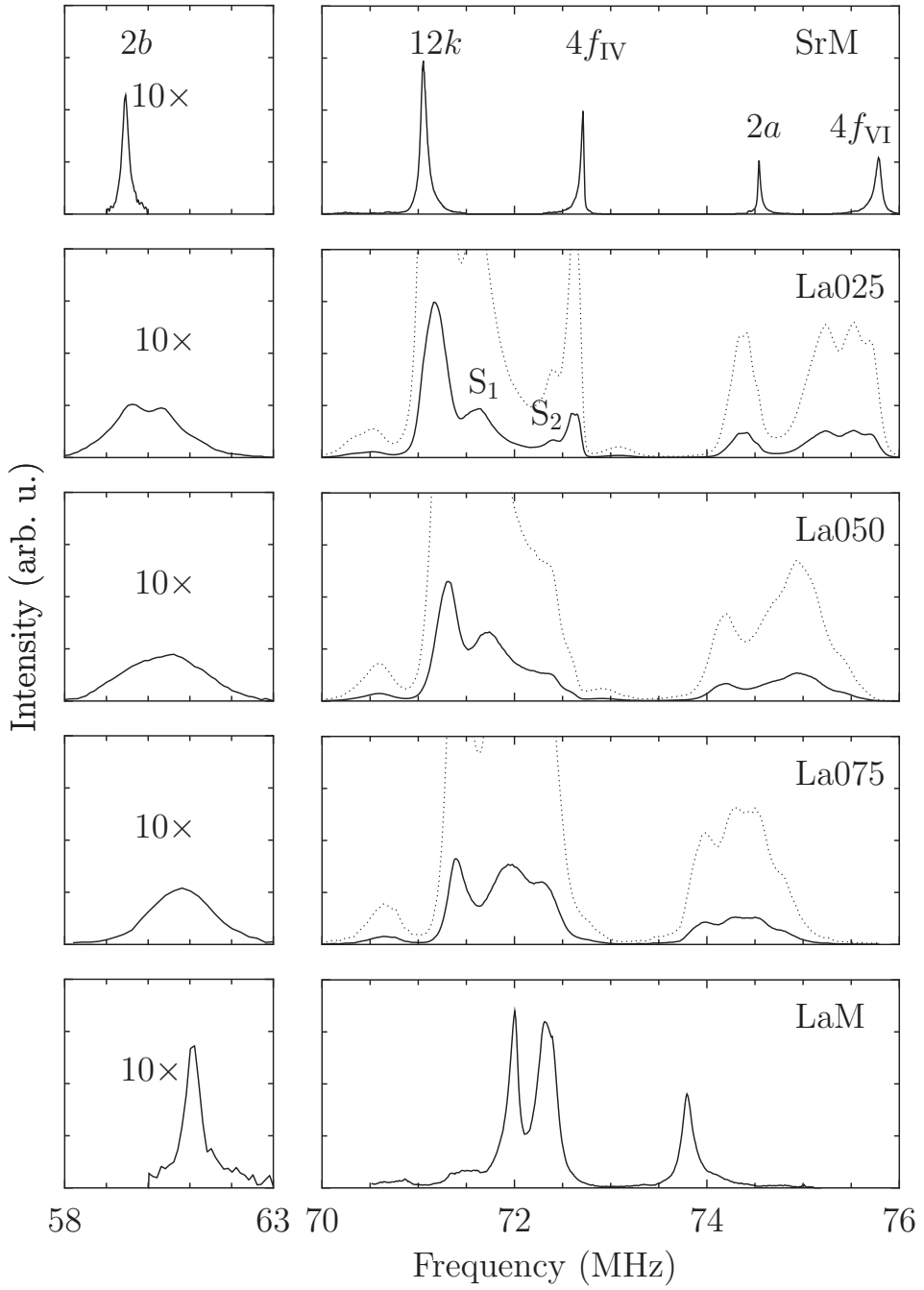

Figure 10.1: ^{57}Fe NMR spectra of LaSrM samples. The f^2 correction of intensities has been applied. The $2b$ lines are normalized to unit area, the $12k$-$4f_{\mathrm{VI}}$ profiles are normalized to $11 - x_{La}$ area. Dotted lines show intensities multiplied by 5.

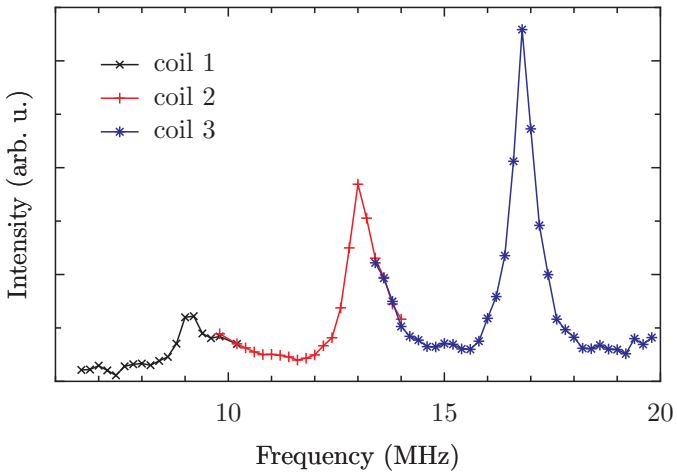

Figure 10.2: Low frequency NMR signal detected in LaM, three rf coils were used to cover the frequency range.

According to Štěpánková et al. [79] the satellites S_1 and S_2 are most likely resonances of ferric ions in $4f_{IV}$ sites altered by nn ferrous ions in $2a$ sublattice, in S_1 there is possibly also contribution from $12k$ sites.

Integral intensities of satellite at 70.5 MHz are roughly 0.2 in La025 sample and 0.3 in La050 and La075 samples, these are too low for the satellite to be induced by either La–Sr disorder in $2d$ sublattice or ferric–ferrous disorder in $2a$ sublattice. There are two plausible scenarios explaining the satellite: noncolinearity of magnetic structure or impurity in systems containing La. If some magnetic moments are canted, the resonance frequencies are to be altered by anisotropy of local magnetic field at nucleus. An impurity will induce satellite lines on resonances of its neighbors. It cannot be decided from the data, which of the above scenarios is valid, or whether there is some combination of the possibilities.

In canting scenario, the satellite probably comes from $12k$ resonance, as these sites have strong anisotropy of local field [66].

If the satellite is due to impurity which is present in samples containing La, we are inclined towards scenario of the impurity entering preferentially $4f_{IV}$ sublattice as the pattern (satellite at 70.5 MHz and weaker satellite at 73 MHz) is similar to that induced by Zn substitution entering $4f_{IV}$ sublattice on LaSrM spectra (see figure 10.8). Based on intensity of satellite at 71 MHz and interpretation of Zn substituted spectra (see below) we estimate impurity content to $x_{\text{impurity}} \approx 0.02$ in La025 sample and $x_{\text{impurity}} \approx 0.03$ in La050 and La075 samples.

In ^{57}Fe spectrum of LaM sample (frequency interval $60 - 75$ MHz) there are four distinct lines, however, the ortorhombic unit cell of LaM determined by Küpeferling et al. [9] has six inequivalent positions occupied by iron. It is expectable, that $4a$ sites (resonance of which diminished with increasing La content) are not seen in the spectrum, but there still are five sublattices left for the four lines. Based on development of spectra with increasing x_{La} it is quite clear, that line at 61 MHz comes from bipyriamidal $4b$ sites and that at 73.8 MHz from $8f_2$ sites. Küpferling et al. assigned line at 72 MHz to $8f_1$ resonance, line at 72.3 MHz to $16h$ and unresolved broad resonance in region $70.5 - 71.6$ MHz to $8f_3$ resonance. Integral intensities of the lines however do not comply with interpretation in [9] The unresolved resonance below 71.6 MHz has not sufficient intensity to come from $8f_3$ sublattice.

We propose interpretation in which line at 72 MHz is assigned to $16h$ resonance and line at 72.3 MHz to overlapped $8f_1$ and $8f_3$ resonances. This is in better agreement with integral intensities of the lines – in our spectrum the intensity is split roughly in ratio 1:1 between the lines, which complies with multiplicities of sites assigned to the lines in our interpretation. The resonance in $70.5 - 71.6$ MHz interval is probably induced by the above discussed canting or impurity. The line assignment is summarized in figure 10.3.

The proposed interpretation is also supported by experimental data reported in [9] – they studied temperature dependence of resonance in interval $71.5 - 72.7$ MHz and found, that with increasing temperature the line at 72.3 MHz splits into two components with approximately equal intensities. They ascribed the splitting to effect of canting of magnetic moments in $16h$ sublattice, we argue, that they merely observed temperature dependences of $8f_1$ and $8f_3$ resonance frequencies, which are different. The difference in temperature dependences is expectable since resonance frequency of $12k$ magnetic sublattice in M ferrite is known to drop upon increasing temperature faster than resonance frequencies of remaining sublattices [80, 81]. $16h$ and $8f_3$ sublattices originate from splitting of $12k$ sublattice due to symmetry change, they still should belong to same magnetic sublattice ($12k$), apparently their behavior on increasing temperature is not significantly altered by the change of lattice symmetry.

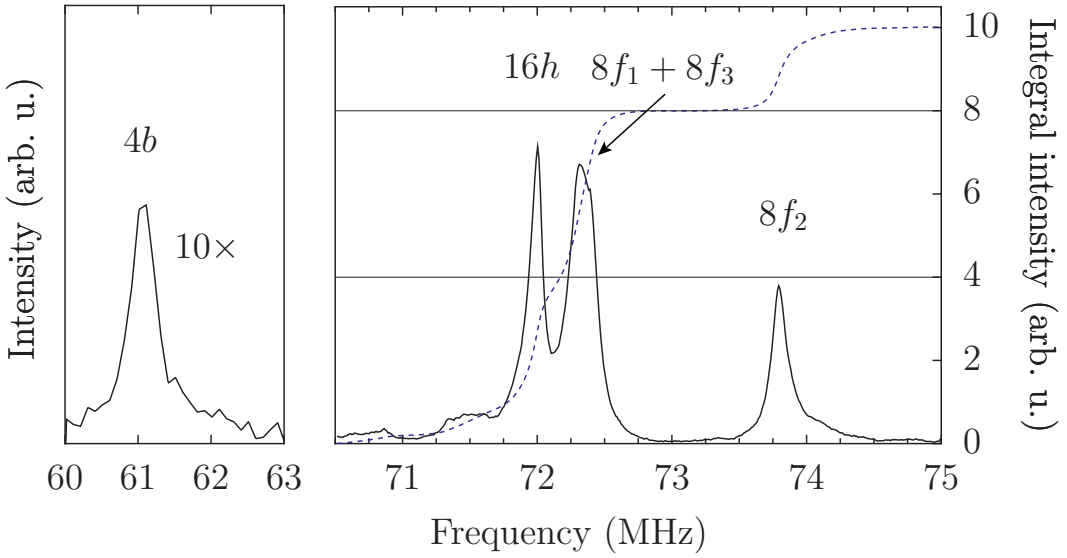

Figure 10.3: Our interpretation of LaM ^{57}Fe NMR spectrum. The dashed blue line correspond to integral intensity. In contrast to Küpferling et al. we assign the line at 72 MHz to 16h resonance and line at 72.3 MHz to overlapped signals from $8f_1$ and $8f3$ sublattices.

10.3.2 La–Sr distribution

In intermediate samples ($x_{\mathrm{La}} = 0.25,\ 0.50,\ 0.75$), there is disorder in large cation sites – each may be occupied either by Sr^{2+} or by La^{3+} cation. Interesting question is, whether the La–Sr distribution is random – probability of a 2d site being occupied by La or Sr is given only by La–Sr ratio and does not depend on occupations of neighboring 2d sites, or there is a preference either towards La–Sr segregation or intermixing.

To study the distribution we choose 2b resonance because these sites are in close vicinity of large cation sites hence sensitive to occupation of neighboring large cation sites, their NMR signal is well separated from rest of the resonances so there are no complications arising from overlap of spectral lines, and finally the ferrous ions are localizing in 2a sites, which are not among nn of 2b, which reduces influence of ferric–ferrous distribution on 2b resonance.

Employing the additivity model, we can write for frequencies of satellite lines induced by La on 2b resonance:

$$f(n) = f_0 + n\Delta f \tag{10.1}$$

where n is number of La nearest neighbors of resonant 2b site, Δf is change in resonance frequency induced by one La nn and f_0 is frequency of 2b resonance

in SrM. Within this framework, every added La ion acts only on its 3 nearest $2b$ neighbors hence increasing the mean 2b resonance frequency always by $3\Delta f/N_{2b}$ (N_{2b} is number of $2b$ sites in sample), yielding linear dependence of the mean frequency on La content:

$$f_{\mathrm{mean}}(x) = f_0 + 3\,x_{\mathrm{La}}\,\Delta f \tag{10.2}$$

Dependence of mean $2b$ resonance frequency on La content can be well fitted with linear function 10.2, see figure 10.4, fit results are in table 10.6.

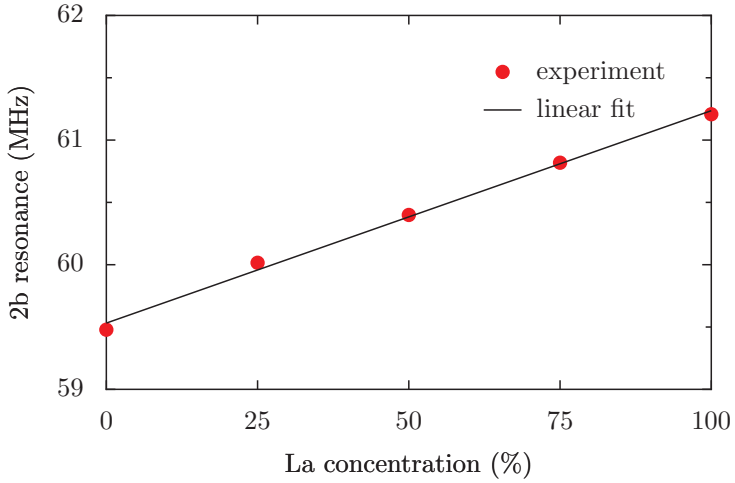

Figure 10.4: Center of mass of 2b resonance in LaSr - M hexaferrites versus La content. Individual datapoints correspond to spectra in fig 10.1, parameters of fitted line are in table 10.6.

f_0 (MHz)	Δf (MHz)	f(n)			
		$n=0$	$n=1$	$n=2$	$n=3$
59.53 ± 0.04	0.56 ± 0.02	59.53	60.09	60.65	61.22

Table 10.6: Results of linear fit of $2b$ resonance frequency and positions of $2b$ lines calculated from the fit results.

We decomposed experimental $2b$ profile of La025 sample into three lines of the same shape (lorentzian on arbitrary power k gave best results):

$$l_n(f) = I_n \left[\frac{w}{(f - f_n)^2 + w^2} \right]^k \tag{10.3}$$

There were 8 fitting parameters – two describing the lineshape (w, k), three for positions f_n and three for intensities I_n of the components. Fit results are summarized in table (10.7), fitted lineshape is in figure (10.5).

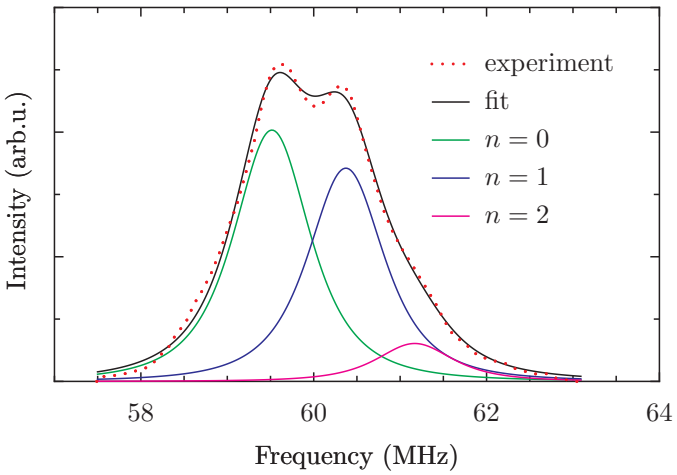

Figure 10.5: Fit of $2b$ resonance in La025 sample, individual components correspond to nuclei with n La nearest neighbors.

In the fit we disregarded fourth component corresponding to nuclei with all three nn being La at its relative intensity is too low. The intensities found by fit do not match those expected for sample with $x_{\mathrm{La}} = 0.25$ (see table 8.1), best agreement with prediction based on binomial distribution is found for $x_{\mathrm{La}} = 0.21$. This may indicate that either the real La content is somewhat smaller than nominal, or, that there is a slight tendency towards repulsion

n	w(MHz)	k	f_n(MHz)	I_n	bin(0.21)
0			59.516 ± 0.004	0.50 ± 0.03	0.49
1	0.71 ± 0.2	1.61 ± 0.04	60.372 ± 0.006	0.42 ± 0.03	0.39
2			61.17 ± 0.03	0.08 ± 0.01	0.10

Table 10.7: Fit results for La025 sample. Fitted intensities are compared to binomial distribution prediction for $x_{\mathrm{La}} = 0.21$ (bin(0.21)).

of La ions. The components found from fit are quite equidistant, which is in accord with additivity hypothesis.

The $2b$ resonances of intermediate samples with higher La content are rather featureless and did not reveal further detailed information on La–Sr distribution.

It is interesting to compare results of the two fits: from the linear fit we got $\Delta f = 560 \pm 20$ kHz while adjacent components of La025 $2b$ lineshape are on average 830 kHz apart, clearly one cannot consider f_0 and Δf in equation 10.1 as fixed, but as dependent on x_{La}. This is expectable – the additivity hypothesis is suited for small substitution contents while we attempted to apply it on case where full conceivable range of substitution content is used.

Similar decomposition of lineshape should be in principle possible for $4f_{\mathrm{VI}}$ lineshape (expected satellite pattern is analogous to that of $2b$), however it was not found practical. The $4f_{\mathrm{VI}}$ profile is in intermediate samples overlapped with that of $2a$ and lineshapes of its components are not likely to be symmetric. Qualitatively one can see, that the $4f_{\mathrm{VI}}$ resonance shifts towards low frequencies and that its splitting is in accord with predictions presented in chapter 8.

10.3.3 Electronic structure calculations

The main goal of performed electronic structure calculations was to gain insight on charged compensation in La–Sr M hexaferrite system. We also used the results to find theoretical ^{139}La NMR spectrum in LaM.

We calculated electronic structures of SrM and LaM using rotationally invariant version of LDA+U [82]. We used hexagonal unit cell for both systems. In final calculations radii of atomic spheres were 1.45 a.u. for oxygen, 2 a.u. for iron and 2.5 a.u. for large ions. In final calculations we used $R_{\mathrm{min}} K_{\mathrm{max}} = 6$ ($\approx$ 110 basis functions per atom), $G_{\mathrm{max}} = 16$ Ry$^{\frac{1}{2}}$ number of k points in irreducible part of first Brillouin zone was 8 and $U_{\mathrm{eff}} = 4.5$ eV.

In contrast to results reported by Novák et al. [83] we found that electronic structure calculations of LaM can produce two distinct solutions: one in which the extra charge is spread more or less uniformly over all iron sites (delocalized solution) and one in which the extra charge is concentrated on $2a$ sites only. This ambiguity is result of using the effective U, as this can produce additional local minima of energy functional which do not correspond to physical solutions.

Character of resulting density is sensitive to starting electron density – e.g. if one lowers (with respect to default starting state) initial magnetic moment of $2a$ ferrous ion, the result is going to be localized solution. While character of solution depends on starting electron density, once convergence is reached the

atom	valence			moment (μ_B)			volume (a.u.^{3})		
	SrM	LaM		SrM	LaM		SrM	LaM	
		del.	loc.		del.	loc.		del.	loc.
Fe ($2a$)	1.845	1.761	1.422	4.202	4.121	3.633	51.0	53.6	60.4
Fe ($2b$)	1.772	1.757	1.761	4.113	4.110	4.114	60.9	60.3	60.0
Fe ($4f_{\mathrm{IV}}$)	1.786	1.777	1.765	-4.112	-4.102	-4.004	64.4	65.3	65.5
Fe ($4f_{\mathrm{VI}}$)	1.857	1.846	1.845	-4.167	-4.169	-4.100	52.2	53.7	54.0
Fe ($12k$)	1.819	1.772	1.819	4.197	4.156	4.217	52.3	53.6	52.6
O ($4e$)	-1.233	-1.238	-1.231	0.423	0.397	0.418	80.6	80.8	80.7
O ($4f$)	-1.240	-1.246	-1.247	0.100	0.083	0.141	81.7	82.2	83.0
O ($6h$)	-1.235	-1.226	-1.224	0.033	0.039	0.043	85.6	82.1	82.0
O ($12k$)	-1.243	-1.250	-1.247	0.100	0.083	0.059	80.0	81.8	81.9
O ($12k$)	-1.225	-1.232	-1.227	0.208	0.137	0.149	83.1	81.4	80.8
La/Sr ($2d$)	1.646	2.152	2.154	-0.005	-0.015	-0.003	113.9	129.0	128.5
interstitial	0.005	0.008	0.003	-0.077	-0.024	-0.023	0.01	0.05	0.43

Table 10.8: Comparison of calculated valences, magnetic moments and volumes of atoms in SrM and LaM. For LaM results obtained from delocalized (del.) as well as localized (loc.) solutions are presented.

resulting density (either localized or delocalized) is independent of the initial density. Total energy of the localized solution is 0.64 eV lower, than that of delocalized solution, hence we conclude, that the localized solution corresponds to actual electron density in LaM.

Valence of iron can be inferred either directly from electron density contained within atom volume, or from magnetic moments of ions. Ferric as well as ferrous ions are expected to be in high spin state thus having spin magnetic moments close to free ion values i.e. 5 μ_B and 4 μ_B respectively – reduction of spin magnetic moment indicates transition from ferric to ferrous state. To extract valences as well as spin magnetic moments of ions we used the AIM program, results are shown in table 10.8.

As one can see, main difference between localized LaM solution and the rest is on $2a$ site – its valence is reduced by about 0.35, magnetic moment is reduced by $0.5\mu_B$ and atomic volume is increased. Variations of valences, moments and atomic volumes of other sites are significantly smaller than those of $2a$.

Next it is evident, that simple picture based on formal valences of ions is not entirely correct – all calculated valences are significantly smaller than the nominal values. Similar observation can be made for magnetic moments: none of the ferric ions has 5 μ_B moment, and there are non-negligible moments of

oxygen anions.

La atom (see table 10.8) adds only about half electron to the LaM system (in comparison to SrM), in delocalized solution this extra charge is distributed uniformly amongst Fe sites (and to smaller extent also amongst oxygen anions), while in localized solution most (but not all) extra charge is localized on $2a$ site while the rest is again uniformly distributed amongst the remaining sites. It is interesting to note, that the calculated valence of La is independent of charge localization.

Volume of $2a$ atom is in localized case significantly larger than in the remaining two as the atom needs to accommodate more charge. From differences of electron densities of localized and delocalized solutions it can be seen, that the extra charge is in minority $d(z^2)$ orbital, orientation of its z axis is parallel with local threefold symmetry axis, which is parallel with hexagonal axis of the unit cell (i.e. the z axis does not coincide with any of body diagonals of the octahedron).

The calculations were performed in hexagonal unit cell, however experiments [9] indicate orthorhombic symmetry of LaM system. Preliminary calculations on orthorhombic LaM have shown, that localized solution is present in this symmetry as well.

Further we extracted hyperfine parameters on La nuclei and used them to calculate theoretical ^{139}La NMR spectrum. The obtained positions and intensities of nuclear transitions were convoluted with common line profile (equal widths for all lines) and resulting spectrum was multiplied by squared frequency to allow direct comparison with experimental data. Calculated hyperfine parameters are in table 10.9, comparison of experimental and calculated spectra is in figure 10.6. Calculated and experimental spectra do show qualitative agreement although the positions of resonance lines do not match exactly.

B_{hf} (T)	B_{lattice} (T)	B_{loc} (T)	V_{zz} (10^{21} Vm^{-2})	η
0.286	0.547	0.833	-13.92	0

Table 10.9: Calculated hyperfine parameters on La nuclei in LaM. Magnetic field and z axis of EFG tensor are parallel with hexagonal axis. Hyperfine and lattice contributions to total local magnetic field are also shown.

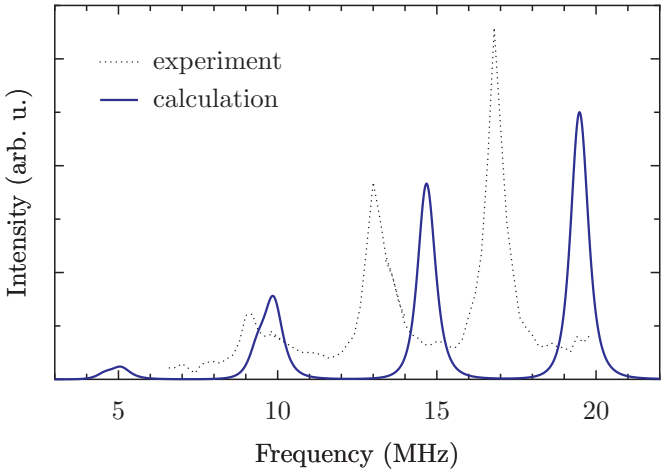

Figure 10.6: Comparison of calculated and experimental ^{139}La NMR spectra of LaM. Frequencies below 6 MHz are out of range accessible by our experimental setup.

10.3.4 Fe^{2+} localization

Calculations indicate, that extra charge in LaM localizes on $2a$ sites, this is supported also by NMR experiment in which line corresponding to $4a$ position (in $Cmcm$ spacegroup) in LaM is missing. To gain more quantitative picture from experimental spectra we normalized the $12k - 4f_{\mathrm{VI}}$ profiles to have total area of $11 - x_{\mathrm{La}}$. In such normalization we should have unit area per ferric ion in formula unit (as ferrous ions are not seen in the spectrum). We then integrated intensity of $12k + 4f_{\mathrm{IV}}$ profile and of $2a + 4f_{\mathrm{VI}}$ profile in all five samples and plotted the results in figure 10.7.

Intensity of $12k + 4f_{\mathrm{IV}}$ remains constant in whole sample series, while intensity of $2a + 4f_{\mathrm{VI}}$ gradually diminishes in good accordance with idea that every added La atom induces transition of one $2a$ ion from ferric to ferrous state. These experimental data indicate, that the charge localization on $2a$ sites takes place also in samples with intermediate La concentrations and that it is static on timescale of NMR experiment (0.1 μs – 1 ms, see below). If there was fast hoping, or delocalization, of the extra charge within $2a$ sublattice, its effect on $2a$ sites would be averaged, it probably would yield more complicated dependence of $2a$ intensity on La content than simple $I_{2a} = 1 - x_{\mathrm{La}}$ since the extra charge would affect more than one $2a$ site at the time. Also significant shift and broadening of $2a$ line with increasing x_{La} should have been observed in fast hoping regime (analogous to fast chemical exchange [25]).

The timescale on which the charge distribution should be static depends

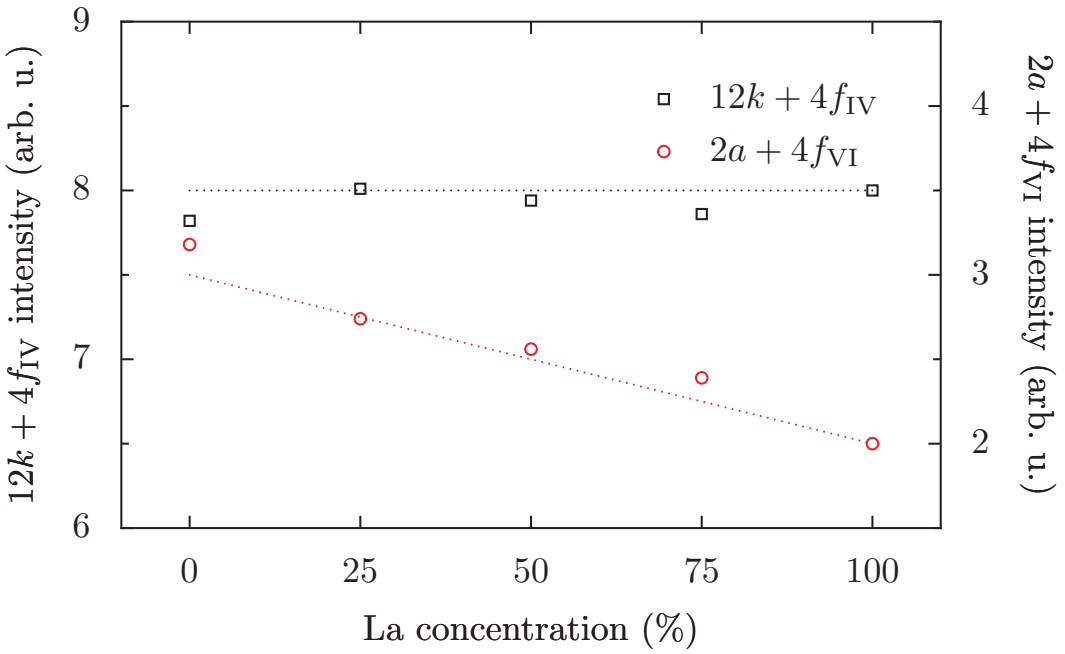

Figure 10.7: Integral intensities of ^{57}Fe $12k + 4f_{\mathrm{IV}}$ resonance and $2a + 4f_{\mathrm{VI}}$ resonance in LaSrM samples as a function of La concentration. Total integral intensity was normalized to $11 - x_{\mathrm{La}}$ in order to correspond to number of ferric ions resonating in frequency range of $12k - 4f_{\mathrm{VI}}$ signals in formula unit. The lines correspond to theoretical intensities in scenario when intensity of $2a$ resonance is due to charge localization reduced proportionally to La content.

on what mechanisms of spectra alteration by fast hoping charge one takes into account. In model based on analogy with chemical exchange [25] sites with or without localized charge have resonance frequencies f_1 and f_2, which in case of ferric–ferrous exchange should differ by few tens of MHz. Fast and slow regime are then defined by inverse of the frequency difference (0.1 μs), if ion changes its valence on shorter timescale one resonance line on average frequency is observed, if it keeps its valence for longer time, two separate lines – one for each state, should be observed. However, the extra charge does not only induce change of local field (and resonance frequency), but it also, and more importantly, leads to broadened lines and changes relaxation times – in ferrous ions the relaxation times are expected to be too short to allow observation of NMR signal by pulse techniques (i.e. below several μs). The hoping extra charge should wipe out resonance of all ions it "visits" during the whole NMR experiment, thus significantly enhancing apparent T_2 relaxation of $2a$ resonance.

This enhancement of $2a$ T_2 relaxation however was not observed, from which one may be inclined to conclude, that charge distribution is static during the whole NMR pulse sequence, which in our case was about half milisecond.

Localization of excess charge in $2a$ sublattice together with its slow (or absent) hopping justifies interpretation of unit integral intensity in $12k - 4f_{\mathrm{VI}}$ range as coming from one ferric ion per formula unit when normalization of total integral intensity in this range to $11 - x_{\mathrm{La}}$ is applied.

10.4 Doubly substituted systems

In this section we present experimental NMR data obtained on doubly substituted samples of $\mathrm{Sr}_{1-x}\mathrm{La}_x\mathrm{Fe}_{12-y}\mathrm{M}_y\mathrm{O}_{19}$, $\mathrm{M} \in \{\mathrm{Zn},\ \mathrm{Co},\ \mathrm{Cu}\}$ where the excess charge brought to system by La is partly compensated by substitution of iron by divalent M atoms hence reducing amount of ferrous ions needed to maintain neutrality. Compositions of samples were summarized in table 10.2.

For the interpretation of integral intensity normalized to number of ferric ions per formula unit to work as described above also for doubly substituted systems one must further assume that substitution is indeed divalent, and that it does not enter the $2b$ sublattice.

In following text we will firs summarize experimental results and then discuss the individual sample series in separate subsections.

10.4.1 NMR spectra

In figure 10.8 there are ^{57}Fe spectra of all nine doubly substituted samples compared to that of samples from LaSrM series with the same La contents. One can see that in $12k - 4f_{\mathrm{VI}}$ region, that effects of Zn and Cu are most different from each other, Co induces changes, which bear some resemblance to that induced by Zn in region $69.5 - 73$ MHz, while at higher frequencies (above 73 MHz) its effect is more similar to that of Cu. Satellite at 69 MHz is observed only for Cu substitution.

Effect of Zn and Co on $2b$ line is similar and not too strong – the line is slightly broadened by the substitutions. In Cu substituted samples, the profile is altered significantly: in sample with $x_{\mathrm{La}} = 0.25$ and to some extent also in sample with $x_{\mathrm{La}} = 0.5$ the resonance is of quite complex profile, which is dependent on excitation conditions, in sample with $x_{\mathrm{La}} = 0.75$ the profile is smooth, consisting of two components with ratio of integral intensities approximately 1:2.

Signal in region of $2b$ resonance observed in Cu substituted samples differs significantly from those observed for other LaSrM samples. In sample with

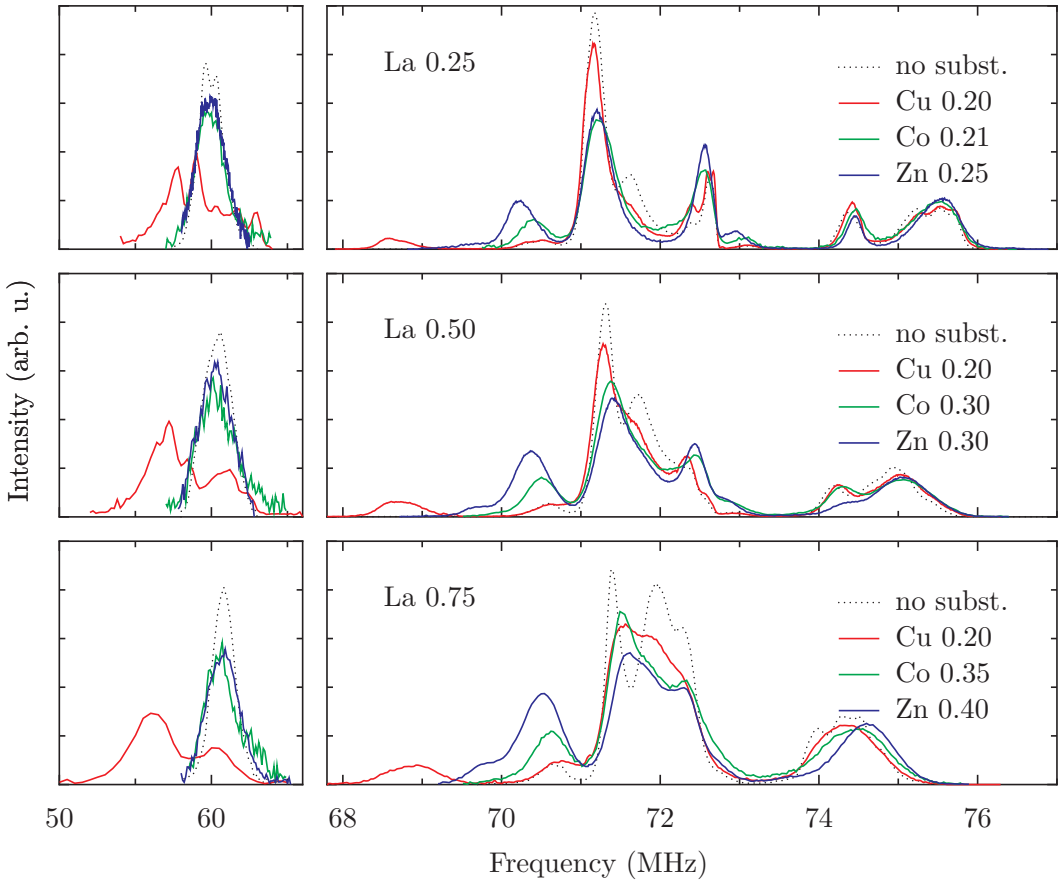

Figure 10.8: ^{57}Fe spectra of La–SrM systems with small cation substitutions, compared to these of non-substituted La–Sr samples. Spectra in each of six plots are normalized to equal areas, scales of individual plots differ.

smallest La content it is of rather complex profile, in samples with higher La content it takes form of two peaks with ratios of intensities about 1:2 and centered about 5 MHz apart. As La content increases (Cu content is the same in all three Cu substituted LaSrM samples), the resonance shifts to lower frequencies.

The spectrum observed in $50 - 65$ MHz range on Cu substituted LaSrM is quite unusual for ^{57}Fe resonance from $2b$ sites, its peculiarity led us to suspicion that the signal may be of other origin. Ratio of intensities of its two components in $x_{\mathrm{La}} = 0.75$ sample together with ratio of frequencies at which the components are centered correspond well to natural abundances and gyromagnetic ratios of ^{63}Cu and ^{65}Cu nuclei (see table 5.1). We measured

this part of spectrum in external field of ≈ 0.7 T at 4.7 K, results are shown in figure 10.9. In external field the spectrum (apart from broadening) shifted to higher frequencies by approximately 3 MHz, such a shift is too much for the signal to be ^{57}Fe resonance but is easily in reach of ^{63}Cu and ^{65}Cu resonance ($\gamma_{\mathrm{Cu}} B_{\mathrm{ext}} \approx 7.9$ and 8.5 MHz for ^{63}Cu and ^{65}Cu respectively; the observed shift is lower due to effect demagnetizing fields). We conclude, that in Cu substituted samples ^{57}Fe 2*b* resonance is overlapped with stronger resonances of ^{63}Cu and ^{65}Cu which accidentally fall into same frequency range.

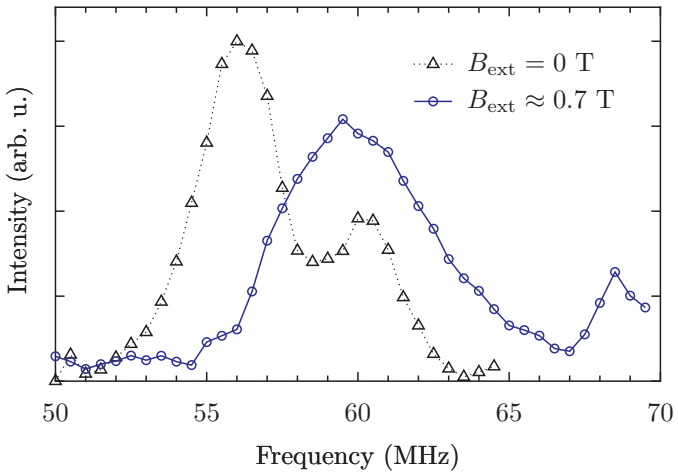

Figure 10.9: NMR signal in $La_{0.75}Sr_{0.25}Fe_{11.8}Cu_{0.2}O_{19}$ powder sample measured at 4.2K in zero external field and at 4.7 K in field of approximately 0.7 T. The shift of spectral profile is about 3 MHz, too large to be resonance of ^{57}Fe, thus indicating that the signal comes from ^{63}Cu and ^{65}Cu nuclei. Above 67 MHz there is ^{57}Fe resonance from $12k - 4f_{\mathrm{VI}}$ region.

Upon further investigation of the 50–65 MHz region in $x_{\mathrm{La}} = 0.25$ Cu substituted sample we found, that the spectral profile is strongly dependent on intensity of applied excitation pulses, spectra for three different rf pulse intensities are shown in figure 10.10. Spectral profile observed for rf attenuation 8 dB quite resembles resonance of ^{57}Fe in 2*b* sublattice seen in other samples. Profile observed at 14 dB attenuation (half rf field amplitude than the 8 dB), had maximal intensity, upon further reduction of rf pulses the signal gradually diminished as whole. Optimal excitation conditions for ^{63}Cu + ^{65}Cu and ^{57}Fe nuclei in this sample probably differ, thus allowing for observed separation of the overlapped signals – the line observed with strong pulses is likely dominated by ^{57}Fe resonance, while the profile observed for weaker pulses comes from ^{63}Cu and ^{65}Cu nuclei. In samples with higher La content we were not able to

separate ^{57}Fe from ^{63}Cu and ^{65}Cu resonance by altering excitation conditions.

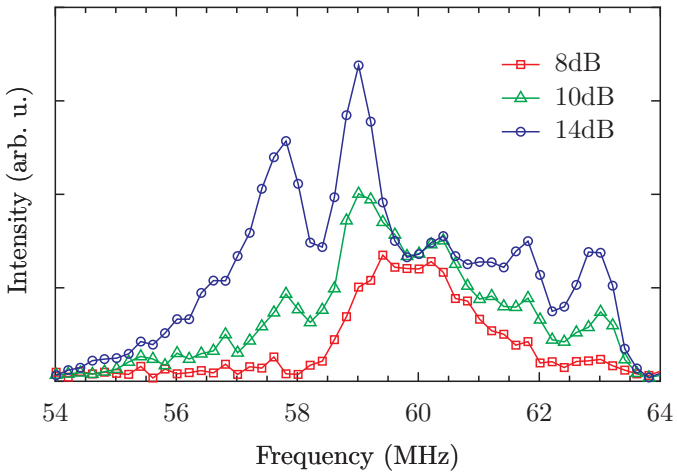

Figure 10.10: NMR spectra of $La_{0.25}Sr_{0.75}Fe_{11.8}Cu_{0.2}O_{19}$ obtained in zero external field at 4.2K for three rf pulse levels. Pulses with attenuation 8 dB were the strongest we were able to apply, for attenuation 14 dB we observed strongest NMR signal. Increase of attenuation by 6 dB corresponds to reduction of applied rf field amplitude to half. Spectra are plotted in common intensity range, no normalizations nor corrections were applied.

In Co substituted samples we observed NMR signal in range of 250 – 600 MHz (see figure 10.11), which we attribute to ^{59}Co resonance. The signal was observed using untuned broadband probehead, for each sample we used several intensities of excitation pulses and constructed resulting spectrum as envelope of obtained spectra. Same probehead was used for all three samples, hence absolute intensities should be roughly comparable. To minimize effect of frequency dependent T_2 relaxations on intensities we used only the first recorded echo in CPMG sequence for evaluation. To eliminate possibility of parasitic signals (e.g. from Co or Mn containing impurities in some part of experimental setup) we measured the spectrum without sample (but using otherwise identical setup, experiment conditions and settings) and we found no signal in this case.

The spectra consist of five lines, two broad ones centered at 300 MHz and 400 MHz, weak line at about 540 MHz and two narrow lines at 570 MHz and 575 MHz. The broad lines below 500 MHz have significantly faster transversal relaxation than the lines above 500 MHz. With increasing La and Co content the lines shift slightly to higher frequencies and change intensities: Lines at 300, 540 and 575 MHz diminish with increasing substitution content while lines

at 400 MHz and 570 MHz do not have monotonous dependence of intensities on substitution content – they reach maximal intensity in sample with $x_{\mathrm{La}} = 0.5$ and $x_{\mathrm{Co}} = 0.30$. Overall intensity of ^{59}Co resonance tends to decrease with increasing Co content. While optimal pulse intensity varies with frequency there is observable trend of its increase with Co content (optimal rf attenuation for 400 MHz signal differs by about 4 dB between $x_{\mathrm{La}} = 0.25$, $x_{\mathrm{Co}} = 0.21$ sample and $x_{\mathrm{La}} = 0.75$ and $x_{\mathrm{Co}} = 0.40$ sample).

Pieper et al. [84, 85] reported, that they observed ^{59}Co resonance in Co substituted LaSrM system in frequency range of 76–100 MHz, we tried to confirm their observation, however no NMR signal in this frequency range in our Co substituted samples was found.

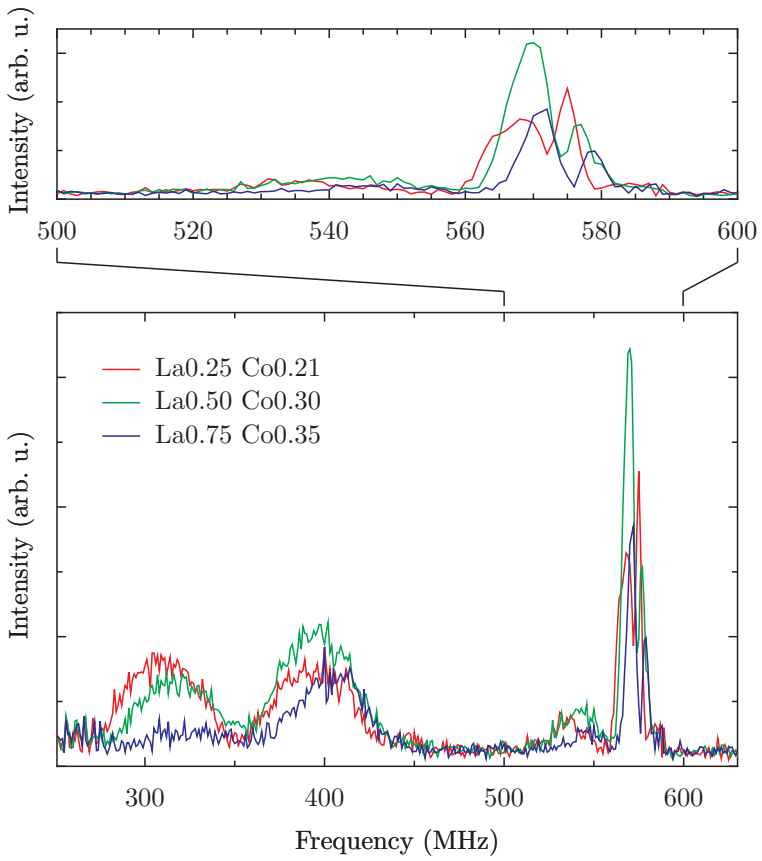

Figure 10.11: Resonance of ^{59}Co recorded at 4.2K in zero external field in Co substituted LaSrM samples using untuned broadband probehead. Bottom plot shows whole spectrum, top plot shows detail of spectrum in interval 520 − 600 MHz. Spectra are envelopes of several experiments with different pulse intensities, they are plotted in common intensity scale, no frequency corrections were applied. Only first observed echo was used in order to minimize T_2 modulation of intensities.

10.4.2 Zn substituted LaSrM

Comparison of ^{57}Fe spectra in frequency region of $12k - 4f_{\mathrm{IV}}$ resonance of LaSrM samples and Zn substituted LaSrM samples together with integral intensities of the latter is in figure 10.12. Zn substitution suppresses satellites S_1 and S_2 observed in LaSrM samples while enhancing satellites at 70.5 MHz and at 73 MHz. One can also see, that intensity of $2a$ resonance is lowered by Zn substitution.

Reduction of S_1 and S_2 intensities indicates, that Zn does significantly lower amount of ferrous ions in the system. The S_1 and S_2 satellites were attributed to $4f_{\mathrm{IV}}$ (and $12k$) sites with ferrous nn in $2a$ sites, their suppression is an expectable outcome upon lowering amount of ferrous ions originally localized in $2a$ sites.

Zinc substitution in magnetic iron oxides is generally considered to have strong preference towards tetrahedral sites [1–4], and indeed, the observed ^{57}Fe NMR spectra can be well explained using model with Zn having strong preference towards tetrahedral $4f_{\mathrm{IV}}$ sites.

Intensity of satellite at 70.5 MHz does increase as expected for sum of $12k$ satellites induced by one and two substitution atoms in nn $4f_{\mathrm{IV}}$ sites (the expected intensities are listed in table 8.5) and the satellite develops upon increasing Zn content a shoulder at lower frequencies which likely arises from $12k$ sites with two substituted nn $4f_{\mathrm{IV}}$ sites – their resonance is further away from $12k$ main line as expected from additivity hypothesis.

Lowering of observed intensity of $2a$ main line can be explained as action of nn Zn in $4f_{\mathrm{IV}}$ sublattice acting on $2a$ ferric ions (see table 8.4 for intensities of $2a$ satellites induced by $4f_{\mathrm{IV}}$ substitution). Satellites induced by Zn on $2a$ resonance draw intensity from the main line. If the satellites emerge on frequencies below 73.5 MHz they merge with $12k - 4f_{\mathrm{IV}}$ lines and the spectral region above 73.5 MHz is short of their intensity. In samples with $x_{\mathrm{La}} = 0.50,\ 0.75$ the zinc content is lower than that of La, presumably there are ferrous ions formed in $2a$ sites thus further reducing intensity of $2a$ resonance.

Satellite at 73 MHz can be interpreted as coming from either $2a$ sublattice or from $4f_{\mathrm{IV}}$ sublattice. It cannot be decided with absolute confidence, but we are strongly inclined towards it being $2a$ resonance. Zn contents are quite high and should induce satellites corresponding to nuclei with two Zn $4f_{\mathrm{IV}}$ nn, such satellites should appear further away from the main line. If the satellite was resonance of $4f_{\mathrm{IV}}$ with one Zn nn, satellite line from sites with two substituted nn should appear on higher frequencies – likely in 73–74 MHz interval – this contradicts the observation, we found no distinct resonance there. If on the other hand the satellite at 73 MHz is resonance of nuclei in $2a$ sublattice, satellite corresponding to that with two zinc nn should lie below

73 MHz, hidden under strong $12k-4f_{\mathrm{IV}}$ resonances. Further argument for the satellite being signal from $2a$ sublattice is in integral intensities of signal below 73.5 MHz and above 73.5 MHz. The Zn substitution should reduce integral intensity from $4f_{\mathrm{IV}}$ sites by x_{Zn}, if there was no $2a$ signal below 73.5 MHz (i.e. the signal there was only from $12k$ and $4f_{\mathrm{IV}}$ sites), the integral intensity in this region should be $8-x_{\mathrm{Zn}}$, while the observed intensity is above 8 in all three samples. But if the satellite is from $2a$ sublattice, the loss of signal induced by Zn substituting $4f_{\mathrm{IV}}$ ^{57}Fe is compensated by gain from $2a$ satellites induced by Zn nn. This interpretation (satellite at 73 MHz is resonance of $2a$ with nn Zn) is further supported by experiments of Štěpánková et al. [86] on Co+Ti co-substituted BaM – they reported similar satellite pattern and confirmed that the satellite is from majority spin sublattice. Satellites induced by Zn nn on $4f_{\mathrm{IV}}$ resonance are probably hidden in 70–73 MHz interval.

Resonance of $4f_{\mathrm{VI}}$ sites is not significantly altered – we observed additional broadening which hides hints of satellite structure induced by La–Sr disorder, this is also expectable – Zn in $4f_{\mathrm{IV}}$ should induce one satellite on each of the $4f_{\mathrm{VI}}$ lines, if the satellite is close to main line, overall smoothing of whole $4f_{\mathrm{VI}}$ subspectrum is not very surprising outcome.

Effect of Zn substitution on $2b$ lines is not too strong, which is to be expected – these sites have neither $4f_{\mathrm{IV}}$ nor $2a$ nearest neighbors.

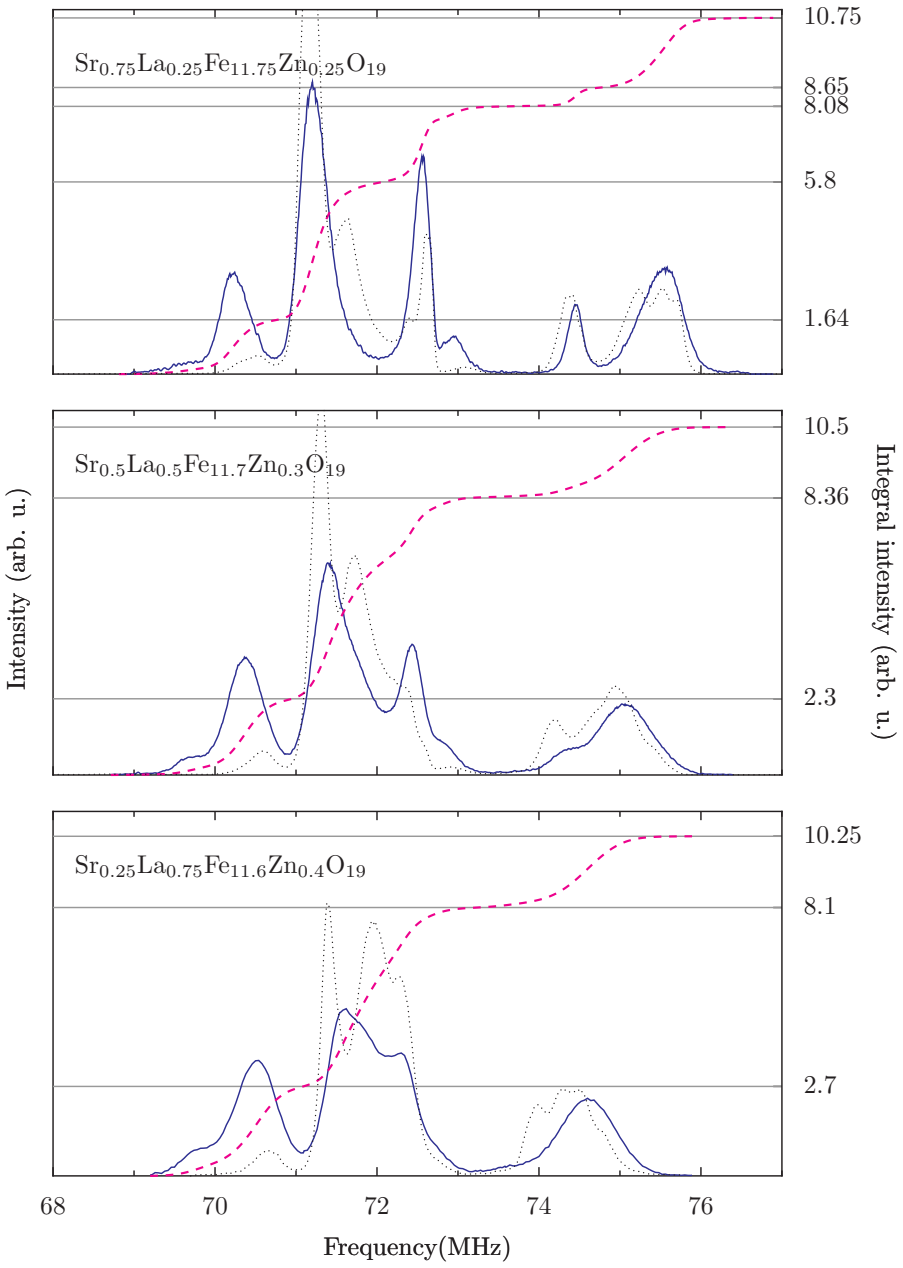

Figure 10.12: $12k - 4f_{\mathrm{VI}}$ ^{57}Fe NMR spectra of Zn substituted LaSrM samples (solid blue lines) compared to that of LaSrM samples of same La contents with no small cation substitution (dotted black lines). Integral intensities of Zn substituted samples are also shown (magenta dashed lines). Intensities are f^2 corrected and normalized to $11 - x_{\mathrm{La}}$ integral intensity.

10.4.3 Cu substituted LaSrM

In Cu substituted LaSrM samples we can take advantage of observed ^{63}Cu and ^{65}Cu NMR. The copper signal shifts to higher frequencies upon application of external magnetic field and in zero field its mean frequency decreases with increasing La content.

Provided that copper ion has same orientation of magnetic moment as iron ions in sublattice it enters, shift of its resonance in external field indicates that it enters minority spin sublattice, i.e. $4f_{\mathrm{IV}}$ or $4f_{\mathrm{VI}}$. The non-negligible shift of copper resonance to low frequencies with increasing x_{La} is in better accord with Cu entering preferentially the $4f_{\mathrm{VI}}$ sites – the $4f_{\mathrm{VI}}$ ^{57}Fe resonance experiences similar shift to low frequencies upon increase of La content. In $\mathrm{Nb}^{5+} - \mathrm{Cu}^{2+}$ substituted BaM the copper was reported to enter preferentially $4f_{\mathrm{VI}}$ sites [87], and in W and X type hexaferrites the Cu^{2+} ions were reported to enter octahedral sites in S blocks [3, 88].

The complex line profiles observed in samples with lower La contents are probably due to quadrupole splitting of ^{63}Cu and ^{65}Cu resonances. Provided, that we observed full ^{63}Cu + ^{65}Cu spectrum (i.e. spectrum is formed by all allowed transitions, as opposed to possibility that we see only central ($-1/2 \leftrightarrow 1/2$) transitions), we can estimate magnitude of quadrupole interaction. The observed splitting is at the order of 1 MHz, which is much smaller than resonance frequency, hence we can treat the quadrupole interaction as perturbation. Both ^{63}Cu and ^{65}Cu isotopes have spin 3/2, one can expect weak quadrupolar interaction to induce splitting of resonance line into three equidistant components (we assume zero asymmetry of EFG and V_{zz} parallel with magnetic field both of which is fulfilled in iron sites in M ferrite) with spacing ν_{Q} given by:

$$\nu_{\mathrm{Q}} = \frac{3eQV_{zz}}{h2I(2I-1)} \tag{10.4}$$

For $|\nu_{\mathrm{Q}}| = 1.3$ MHz and ^{63}Cu nucleus we get $|V_{zz}| \approx 10^{21}\mathrm{Vm}^{-2}$.

From resonance frequency we estimate local magnetic field on Cu nuclei to $B_{\mathrm{loc}}^{\mathrm{Cu}} \approx 5$ T, which implies magnetic moment of Cu ion about 0.5 μ_{B}.

In figure 10.13 we compare $12k - 4f_{\mathrm{VI}}$ ^{57}Fe NMR spectra of LaSrM samples with Cu substitution to that with same La content but no small cation substitution. Intensity of S_1 satellite is reduced in Cu substituted samples while that of S_2 is increased, intensities of satellites at 70.5 MHz and 73 MHz are left unchanged. Additional satellite at 68.5 MHz appears in the spectrum, its intensity is 0.34 in sample with smallest La content and about 0.6 in remaining two samples. Integral intensity of signal below 73.5 MHz ($12k + 4f_{\mathrm{IV}}$ region) is quite close to 8 in all three samples while that above 73.5 MHz decreases with increasing La content. Intensity of $2a$ main line is not suppressed by

Cu substitution (while it was in Zn substituted samples), in Cu substituted sample with smallest La content the $2a$ line is slightly stronger, than in the non-substituted one.

The effect of Cu substitution on observed ^{57}Fe NMR spectrum can be explained by Cu preferentially entering the $4f_{\mathrm{VI}}$ sublattice. Divalent copper in $4f_{\mathrm{VI}}$ sites is in accord with $12k + 4f_{\mathrm{IV}}$ profile having integral intensity equal to 8 and $2a + 4f_{\mathrm{VI}}$ having intensity $3 - x_{\mathrm{La}}$ provided that ferrous ions form again in $2a$ sublattice. In such case intensity of $2a + 4f_{\mathrm{VI}}$ signal is reduced by Cu taking place of resonant ^{57}Fe in $4f_{\mathrm{VI}}$ sites as well as by ferrous ions forming in $2a$ sites due to incomplete compensation of excess charge by divalent copper.

The satellite at 68.5 MHz most likely comes from $12k$ ^{57}Fe with one Cu nn in $4f_{\mathrm{VI}}$ site. Intensity of the satellite is quite low, compared to prediction for this situation (see table 8.7), this can be explained by the real Cu content being smaller than the nominal one. For sample with $x_{\mathrm{La}} = 0.25$ we get from intensity of the satellite $y_{\mathrm{Cu}} \approx 0.06$ and for samples with $x_{\mathrm{La}} = 0.50,\ 0.75$ we get $y_{\mathrm{Cu}} \approx 0.1$. Results of titration on $x_{\mathrm{La}} = 0.25$ sample (table 10.4) indicate much higher content of ferrous ions than expected – this complies with much smaller than nominal copper content indicated by ^{57}Fe NMR results. In samples with higher x_{La} the titration gives results resembling theoretical values, however there is still second phase detected by SEM – if the second phase is Cu–rich it may explain still quite low Cu contents inferred from ^{57}Fe NMR.

Partial suppression of S_1 satellite is likely due to smaller amount of ferrous ions in $2a$ sites which induce the satellite, reduction of S_2 intensity by the same mechanism is probably compensated by emergence of $4f_{\mathrm{IV}}$ satellite line induced by nn Cu on frequency of S_2 satellite (however we have to admit, that this mechanism cannot explain increase of S_2 intensity).

Effect of substitution in $4f_{\mathrm{VI}}$ should also be observable on $2b$ and $4f_{\mathrm{VI}}$ lines. The $2b$ line is hidden below resonance of copper, with exception of $x_{\mathrm{La}} = 0.25$ sample, where signal attributable to $2b$ ^{57}Fe NMR was observed when stronger rf pulses were applied. This signal has a tail reaching to frequencies above 62 MHz which may be interpreted as satellite induced by nn Cu, however the separation of ^{57}Fe resonance from these of ^{63}Cu and ^{65}Cu is certainly not perfect from which it emerges with imminent inevitability, that the observed tail could have origin in resonance of copper isotopes rather than in resonance in ^{57}Fe in $2b$ sites. Given the copper contents deduced from intensities of $12k$ satellite at 69 MHz the expected intensity of $4f_{\mathrm{VI}}$ satellites should be quite low (namely equal to x_{Cu}), it is then understandable, that no significant change of $4f_{\mathrm{VI}}$ resonance upon Cu substitution was observed.

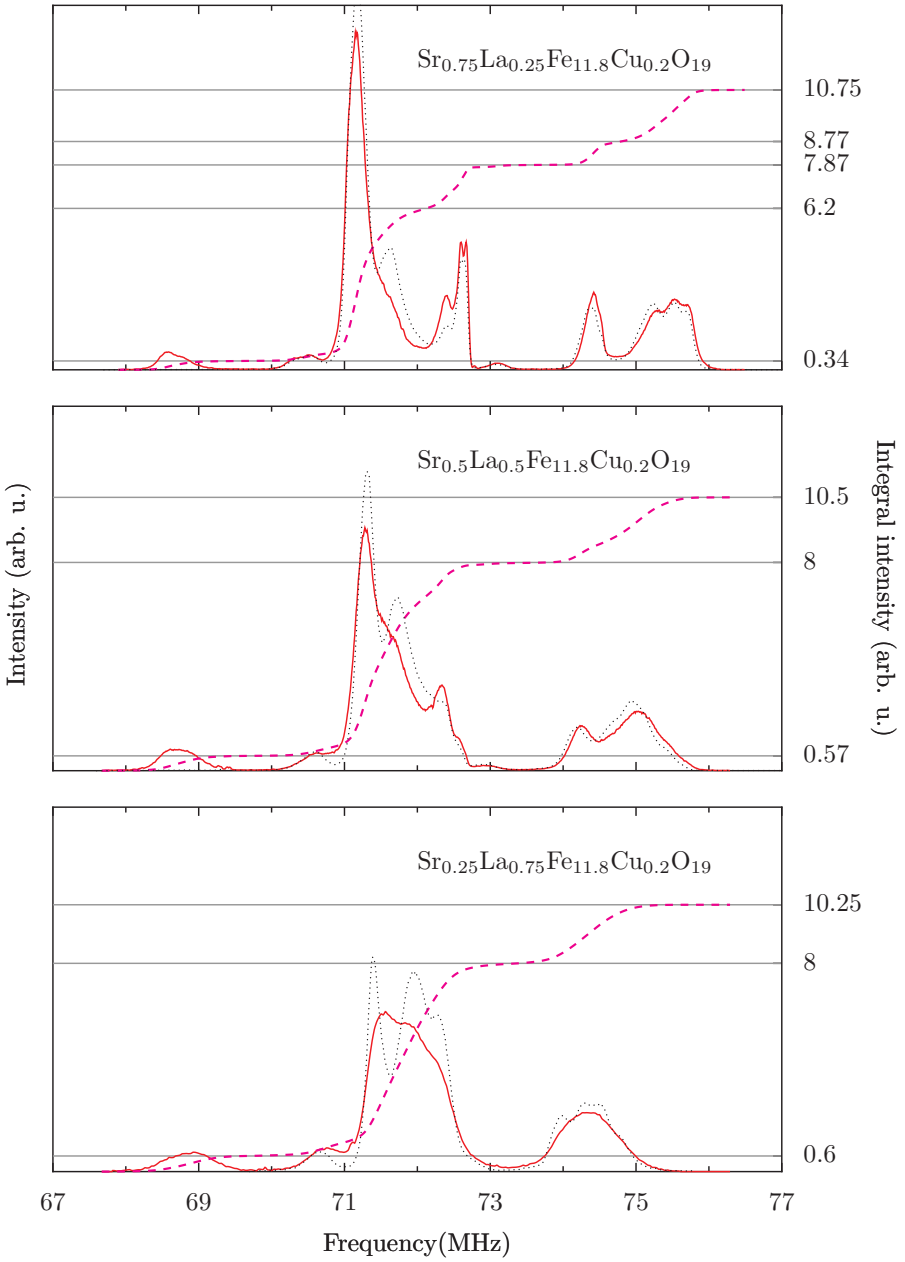

Figure 10.13: $12k - 4f_{\mathrm{VI}}$ ^{57}Fe NMR spectra of Cu substituted LaSrM samples (solid red lines) compared to that of LaSrM samples of same La contents with no small cation substitution (dotted black lines). Integral intensities of Cu substituted samples are also shown (magenta dashed lines). Intensities are f^2 corrected and normalized to $11 - x_{\mathrm{La}}$ integral intensity.

10.4.4 Co substituted LaSrM

Case of Co substituted LaSrM samples is the most intriguing one, the results cannot be explained assuming strong preference of Co towards only one site in the hexaferrite structure. Wiesinger et al. [89] used studied La–Co co-substituted SrM by Mössbauer spectroscopy and proposed preference of Co^{2+} towards octahedral $4f_{VI}$ and $2a$ sites, while Pieper et al. [84, 85] in their NMR studies proposed $4f_{IV}$ and $4f_{VI}$ sites.

As in previous subsections we compare the range of $12k - 4f_{VI}$ ^{57}Fe NMR spectra of LaSrM samples substituted by Co to these of LaSrM with no small cation substitution (figure 10.14), additionally we also compare ^{57}Fe NMR spectra of Co substituted LaSrM to these of Zn substituted LaSrM (figure 10.15).

At first glance, effect of Co substitution on ^{57}Fe resonance is quite similar to that of Zn – S_1 and S_2 satellites are suppressed, and satellites at 70.5 MHz and 73 MHz are enhanced. On the other hand $2a$ line in Co substituted $La_{0.5}Sr_{0.5}M$ is stronger than that in system substituted by same amount of Zn (central plot in figure 10.15) and at 63 MHz there is a shoulder on $2b$ line in Co substituted samples.

Suppression of S_1 and S_2 satellites implies that Co does compensate for the extra charge brought to system by La, i.e. that there are Co^{2+} ions. Overall similarity of ^{57}Fe spectra of Co and Zn substituted LaSrM suggests, that Co probably enters the $4f_{IV}$, smaller intensity of satellite at 70.5 MHz then indicates, that Co content in the $4f_{IV}$ sites is smaller than that of Zn. From intensities of the satellite we estimate Co content in $4f_{IV}$ sublattice to $x_{Co}^{4f_{IV}} \approx 0.1$ in sample with $x_{La} = 0.25$ and to $x_{Co}^{4f_{IV}} \approx 0.14$ in samples with higher La contents, i.e. about half the nominal Co contents. If reason for formation of the satellite at 70.5 MHz in non-substituted LaSrM is present also in Co substituted LaSrM samples (e.g. the satellite in LaSrM is induced by impurity in $4f_{IV}$ sites and this impurity is present also in Co substituted samples in same amounts), then estimates of Co content should be lowered to $x_{Co}^{4f_{IV}} \approx 0.07$ in sample with $x_{La} = 0.25$ and to $x_{Co}^{4f_{IV}} \approx 0.1$ in samples with higher La contents.

Shoulder on $2b$ resonance indicates, that there is some Co in sites neighboring with the $2b$, i.e. $12k$ or $4f_{VI}$. We see the $12k$ sites as more probable variant for two reasons: first the shoulder is quite weak – same amounts of substitution in $12k$ or in $4f_{VI}$ sublattice would induce weaker satellite pattern on $2b$ line in case of substitution entering the $12k$ sublattice (compare table 8.11 to 8.8, 8.9 and 8.4), second, Co in $4f_{VI}$ sublattice might induce similar satellite on $12k$ resonance as Cu does (i.e. satellite line at about 69 MHz) and no such line was found. Substitution in $12k$ sites should induce satellite lines on resonances of all five iron sublattices, however the satellites induced by ex-

pected Co contents in $12k$ sublattice (below 0.25) would in general be quite weak. It is conceivable, that they are hidden in broad profiles and manifest themselves as mere overall smoothing of ^{57}Fe spectrum.

Observed ^{59}Co NMR signal (fig 10.11) is in stark contrast to that reported by Pieper et al. [84, 85] and its overall lowering upon increasing of Co content is puzzling too. Based on comparison with work by Krishnan [90] resonance above 500 MHz should be ascribed to Co^{2+} ions while these below 500 MHz can originate in Co^{3+}. Two different dependences of ^{59}Co signal intensity on Co content (decrease with increasing y_{Co} and non-monotonic change) may be ascribable to two Co species (e.g. Co ions in two different sublattices) each of which changes its valence between Co^{2+} and Co^{3+} thus appearing in two different regions of ^{59}Co spectrum.

Overall loss of ^{59}Co signal with increase of Co content is probably result of lowering of enhancement factor with increase of La and Co content (stronger pulses were needed to excite ^{59}Co resonance in samples with higher La and Co content). Increase of magnetocrystalline anisotropy can be reason for such lowering of enhancement factor (see equation 3.13).

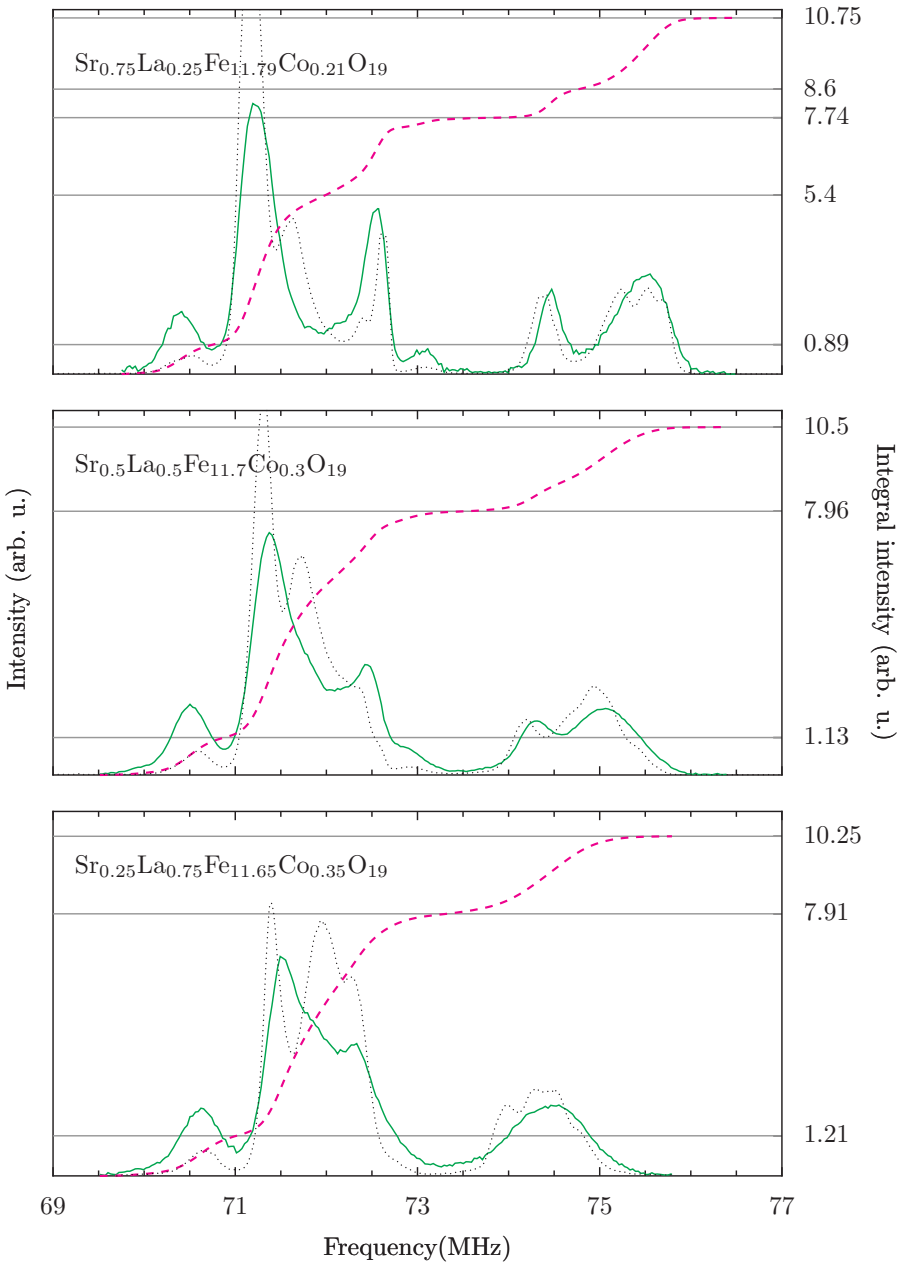

Figure 10.14: $12k - 4f_{\mathrm{VI}}$ ^{57}Fe NMR spectra of Co substituted LaSrM samples (solid green lines) compared to that of LaSrM samples of same La contents with no small cation substitution (dotted black lines). Integral intensities of Co substituted samples are also shown (magenta dashed lines). Intensities are f^2 corrected and normalized to $11 - x_{\mathrm{La}}$ integral intensity.

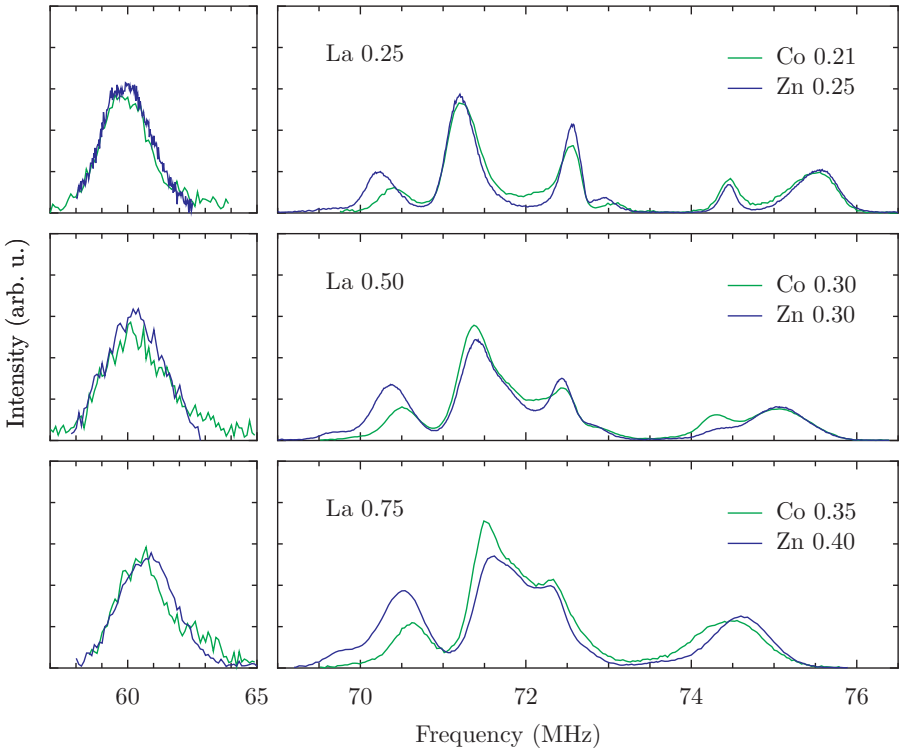

Figure 10.15: Comparison of ^{57}Fe NMR spectra of Co substituted LaSrM samples (green lines) and Zn substituted LaSrM (blue lines). Note, that in $x_{\mathrm{La}} = 0.50$ samples nominal contents of Co and Zn are identical.

10.5 Summary

Using ^{57}Fe NMR and electronic structure calculations we found that in LaSrM system trivalent La ions induce formation of ferrous ions in $2a$ sublattice and that distribution of the ferrous ions in $2a$ sublattice is static on timescale of at least 10^{-7} s. We detected ^{139}La NMR signal in LaM and have shown that it is in good accord with prediction of the calculations.

Further we studied LaSrM samples substituted by Zn, Cu and Co with intent to partially compensate for the extra charge brought in by La. ^{57}Fe spectra have shown, that Zn substitution enters $4f_{\mathrm{IV}}$ sites and does compensate the charge. ^{63}Cu and ^{65}Cu NMR together with ^{57}Fe NMR evidenced Cu in $4f_{\mathrm{VI}}$ sites in somewhat smaller amount than the nominal. In case of Co substitution ^{57}Fe spectra indicate its preference towards at least two sublattices, about third to half of Co likely enters the $4f_{\mathrm{IV}}$ sites, the rest is expected to come to $12k$ sites, however presence in Co in other sites cannot be excluded. The observed ^{59}Co spectra imply presence of Co^{2+} as well as Co^{3+}, indicating that in case of Co the charge compensation is of more complex nature.

Chapter 11

Comparison of M, W and X type hexaferrites

11.1 Introduction

In this chapter we compare results of ^{57}Fe NMR and electronic structure calculations on SrM, $SrFe_2W$ and $SrFe_2X$. We aimed on interpretation of $SrFe_2W$ and $SrFe_2X$ ^{57}Fe NMR spectra and question of localization of ferrous ions in these structures.

We studied powder samples of SrM, $SrFe_2W$ and $SrFe_2X$ prepared by J. Töpfer from University of Applied Sciences Jena using standard ceramic process. We recorded ^{57}Fe NMR spectra of all samples at 4.2 K in zero external field and compared the observed profiles to predictions of electronic structures calculations.

Structures of M, W and X type hexaferrites are quite related as they correspond to different stacking orders of R and S blocks, also all three types are uniaxial collinear magnets with easy axis parallel with hexagonal axis of crystal structure. Due to this one can match sites in different types on basis of similar surroundings. Such comparison is useful in interpretation of ^{57}Fe NMR spectra as the resonance frequency is dependent on local environment of nucleus. Review of sites in these hexaferrite types is in table 2.1 in chapter 2, where also similarities of particular sites in M, W and X structures are accented.

11.2 NMR Spectra

^{57}Fe NMR spectra of all three samples are plotted in figure 11.1. The M type ferrite shows the five well resolved narrow resonance lines which have been

ascribed to corresponding sublattices.

The W type shows spectrum of more complex profile, again there is one line at 59.5 MHz and one just below 76 MHz, but between 70–74 MHz there is partially resolved profile apparently composed of several overlapping lines. Most intensity is found around 71 MHz. There are three other peaks at 71.2 MHz, 72 MHz and 73.3 MHz.

Spectrum of the X type can be qualitatively viewed as combination of the previous two, it has sharp resonance lines at frequencies of M type resonance lines and beneath them there is broadened profile quite similar to that observed on W type. Widths of sharp narrow resonance lines in its spectrum are similar to these of SrM lines.

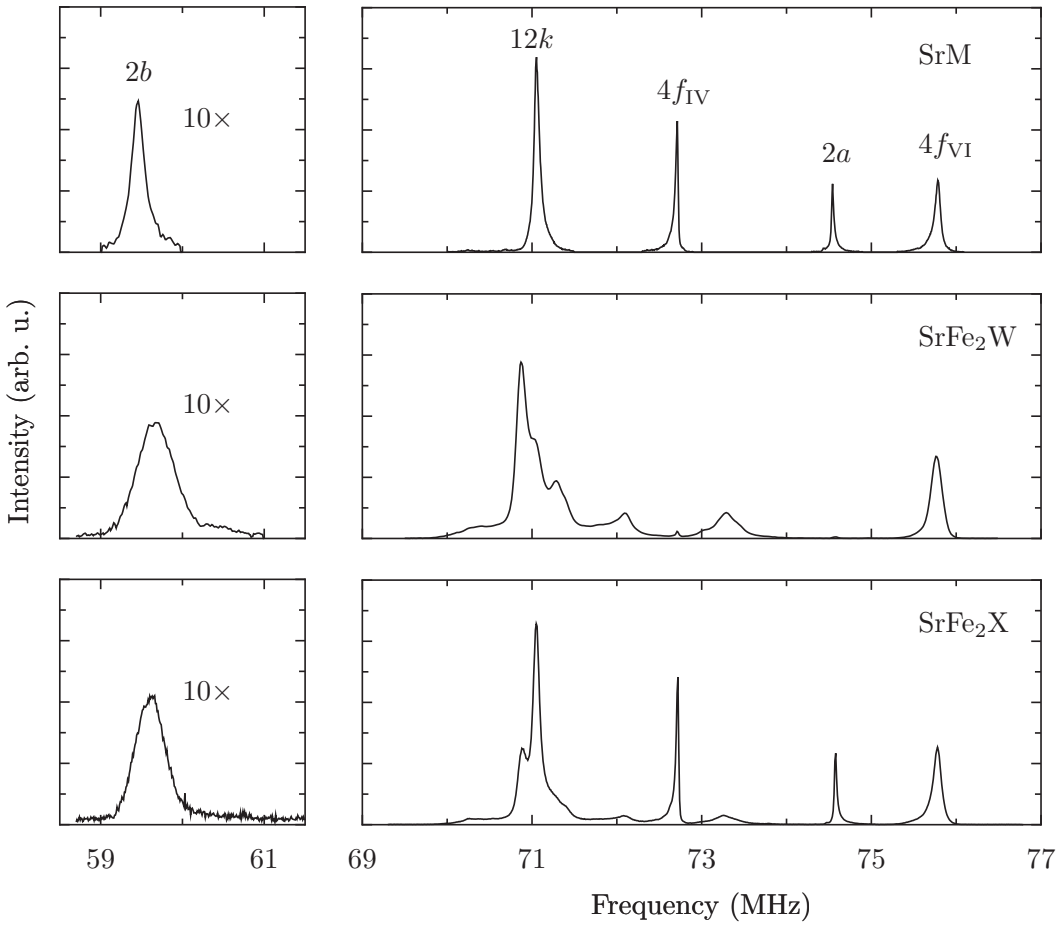

Figure 11.1: Spectra of (top to bottom) SrM, $SrFe_2W$ and $SrFe_2X$ hexaferrite powders recorded at 4.2 K in zero external field. Intensities are f^2 corrected. Intensities of low-frequency lines are multiplied by factor 10 in order to be well visible in common scale plot.

11.3 Electronic Structure Calculations

From calculations of electronic structures of SrM, $SrFe_2W$ and $SrFe_2X$ we extracted local magnetic fields on iron sites, valences of iron ions and their spin magnetic moments. The local fields are given in tables 11.1, 11.2 and 11.3, magnetic moments and valences are in tables 11.4, 11.5 and 11.6.

In tables 11.1, 11.2 and 11.3 the local field has been broken up into several contributions. The two contributions to contact field (from $3d$ and $4s$ moments) calculated using the semi-empirical correction performed according to [52] are shown separately. The contact contribution calculated from $3d$ mo-

ment many be viewed as on-site, while that of $4s$ electrons, which are affected mainly by neighbors of the particular ion, as transferred. Next there are orbital and dipolar contributions. The orbital contribution is induced by motion of electrons, and the dipolar contribution corresponds to field generated by magnetic dipole moments of electrons. All these contributions are calculated from electron density inside particular atomic sphere and together constitute the hyperfine field. Finally there is contribution of other magnetic ions – sum of their dipolar fields on the particular site.

If a ion acquires ferrous rather than ferric character magnitudes of its local components field are affected. As extra $3d$ charge is added, orbital and (or) dipolar contributions tend to increase. In ferric ion the $3d$ electron density has nearly spherical symmetry, thus allowing only quite small orbital and dipolar components of hyperfine field. Upon addition of extra charge (transition to ferrous ion) the $3d$ density looses the symmetry and the orbital and dipolar components can grow significantly. Apart from this one can also use the calculated valences and magnetic moments to identify ferrous-like ions in the same way as was discussed in chapter 10.

In SrM all ions should have ferrous character and indeed their calculated valences are close to three and there is no site with significantly lowered magnetic moment (table 11.4). Orbital and dipolar contributions to local field are below 1 T except for dipolar contribution on $2b$ bipyramidal site.

In $SrFe_2W$ (tables 11.2 and 11.5) one can see substantial orbital or dipolar contributions to local field on $4f_{VI}$ sites in SS block and on $6g$ sites in between adjacent S blocks, furthermore calculated valence and moment of $4f_{VI}$ sites in SS are lowered in comparison to the rest. This indicates localization of extra charge in these sites. In case of ferrous ions in $SrFe_2W$ are the main suspects the $9c_{VI}$ sites, which are located in between adjacent S blocs (these sites are analogous to $6g$ in W structure).

SrM site	block	local field (T) contact field $4s$	$3d$	other contributions orb.	dip.	latt.	total	freq. (MHz)
$4f_{\mathrm{VI}}$	R	−11.80	68.79	−0.54	0.01	−0.56	55.89	77.21
$2b$	R	19.66	−67.50	0.86	2.41	0.90	−43.66	60.33
$2a$	S	14.50	−69.55	0.53	−0.07	1.08	−53.51	73.92
$4f_{\mathrm{IV}}$	S	−12.29	67.25	−0.73	0.03	0.02	54.18	74.85
$12k$	R–S	18.19	−69.31	0.59	0.39	−0.49	−50.63	96.94

Table 11.1: Calculated local fields on iron sites in SrM and ^{57}Fe resonance frequencies corresponding to total local field. Contributions to the local field are shown as well. Contact field is further broken up into contributions of $3d$ electrons and $4s$ electrons (see equation 5.1). Field generated by orbital motion of electrons is shown in column orb. and dipole field of electron spins in column dip. All so far mentioned contributions come from within atomic sphere only and together form the hyperfine field, the latt. contribution is sum of dipolar fields generated on the particular site by other ions.

$SrFe_2W$ site	block	local field (T) contact field $4s$	$3d$	other contributions orb.	dip.	latt.	total	freq. (MHz)
$4f_{\mathrm{VI}}$	R	−12.54	69.64	−0.48	0.01	−0.57	56.07	77.46
$2d$	R	20.65	−68.32	0.83	2.38	0.90	−43.56	60.19
$4f_{\mathrm{VI}}$	SS	14.75	−66.90	0.37	−6.44	1.09	−57.13	78.93
$4e$	SS	−15.49	67.99	−0.62	0.23	0.01	52.12	72.01
$4f_{\mathrm{IV}}$	SS	−16.22	68.05	−0.70	−0.44	0.00	50.68	70.02
$12k$	R–SS	18.44	−69.91	0.56	0.41	−0.48	−50.99	70.45
$6g$	S–S	14.01	−66.81	7.76	−1.10	−0.39	−46.53	64.28

Table 11.2: Calculated local fields on iron sites in $SrFe_2W$ and ^{57}Fe resonance frequencies corresponding to total local field. Contributions to the local field are shown as well. Contact field is further broken up into contributions of $3d$ electrons and $4s$ electrons (see equation 5.1). Field generated by orbital motion of electrons is shown in column orb. and dipole field of electron spins in column dip. All so far mentioned contributions come from within atomic sphere only and together form the hyperfine field, the latt. contribution is sum of dipolar fields generated on the particular site by other ions.

$SrFe_2X$		local field (T)						freq.
site	block	contact field		other contributions			total	(MHz)
		$4s$	$3d$	orb.	dip.	latt.		
$3b_{VI}$	S	15.24	−70.25	0.48	−0.07	1.07	−53.53	73.96
$6c_{IV}$	S	−13.76	68.14	−0.65	−0.03	−0.02	53.68	74.16
$6c_{VI}$	R	−13.52	69.59	−0.48	0.04	−0.56	55.07	76.08
$6c^*_{VI}$	R	−13.52	69.59	−0.48	0.04	−0.56	55.07	76.08
$6c_V$	R	21.14	−68.35	0.81	2.38	0.88	−43.14	59.60
$6c_{VI}$	SS	16.47	−70.01	−0.60	0.35	1.07	−52.72	72.84
$6c_{IV}$	SS	−14.75	68.06	−0.61	0.10	0.04	52.85	73.01
$6c^*_{IV}$	SS	−13.76	68.15	−0.64	0.19	−0.01	53.93	74.51
$18h_{VI}$	R–S	19.91	−70.17	0.54	0.27	−0.48	−49.92	68.97
$18h^*_{VI}$	R–SS	19.91	−70.14	0.57	0.30	−0.51	−49.86	68.89
$9c_{VI}$	S–S	14.75	−64.55	8.49	8.03	−0.43	−33.71	46.57

Table 11.3: Calculated local fields on iron sites in $SrFe_2X$ and ^{57}Fe resonance frequencies corresponding to total local field. Contributions to the total local field are shown as well. Contact field is further broken up into contributions of $3d$ electrons and $4s$ electrons (see equation 5.1). Field generated by orbital motion of electrons is shown in column orb. and dipole field of electron spins in column dip. All so far mentioned contributions come from within atomic sphere only and together form the hyperfine field, the latt. contribution is sum of dipolar fields generated on the particular site by other ions.

site	block	valence	moment
$4f_{VI}$	R	3.01	−4.143
$2b$	R	2.86	4.117
$2a$	S	2.99	4.200
$4f_{IV}$	S	2.88	−4.111
$12k$	R–S	2.96	4.199

Table 11.4: Valences and magnetic moments calculated by AIM for iron ions in SrM. Valences have been rescaled to nominal values as described in chapter 5.

site	block	valence	moment
$4f_{\mathrm{VI}}$	R	2.99	−4.191
$2d$	R	2.85	4.112
$4f_{\mathrm{VI}}$	SS	2.55	3.870
$4e$	SS	2.86	−4.097
$4f_{\mathrm{IV}}$	SS	2.85	−4.103
$12k$	R–SS	2.94	4.199
$6g$	S–S	2.79	4.096

Table 11.5: Valences and magnetic moments calculated by AIM for iron ions in $SrFe_2W$. Valences have been rescaled to nominal values as described in chapter 5.

site	block	valence	moment
$3b_{\mathrm{VI}}$	S	2.97	4.243
$6c_{\mathrm{IV}}$	S	2.89	−4.161
$6c_{\mathrm{VI}}$	R	3.00	−4.191
$6c^*_{\mathrm{VI}}$	R	3.00	−4.191
$6c_{\mathrm{V}}$	R	2.87	4.161
$6c_{VI}$	SS	2.94	4.227
$6c_{\mathrm{IV}}$	SS	2.87	−4.157
$6c^*_{\mathrm{IV}}$	SS	2.88	−4.161
$18h_{\mathrm{VI}}$	R–S	2.95	4.245
$18h^*_{\mathrm{VI}}$	R–SS	2.94	4.244
$9c_{\mathrm{VI}}$	S–S	2.53	3.913

Table 11.6: Valences and magnetic moments calculated by AIM for iron ions in $SrFe_2X$. Valences have been rescaled to nominal values as described in chapter 5.

11.4 Line assignment

For line assignment we used comparison of M, W and X structures and spectra, experiments on $BaFe_2W$ single crystal reported by Štěpánková et al. [91] and electronic structure calculations. In order to asses integral intensities of resonance lines we constructed spectra out of first ten recorded echoes (to minimize T_2 modulation) and plotted them together with their integral intensities in figures 11.2 and 11.3, again we used normalization which gives unit integral intensity per ferric ion in formula unit. Crystallographic positions of small cations in studied structures were summarized in table 2.1 in chapter 2.

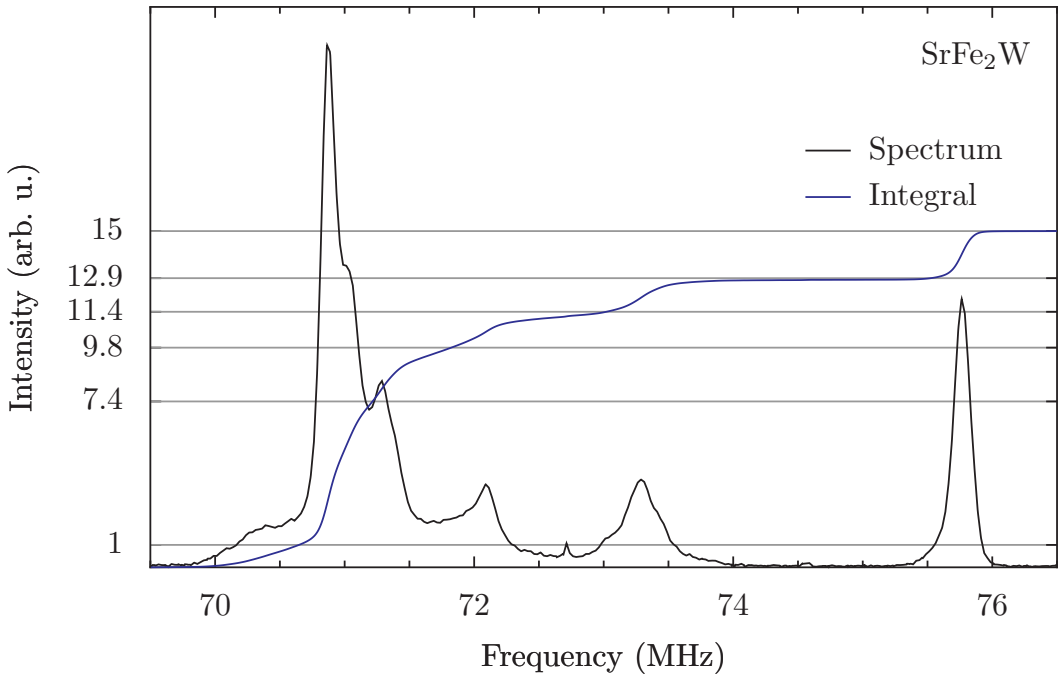

Figure 11.2: $SrFe_2W$ spectrum constructed of first ten echoes in CPMG sequence and its integral. The spectrum is f^2 corrected, integral intensity is normalized to number of ferric ions per formula unit expected resonate in shown frequency interval.

In following text we will discuss resonance of ^{57}Fe nuclei in individual sites in W and X structures. Resulting line assignment together with calculated positions of resonance lines is summarized in figure 11.4 for $SrFe_2W$ and in figure 11.5 for $SrFe_2X$.

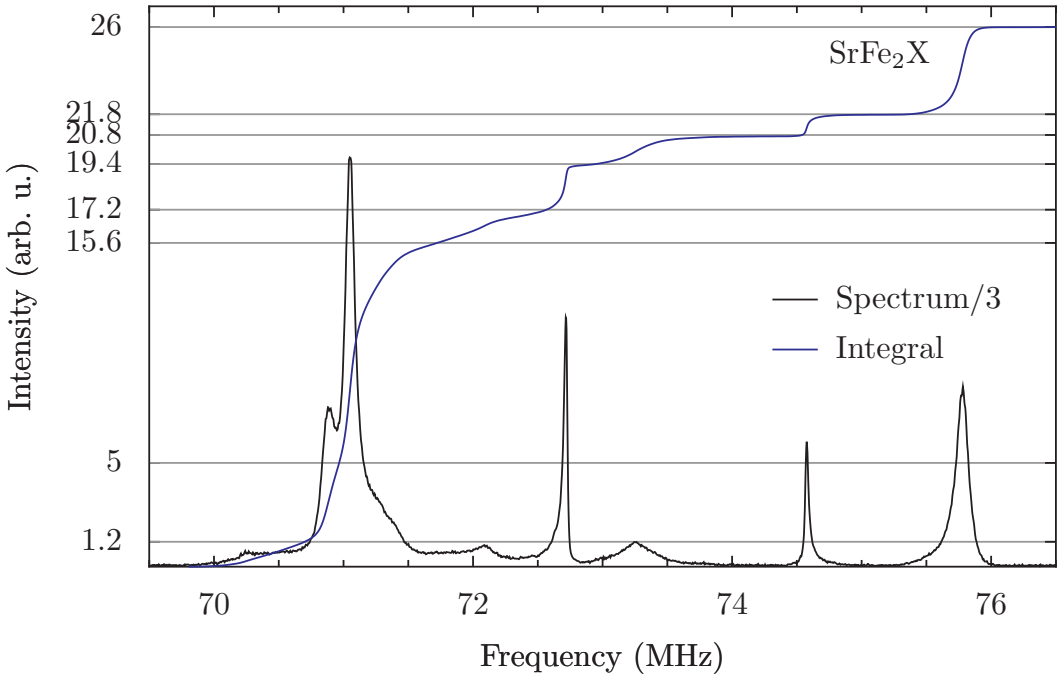

Figure 11.3: $SrFe_2X$ spectrum constructed of first ten echoes in CPMG sequence and its integral. The spectrum is f^2 corrected, integral intensity is normalized to number of ferric ions per formula unit expected resonate in shown frequency interval.

11.4.1 Sites in R blocks

We start with sites located inside R blocks. In W structure these are octahedral $4f_{VI}$ and bipyramidal $2d$, while in X structure there are octahedral $6c_{VI}$ and $6c^*_{VI}$ and bipyramidal $6c_V$. When comparing stacking sequences of M, W and X structures one notes, that in all three structures nearest neighbor block of a R block is always a S block, until next nearest neighbor block is reached, there is no substantial difference between these three structures.

The similarity of R block environments throughout the structures suggests that corresponding sites in these blocks may have quite similar resonance frequencies in all three investigated hexaferrite types. Indeed, in spectra of $SrFe_2W$ as well as of $SrFe_2X$ there are lines with resonance frequencies close to these of bipyramidal $2b$ (59.5 MHz) and octahedral $4f_{VI}$ (75.8 MHz) in SrM (see figure 11.1). Integral intensities of lines at 75.8 MHz correspond well to multiplicities of octahedral R block sites in W and X structures. Analogous interpretation of $BaFe_2W$ ^{57}Fe NMR spectrum was proposed in literature and

supported by experiments in external magnetic fields [91]. In case of $SrFe_2X$ resonance frequencies of the two inequivalent octahedral sites most likely coincide as their equivalency is lost due to difference of next nearest neighbor blocks – closer surroundings of these sites are quite similar.

Electronic structure calculations predicted R site ^{57}Fe resonance in $SrFe_2W$ at 77.45 MHz for $4f_{VI}$ site and 60.19 MHz $2d$ site (see table 11.2). Prediction for $2d$ site is in excellent agreement with observed resonance frequency and in case of $4f_{VI}$ site it is reasonably close too. Calculations of resonance frequencies $SrFe_2X$ (table 11.3) give even better match to observed frequencies. It is interesting to note, that calculations predict (within first four digits) identical resonance frequencies as well as individual components of local fields for $6c_{VI}$ and $6c^*_{VI}$ sites in R block of $SrFe_2X$.

11.4.2 Sites shared by adjacent blocks

Next we discuss sites shared by two adjacent blocks, these are (all octahedral): $12k$ in M structure (at 71.1 MHz), $12k$ and $6g$ in W and $18h$, $18h^*$ and $9c$ in X. Due to their high mutiplicities, these sites should generate very strong signals – their contribution is most likely in frequency range $70 - 71.5$ MHz of $SrFe_2W$ and $SrFe_2X$ spectra. Experiments on single crystals in external field have shown [91], that large portion of signal in this frequency range comes from sites with majority spin orientation.

In $SrFe_2X$ spectrum, there is narrow peak at 71 MHz, frequency of which coincides with $12k$ resonance in SrM and which is missing in $SrFe_2W$. Most likely this signal comes from $18h_{VI}$ sites shared by R and single S block in X structure.

The calculations also put resonance frequencies of these "interblock" sites close to $70 - 71.5$ MHz frequency range. Exceptions are sites shared by two adjacent S blocks ($6g$ in W and $9c$ in X). Predicted resonance frequencies for these sites are far too low. This is probably due to extra electrons partly localizing on thsse sites – the semiempirical correction [52] used for calculation of local fields is tailored for ferric ions and apparently fails as soon as there is substantial extra charge on the ion (similar discrepancy between calculation and experiment is seen on results on $4f_{VI}$ (SS) sites in $SrFe_2W$ which also have hint of ferrous character in calculations).

11.4.3 Sites in S blocks

Last are resonances from S blocks. In M type there are octahedral $2a$ sites (74.6 MHz) and tetrahedral $4f_{IV}$ (72.7 MHz). In W structure there are octahedral $4f_{VI}$ and tetrahedral $4e$ and $4f_{IV}$. In X structure we have ocatahedral

$3b_{\mathrm{VI}}$ (in single S block) and $6c_{\mathrm{VI}}$ (SS block pair) together with tetrahedral $6c_{\mathrm{IV}}$ in single S block and $6c_{\mathrm{IV}}$ with $6c^*_{\mathrm{IV}}$ in SS block pair.

When comparing the spectra, one can see that $SrFe_2X$ has two narrow resonance lines located on frequencies of S block sites in SrM. Integral intensities of these narrow lines correspond nicely to multiplicities of $3b_{\mathrm{VI}}$ and $6c_{\mathrm{IV}}$ sites located in single S block in X structure. Therefore we assign these narrow lines to $3b_{\mathrm{VI}}$ and $6c_{\mathrm{IV}}$ sites. Calculations put resonance frequencies of $3b_{\mathrm{VI}}$ and $6c_{\mathrm{IV}}$ sites is $SrFe_2X$ close to 74MHz which is in reasonable agreement with observed frequencies of the narrow lines.

The pair of S blocks contains three types of sites (one octahedral and two tetrahedral) in both X and W structures (we disregard the $6g$ and $9c$ sites discussed above).

The broad resonance at 73.3 MHz is known to have majority spin orientation in $BaFe_2W$ [91] and should correspond to octahedral site inside S block adjacent to another S block ($4f_{\mathrm{VI}}$ in W and $6c_{\mathrm{VI}}$ in X). Electronic structure calculations agree nicely with this interpretation of broad resonance at 73.3 MHz in case of $SrFe_2X$. In $SrFe_2W$ predicted resonance frequency of $4f_{\mathrm{VI}}$ in SS block pair is off by almost 6 MHz. Reason is probably electron localization on $4f_{\mathrm{VI}}$ (SS) sites in $SrFe_2W$ calculation.

The tetrahedral sites are known to resonate between $70 - 72$ MHz in $BaFe_2W$ [91]. Based on calculation results we suggest that resonance at 72 MHz in $SrFe_2W$ is interpreted as coming from $4e$ site. The $4f_{\mathrm{IV}}$ resonance in $SrFe_2W$ should then be at slightly lower frequency, overlapped with resonances of octahedral sites between adjacent blocks.

The tetrahedral sites in SS block pairs in X structure ($6c_{\mathrm{IV}}$ and $6c^*_{\mathrm{IV}}$) are analogous to $4e$ and $4f_{\mathrm{IV}}$ in W structure. The broadened line at 72.1 MHz is likely to come from these sites, rest of their resonance is probably hidden within spectral profile in 70–73 MHz range.

11.4.4 Defects

It is worth noting, that in $SrFe_2W$ spectrum there are small narrow peaks on frequencies corresponding to SrM lines $4f_{\mathrm{IV}}$ and $2a$ and a kink on frequency of SrM $12k$ resonance. These may be interpreted as coming either from inclusions of M phase or (more likely) from stacking faults. Based on intensities of the peaks we estimated molar fraction of sample corresponding to these defects to be about 0.7% suggesting high sample quality.

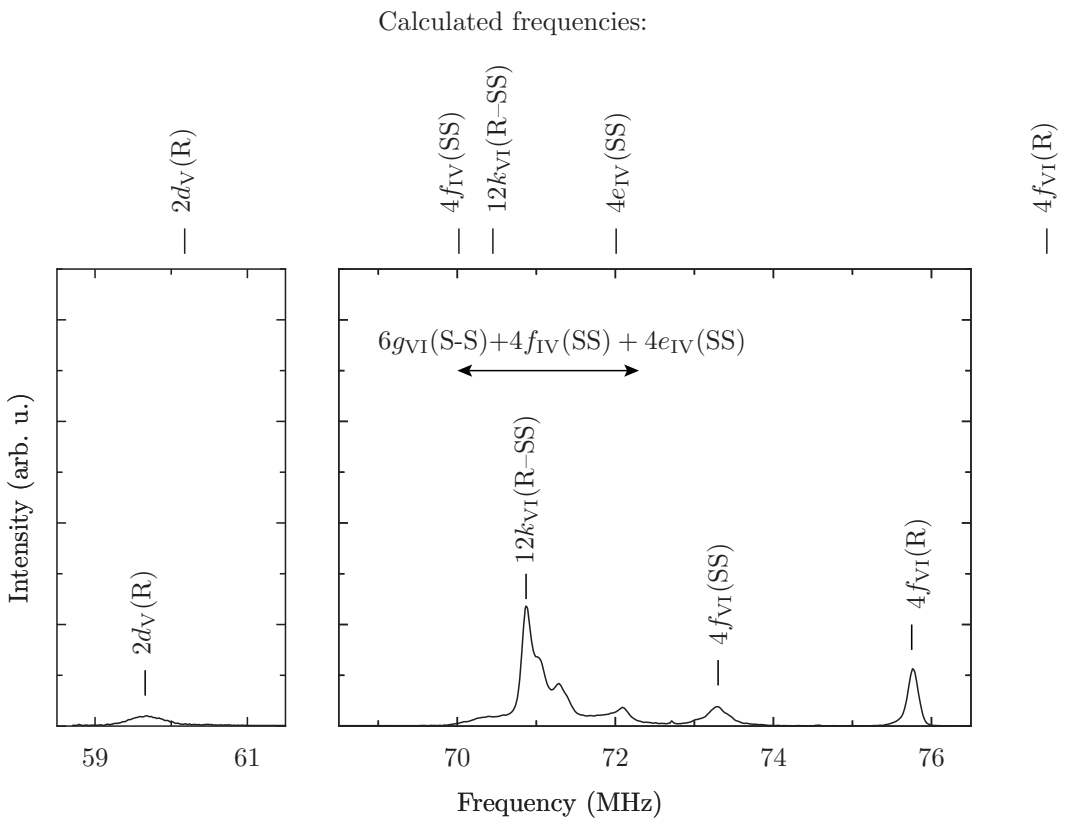

Figure 11.4: Proposed interpretation of experimental $SrFe_2W$ ^{57}Fe NMR spectrum together with resonance line positions obtained from calculations (marks above the plot frames). Calculated frequencies for $4f_{\mathrm{VI}}$(SS) and $6g$(S–S) sites are not shown as they are out of plot range (they are predicted to resonate at 78.93 MHz and 64.28 MHz respectively).

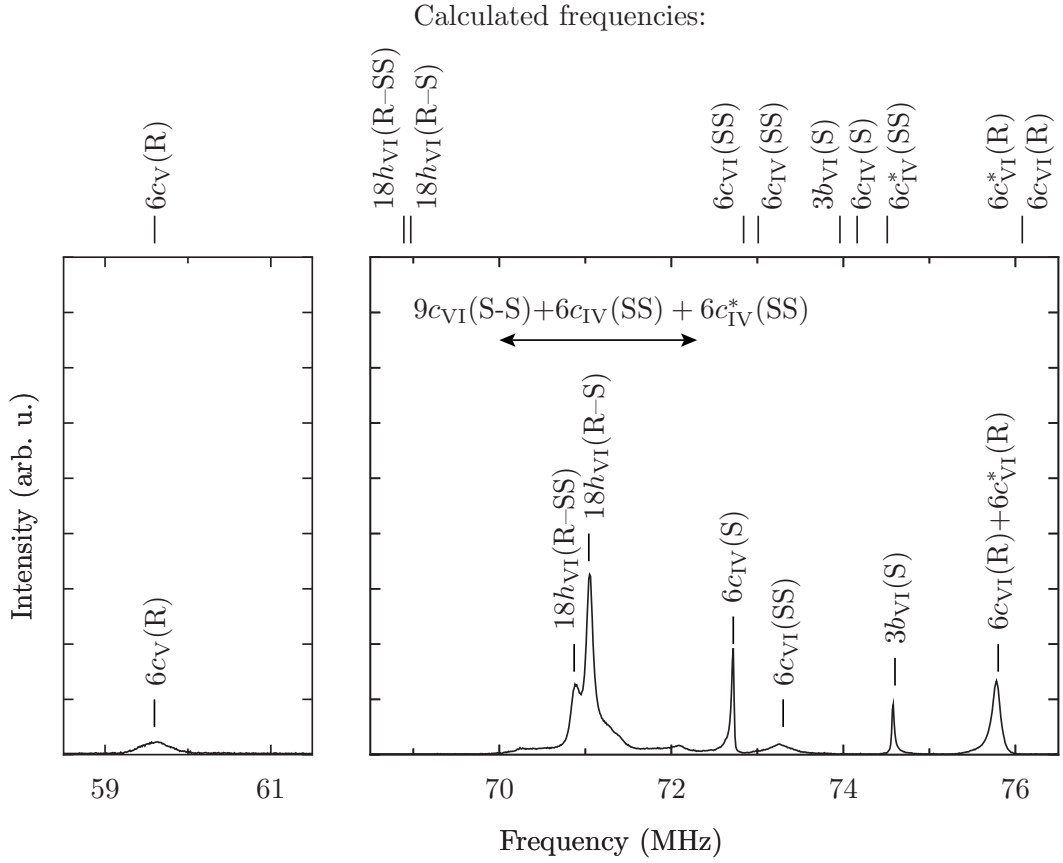

Figure 11.5: Proposed interpretation of experimental $SrFe_2X$ ^{57}Fe NMR spectrum together with resonance line positions obtained from calculations (marks above the plot frames). Calculated frequency for $9c$ position is not shown as it is well out of plot range (at 46.57 MHz).

11.5 Electron localization

Experimental indications (in ^{57}Fe NMR experiment) of electron localizing on a particular iron site are enhancement of relaxation of its signal, line broadening and reduction of integral intensity. Similar effects can be observed on neighbor sites as well. In addition to this we again used results of electronic structure calculations, where, apart from lowering calculated valences, electron partly localizing on a particular iron atom lowers its magnetic moment and increases orbital and dipolar contribution to local field.

The extra electrons in $SrFe_2W$ $SrFe_2X$ systems are believed to localize in octahedral sites of the SS block pairs [3]. Our results do agree with this. In our spectra, lines interpreted as signals from SS pair (including the octahedral sites shared by adjacent S block) appear to be quite broadened and show slightly faster T_2 relaxation.

Integral intensity of $4f_{\mathrm{VI}}$ site in SS pair in $SrFe_2W$ is 1.5, that of $6c_{\mathrm{VI}}$ in SS pair of $SrFe_2X$ is 1.4, while if the sites were occupied by ferric ions, their resonances should have integral intensities close to 2. Resonances of $6g$ and $9c$ sites are overlapped with others, hence we cannot obtain their integral intensities directly, however integral intensity in $69.5 - 74$MHz interval is 12.9 for $SrFe_2W$ and 20.8 for $SrFe_2X$ while if all sites resonating in this range were occupied by ferric ions only, the integral intensities should have been 15 and 23.

Electronic structure calculations also indicate electron localization in octahedral sites in SS block pair. Sites $4f_{\mathrm{VI}}$ and $6g$ in $SrFe_2W$ have unusually strong dipolar or orbital contribution to local field and calculated valence as well as magnetic moment of $4f_{\mathrm{VI}}$ site is considerably lower than of other sites. In $SrFe_2X$ calculations point towards $9c_{\mathrm{VI}}$ site, which has strong orbital and dipolar component of local field as well as low calculated valence and magnetic moment.

Similarly to LaSrM one can see tendency towards charge localization in octahedral sites inside S blocks, the only difference (or rather extension of the observation) is that in $SrFe_2X$ SS block pairs (absent in LaSrM) are obviously preferred over solitary S blocks (absent in $SrFe_2W$). Question remains whether preference of ferrous ion localization within SS block pair is the same in $SrFe_2W$ and $SrFe_2X$ or whether there is a difference between these two hexaferrite types. The calculations indicate slightly different scenarios (in $SrFe_2W$ both types of octahedral sites inside SS pair have ferrous character, while in $SrFe_2X$ only the sites in between the adjacent S blocks are ferrous), however experimental spectra do not exactly support this – the broad component in 70–73 MHz range is of very similar shape in both hexaferrite types thus implying that similar patterns of ferrous ions are formed in SS pairs of $SrFe_2W$ and $SrFe_2X$.

11.6 Summary

We observed experimental ^{57}Fe NMR spectra of SrM, $SrFe_2W$ and $SrFe_2X$ hexaferrites and confronted them with results of electronic structure calculations. Based on comparison of spectra, similarities between M, W and X structures and calculation results we proposed interpretations of $SrFe_2W$ and $SrFe_2X$ spectra. Further we discussed localization of ferrous ions in $SrFe_2W$ and $SrFe_2X$ systems, calculations and experiments indicate, that in both systems are the ferrous ions located in ocatehedral sites within SS blocks.

Chapter 12

Conclusions

We studied hexaferrite systems of M, W, X and Y structure types by means of ^{57}Fe, ^{59}Co,^{63}Cu + ^{65}Cu, ^{67}Zn and ^{139}La NMR, electronic structure calculations and magnetoelectric experiments. We assessed how is local structure of studied materials influenced by doping, particle size, thermal treatment and sample position in parent crystal.

In NMR experiments we were able to achieve high sensitivity which allowed us to to obtain good quality ^{57}Fe spectra of sub-miligram amounts of non-enriched samples (330 μm spheres, thin layers). Combination of electronic structure calculation with NMR has proven to be quite fruitful, calculations unquestionably significantly improved our capability to interpret the experimental NMR spectra and provided independent view on phenomenon of charge localization. The magnetoelectric experiments allowed us to study electrical polarization induced by non-collinear magnetic order.

The main obtained results can be summarized as follows:

- We observed pronounced effect of demagnetizing fields on ^{57}Fe spectra of SrM oriented thin films and submicron BaM particles. In smallest particles (16 nm diameter) significant fast-relaxing spectral component corresponding to resonance of surface layer was identified. This component is overall broadened and has tail reaching to low frequencies indicating smaller mean magnetic moments of ions in surface layer.

- In magnetoelectric $Ba_{0.5}Sr_{1.5}Zn_2Y$ hexaferrites we found that annealing markedly improves temperature range in which ME behavior can be observed while somewhat lowering maximum polarization observed at 4.2 K. The ^{67}Zn and ^{57}Fe NMR have not shown significant change of microstructure upon annealing (namely the Zn distribution was not found to be observably altered).

- In Sc doped BaM spheres we found ^{57}Fe NMR spectra and relaxations independent on position of sample in parent crystal prepared by TSSG technique indicating that Sc content as well as that of possible impurity is homogeneous in the crystal. We observed significant enhancement of T_1 relaxation by addition of Sc while observed T_2 was near its theoretical maximum for given T_1. Based on analysis of spectra we proposed, that Sc enters mainly $2b$ and $4f_{\mathrm{VI}}$ sublattices.

- We identified that in LaSrM system the extra charge brought in by La^{3+} is localized on $2a$ sites within full range of La content and that its distribution is static on timescale of at least 0.1 μs. This experimental observation is in accord with results of electronic structure calculations of LaM. We also proposed novel interpretation of ^{57}Fe NMR spectrum of LaM. In LaSrM samples co-substituted by Zn, Cu and Co we identified that Zn enters tetrahedral $4f_{\mathrm{IV}}$ sites and does well compensate the effect of La, Cu enters octahedral $4f_{\mathrm{VI}}$ sites in smaller than nominal concentrations, and that Co likely enters $4f_{\mathrm{IV}}$ sites as well as $12k$ sites. ^{59}Co NMR spectra indicated presence of divalent as well as trivalent Co in the Co co-substituted samples.

- Finally we observed ^{57}Fe spectra of $SrFe_2W$ and $SrFe_2X$ and based on comparison with spectrum of SrM and results of electronic structure calculations were able to partially interpret the observed ^{57}Fe NMR patterns. Further we propose that ferrous ions in $SrFe_2W$ and $SrFe_2X$ form in octahedral sites inside pairs of adjacent S blocks.

These results are useful within scope of basic research (preference sites for substitution atoms, localization of ferrous ions, interpretation of LaM, $SrFe_2W$ and $SrFe_2X$ ^{57}Fe spectra) as well as from application point (homogeneity of dopant content in BaM spheres, effect of annealing on ME properties of $Ba_{0.5}Sr_{1.5}Zn_2Y$).

Bibliography

[1] Kojima H. *Ferromagnetic materials. A handbook of the properties of magnetically ordered substances Volume 3 (ed. Wohlfarth E.P.).* North Holland Publ. Comp., Amsterdam, 1982. Chapter 5.

[2] Sugimoto M. *Ferromagnetic materials. A handbook of the properties of magnetically ordered substances Volume 3 (ed. Wohlfarth E.P.).* North Holland Publ. Comp., Amsterdam, 1982. Chapter 6.

[3] E Pollert. *Progress in Crystal Growth and Characterization of Materials*, 11(3):155–205, 1985.

[4] S. Krupička. *Fyzika feritů a příbuzných magnetických kysličníků.* Academia, Praha, 1969.

[5] T Kimura. In Langer, JS, editor, *Annual Review of Condensed Matter Physics, Vol 3*, pages 93–110. Annual Reviews, 4139 el Camino way, po box 10139, Palo Alto, CA 94303-0897 USA, 2012.

[6] Robert C. Pullar. *Progress in Materials Science*, 57(7):1191–1334, 2012.

[7] A Kokalj. *Computational Materials Science*, 28(2):155–168, 2003.

[8] G Albanese, A Deriu, and D Cabrini. *Hyperfine Interactions*, 70(1-4):1087–1090, 1992.

[9] Michaela Küpferling, Roland Grössinger, Martin W. Pieper, Günter Wiesinger, Herwig Michor, Clemens Ritter, and Frank Kubel. *Phys. Rev. B*, 73:144408, 2006.

[10] P Novak and J Rusz. *Phys. Rev. B*, 71(18), 2005.

[11] V Prochazka, H Stepankova, J Stepanek, A Snezhko, V Chlan, and K Kouril. *Acta Physica Slovaca*, 56(2):165–168, 2006.

[12] N Momozawa, Y Yamaguchi, H Takei, and M Mita. *Journal of the Physical Society of Japan*, 54(10):3895–3903, 1985.

[13] N Momozawa, Y Yamaguchi, H Takei, and M Mita. *Journal of the Physical Society of Japan*, 54(2):771–780, 1985.

[14] T. Kimura, G. Lawes, and A. P. Ramirez. *Phys. Rev. Lett.* , 94:137201, 2005.

[15] Shigenori Utsumi, Daisuke Yoshiba, and Nobuyuki Momozawa. *Journal of the Physical Society of Japan*, 76(3), 2007.

[16] Hosho Katsura, Naoto Nagaosa, and Alexander V. Balatsky. *Phys. Rev. Lett.* , 95:057205, 2005.

[17] I. A. Sergienko and E. Dagotto. *Phys. Rev. B*, 73:094434, 2006.

[18] A. B. Harris. *Phys. Rev. B*, 76:054447, 2007.

[19] Maxim Mostovoy. *Phys. Rev. Lett.* , 96:067601, 2006.

[20] I. Dzyaloshinsky. *Journal of Physics and Chemistry of Solids*, 4(4):241 – 255, 1958.

[21] Tôru Moriya. *Phys. Rev.* , 120:91–98, 1960.

[22] E. A. Turov and M. P. Petrov. *Nuclear magnetic resonance in ferro and antiferromagnets*. Halsted Press, a division of John Willey & Sons, Inc. New York, 1972.

[23] A. Abragam. *Principles of nulear magnetism*. Oxford University Press, 1961.

[24] Melinda J. Duer. *Introduction to Solid–State NMR Spectroscopy*. Blackwell Publishing Ltd Oxford, 2004.

[25] Malcolm H. Levitt. *Spin Dynamics: Basics of Nuclear Magnetic Resonance, Second Edition*. Wiley, 2008.

[26] Harald Günter. *NMR Spectroscopy: Basic principles, concepts, and applications in chemistry*. John Willey & Sons Ltd, Chichester, 1994.

[27] G. Allodi, R. De Renzi, G. Guidi, F. Licci, and M. W. Pieper. *Phys. Rev. B*, 56:6036–6046, 1997.

[28] A. M. Portis and A. C. Gossard. *Journal of Applied Physics*, 31(5):S205–S213, 1960.

[29] H Stepankova, J Kohout, J Englich, and P Novak. *Hyperfine Interactions*, 131(1-4):3–19, 2000.

[30] K Kouril, J Kohout, H Stepankova, J Englich, and V Chlan. *Acta Physica Slovaca*, 56(1):31–34, 2006.

[31] O. Krogh Andersen. *Phys. Rev. B*, 12:3060–3083, 1975.

[32] S.Cottenier. *DFT and the Family of (L)APW-methods: a step-by-step introduction.* (Instituut voor Kern- en Stralingsfysica, K.U.Leuven, Belgium), 2002. (to be found at http://www.wien2k.at/reg user/textbooks).

[33] Petr Blaha, Karlheinz Schwarz, Georg Madsen, Dieter Kvasnicka, and Joachim Lutz. *Wien2k An Augmented plane Wave Plus Local Orbitals Program for Calculating Crystal Properties.* Vienna University of Technology, 2001.

[34] K Schwarz, P Blaha, and GKH Madsen. *Computer Physics Communications*, 147(1-2):71–76, 2002.

[35] P. Hohenberg and W. Kohn. *Phys. Rev.* , 136:B864–B871, 1964.

[36] W. Kohn and L. J. Sham. *Phys. Rev.* , 140:A1133–A1138, 1965.

[37] A. Svane and O. Gunnarsson. *Phys. Rev. Lett.* , 65:1148–1151, 1990.

[38] Vladimir I. Anisimov, Jan Zaanen, and Ole K. Andersen. *Phys. Rev. B*, 44:943–954, 1991.

[39] V. I. Anisimov, I. V. Solovyev, M. A. Korotin, M. T. Czyżyk, and G. A. Sawatzky. *Phys. Rev. B*, 48:16929–16934, 1993.

[40] M. T. Czyżyk and G. A. Sawatzky. lacuo$_3$. *Phys. Rev. B*, 49:14211–14228, 1994.

[41] AD Becke. *Journal of Chemical Physics*, 98(2):1372–1377, 1993.

[42] P Novak, J Kunes, L Chaput, and WE Pickett. *Physica Status Solidi B-Basic Solid State Physics*, 243(3):563–572, 2006.

[43] Fabien Tran, Peter Blaha, Karlheinz Schwarz, and Pavel Novák. *Phys. Rev. B*, 74:155108, 2006.

[44] Antoine Georges. *arXiv:cond-mat/0403123*, 2004.

[45] Antoine Georges, Gabriel Kotliar, Werner Krauth, and Marcelo J. Rozenberg. *Reviews of Modern Physics*, 68:13–125, 1996.

[46] G. Kotliar, S. Y. Savrasov, K. Haule, V. S. Oudovenko, O. Parcollet, and C. A. Marianetti. *Reviews of Modern Physics*, 78:865–951, 2006.

[47] J. Hubbard. *Phys. Rev. B*, 17:494–505, 1978.

[48] P. W. Anderson. *Phys. Rev.* , 124:41–53, 1961.

[49] John P. Perdew, Kieron Burke, and Matthias Ernzerhof. *Phys. Rev. Lett.*, 77:3865–3868, 1996.

[50] RFW Bader. *Theoretical Chemistry Accounts*, 105(4-5):276–283, 2001.

[51] V. Chlan, H. Stepankova, R. Reznicek, and P. Novak. *Solid State Nuclear Magnetic Resonance*, 40(1):27–30, 2011.

[52] P. Novak and V. Chlan. *Phys. Rev. B*, 81:174412, 2010.

[53] Josef Bursik, Ivo Drbohlav, Zdenek Frait, Karel Knizek, Radomir Kuzel, and Karel Kouril. *Journal of Solid State Chemistry*, 184(11):3085–3094, 2011.

[54] P. Gornert et al. *Key Engineering Materials*, 58:129–148, 1991.

[55] E. R. Malinowski. *Factor Analysis in Chemistry.* Wiley, third edition, 1972.

[56] Z. Šimša, R. Geber, R.Atkinson, and P.Papaonstantinon. Ferrites. *Proc. ICF 6 Tokyo*, 1992.

[57] Y. S. Chai, S. H. Chun, S. Y. Haam, Y. S. Oh, Ingyu Kim, and Kee Hoon Kim. *New Journal of Physics*, 11, 2009.

[58] X Obradors, A Isalgue, A Collomb, A Labarta, M Pernet, JA Pereda, J Tejada, and JC Joubert. *Journal of Physics C-Solid State Physics*, 19(33):6605–6621, 1986.

[59] Arthur Miller. *Journal of Applied Physics*, 30(4):S24–S25, 1959.

[60] K Knizek, P Novak, and M Kupferling. *Phys. Rev. B*, 73(15), 2006.

[61] Pavel Novak and Karel Knizek. *Journal of Magnetism and Magnetic Materials*, 316(2):E587–E590, 2007.

[62] N Momozawa, M Mita, and H Takei. *Journal of Crystal Growth*, 83(3):403–409, 1987.

[63] V. Prochazka, H. Stepankova, B. Sedlak, Cz. Kapusta, K. Knizek, Z. Jirak, J. Englich, and R. Reznicek. *Journal of Magnetism and Magnetic Materials*, 320(14):E12–E15, 2008.

[64] G Albanese, M Carbucicchio, A Deriu, G Asti, and S Rinaldi. *Applied Physics*, 7(3):227–238, 1975.

[65] H Stepankova, J Englich, M Nejezchleba, J Kohout, and H Lutgemeier. *Journal of Magnetism and Magnetic Materials*, 157:393–394, 1996.

[66] H Stepankova, J Englich, EG Caspary, and H Lutgemeier. *Journal of Magnetism and Magnetic Materials*, 177:253–254, 1998.

[67] H Stepankova, J Kohout, P Novak, J Englich, EG Caspary, and H Lutgemeier. *Australian Journal of Physics*, 51(2):437–452, 1998.

[68] MN Berberan-Santos, EN Bodunov, and B Valeur. *Chemical Physics*, 315(1-2):171–182, 2005.

[69] AV Zalesskii, VD Doroshev, and VG Krivenko. *Fizika Tverdogo Tela*, 24(1):20–27, 1982.

[70] Helena Štěpánková. *Studium hexagonálních feritů magnetoplumbitové struktury metodou jaderné magnetické rezonance.* Kandidátská disertační práce na Matematicko–Fyzikální fakulě Univerzity Karlovy na katedře fyziky nízkých teplot. Praha, 1994.

[71] AS Kamzin. *Journal of Experimental and Theoretical Physics*, 89(5):890–898, 1999.

[72] AS Kamzin, VL Rozenbaum, and LP Ol'khovik. *Physics of the Solid State*, 41(3):433–439, 1999.

[73] G Albanese, A Deriu, E Lucchini, and G Slokar. *Applied Physics A-Materials Science & Processing*, 26(1):45–50, 1981.

[74] D. Seifert, J. Toepfer, F. Langenhorst, J. M. Le Breton, H. Chiron, and L. Lechevallier. *Journal of Magnetism and Magnetic Materials*, 321(24):4045–4051, 2009.

[75] Lotgerin.FK. *Journal of Physics and Chemistry of Solids*, 35(12):1633–1639, 1974.

[76] R. Grossinger, M. Kupferling, M. Haas, H. Muller, G. Wiesinger, and C. Ritter. *Journal of Magnetism and Magnetic Materials*, 310(2, Part 3):2587–2589, 2007.

[77] C Sauer, U Kobler, W Zinn, and H Stablein. *Journal of Physics and Chemistry of Solids*, 39(11):1197–1201, 1978.

[78] Vandiepe.AM and Lotgerin.FK. *Journal of Physics and Chemistry of Solids*, 35(12):1641–1643, 1974.

[79] H Stepankova, J Englich, P Novak, and H Lutgemeier. *Journal of Magnetism and Magnetic Materials*, 104(Part 1):409–410, 1992.

[80] R. L. Streever. *Phys. Rev.*, 186:285–290, 1969.

[81] AA Bezlepkin and SP Kuntsevich. *Low Temperature Physics*, 31(3-4):283–284, 2005.

[82] A. I. Liechtenstein, V. I. Anisimov, and J. Zaanen. *Phys. Rev. B*, 52:R5467–R5470, 1995.

[83] P Novak, K Knizek, M Kupferling, R Grossinger, and MW Pieper. *European Physical Journal B*, 43(4):509–515, 2005.

[84] MW Pieper, A Morel, and F Kools. *Journal of Magnetism and Magnetic Materials*, 242(Part 2):1408–1410, 2002.

[85] MW Pieper, F Kools, and A Morel. *Phys. Rev. B*, 65(18), 2002.

[86] H Stepankova, J Kohout, and Z Simsa. *Journal of Magnetism and Magnetic Materials*, 104(Part 1):411–412, 1992.

[87] Zhai H., Xu Y., Liu J., Yang G., Lu M., Jin T., and Wang Z. *Cryst. Prop. Prep.*, 27–30:473, 1990.

[88] B. X. Gu. *Journal of Applied Physics*, 70(1):372–375, 1991.

[89] G Wiesinger, M Muller, R Grossinger, M Pieper, A Morel, F Kools, P Tenaud, JM Le Breton, and J Kreisel. *Physica Status Solidi A-Applied Research*, 189(2):499–508, 2002.

[90] R. Krishnan. *Physics of Magnetic Garnets*. LXX Corso, Soc. Italiana di Fisica, Bologna, 1978. p. 504.

[91] H Stepankova, J Englich, J Kohout, and H Lutgemeier. *Journal of Magnetism and Magnetic Materials*, 140(Part 3):2099–2100, 1995.

Articles related to the thesis:

1. Josef Bursik, Ivo Drbohlav, Zdenek Frait, Karel Knizek, Radomir Kuzel, and Karel Kouril. Oriented SrFe12O19 thin films prepared by chemical solution deposition. *Journal of Solid State Chemistry*, 184(11):3085–3094, 2011.

2. K. Kouril, V. Chlan, H. Stepankova, A. Telfah, P. Novak, K. Knizek, Y. Hiraoka, and T. Kimura. Distribution of Zn in Magnetoelectric Y-Type Hexaferrite. *Acta Physica Polonica A*, 118(5):732–733, 2010.

3. S. Kamba, V. Goian, M. Savinov, E. Buixaderas, D. Nuzhnyy, M. Marysko, M. Kempa, V. Bovtun, J. Hlinka, K. Knizek, P. Vanek, P. Novak, J. Bursik, Y. Hiraoka, T. Kimura, K. Kouril, and H. Stepankova. Dielectric, magnetic, and lattice dynamics properties of Y-type hexaferrite Ba0.5Sr1.5Zn2Fe12O22: Comparison of ceramics and single crystals. *Journal of Applied Physics*, 107(10), 2010.

4. Karel Kouril, Vojtech Chlan, Helena Stepankova, Pavel Novak, Karel Knizek, Jiri Hybler, Tsuyoshi Kimura, Yuji Hiraoka, and Josef Bursik. Hyperfine interactions in magnetoelectric hexaferrite system. *Journal of Magnetism and Magnetic Materials*, 322(9-12):1243–1245, 2010.

5. Helena Stepankova, Karel Kouril, Vojtech Chlan, Peter Goernert, Robert Mueller, and Josef Stepanek. Internal magnetic fields in submicron particles of barium hexaferrite detected by Fe-57 NMR. *Journal of Magnetism and Magnetic Materials*, 322(9-12):1323–1326, 2010.

Other articles:

1. V. Prochazka, H. Stepankova, V. Chlan, J. Tucek, J. Cuda, K. Kouril, J. Filip, and R. Zboril. Electric field gradient in FeTiO3 by nuclear magnetic resonance and ab initio calculations. *Journal of Physics-Condensed Matter*, 23(20), 2011.

2. V. Chlan, H. Stepankova, J. Englich, R. Reznicek, K. Kouril, M. Kucera, and K. Nitsch. Antisite Defects in Epitaxial Films of Lutetium Doped Yttrium Iron Garnets Studied by Nuclear Magnetic Resonance. *Acta Physica Polonica A*, 118(5):846–847, 2010.

3. B. Sedlak, K. Kouril, V. Chlan, R. Reznicek, P. Kristan, M. Pfeffer, J. Englich, and H. Stepankova. Tuned Probehead for NMR Spectroscopy in Magnetically Ordered Materials. *Acta Physica Polonica A*, 118(5):924–925, 2010.

4. V. Chlan, K. Kouril, H. Stepankova, R. Reznicek, J. Stepanek, W. Tabis, G. Krol, Z. Tarnawski, Z. Kakol, and A. Kozlowski. Magnetically induced structural reorientation in magnetite studied by nuclear magnetic resonance. *Journal of Applied Physics*, 108(8), 2010.

5. Vojtech Chlan, Pavel Novak, Helena Stepankova, Richard Reznicek, Karel Kouril, and Andrzej Kozlowski. Electronic structure and hyperfine fields in non-stoichiometric magnetite above the Verwey transition. *Journal of Magnetism and Magnetic Materials*, 322(9-12):1079–1081, 2010.

6. V. Chlan, E. Gamaliy, H. Stepankova, K. Kouril, J. Englich, J. Kohout, and V. Brabers. Nuclear magnetic resonance of Fe-57 in Al-, Ga- and Ti-substituted magnetite above Verwey temperature. *Journal of Magnetism and Magnetic Materials*, 310(2, Part 3):2555–2557, 2007.

7. K Kouril, J Kohout, H Stepankova, J Englich, and V Chlan. Nuclear magnetic resonance of Fe-57 from magnetic domains and walls in yttrium iron garnet. *Acta Physica Slovaca*, 56(1):31–34, 2006.

8. V Prochazka, H Stepankova, J Stepanek, A Snezhko, V Chlan, and K Kouril. Exchange interactions in barium hexaferrite. *Acta Physica Slovaca*, 56(2):165–168, 2006.